STATISTICAL ANALYSIS AND SENSOR BASED MODELING OF ELECTROCHEMICAL MECHANICAL POLISHING (ECMP) OF Cu BLANKET WAFER FOR SEMICONDUCTOR APPLICATIONS

By

SAKTHI JAYA RAHUL RAVICHANDRAN

Bachelor of Engineering in Mechanical Engineering

Velammal Engineering College (VEC)

Anna University

Chennai, India

2010

Submitted to the Faculty of the
Graduate College of the
Oklahoma State University
in partial fulfillment of
the requirements for
the Degree of
MASTER OF SCIENCE
July, 2013

STATISTICAL ANALYSIS AND SENSOR BASED MODELING OF ELECTROCHEMICAL MECHANICAL POLISHING (ECMP) OF Cu BLANKET WAFER FOR SEMICONDUCTOR APPLICATIONS

Thesis Approved:

Dr. Satish T.S. Bukkapatnam

Thesis Adviser

Dr. Zhenyu (James) Kong

Dr. Sandip P. Harimkar

ACKNOWLEDGEMENTS

I would like to express my deepest gratitude to my advisor Dr. Satish T. S. Bukkapatnam for continually motivating and helping me to associate with his research group. I really thank him for providing me such an opportunity to be part of his research and for his timely advice, which helped me to learn a lot from him. The research meetings really helped me to develop my presentational skills. His continual encouragement and inspiration triggered my thoughts and help me accomplish the suggested tasks. Secondly I would like to thank my committee members, Dr. James Kong and Dr. Sandip Harimkar, for giving me important insights which helped me in completing my research. A special thanks to Dr. Sadagopan Krishnan for providing me some important ideas and thoughts for my research work. Thirdly, I would like to thank my research colleagues Anant K. Arulmozhi, Omer Beyca, Woranat Wongdhamma, Robin Wang, Thiagarajan Nagarajan, and Prahalad K Rao for their help and advice. Fourthly, I would like to thank my Stillwater friends as well as my Indian friends for continually helping and motivating me.

This project is funded by grants (CMMI-0700680 and CMMI-1000978) from the Manufacturing Processes and Machines of the division of Civil, Mechanical, and Industrial Innovation of the National Science Foundation. And I would like to thank NSF for its interest and support for this work.

I would like to dedicate this work to my dearest parents, Mr.Ravichandran and Mrs Umamaheswari, my sister Hamsavarthini, my Uncle Kanagaraj and Aunt Mahadevi for their kind support and playing an important role in shaping my life.

Finally I would like to thank God for providing me such an opportunity and guiding me throughout my research work. This work would have been impossible without his grace.

Name: SAKTHI JAYA RAHUL RAVICHANDRAN

Date of Degree: JULY, 2013

Title of Study: STATSITICAL ANALYSIS AND SENSOR BASED MODELING OF ELECTROCHEMICAL MECHANICAL POLISHING (ECMP) OF Cu BLANKET WAFER FOR SEMICONDUCTOR APPLICATIONS

Major Field: INDUSTRIAL ENGINEERING & MANAGEMENT (IEM)

Copper electrochemical mechanical polishing (Cu ECMP) has attracted many scientists in the field of semiconductor manufacturing industry, as they are investigating whether to replace chemical mechanical polishing (CMP) with Cu ECMP after the introduction of porous low - k dielectric materials because of its increased efficiency and better quality. An approach to locating real time variations in Cu ECMP processes has been identified. The various regions in Cu ECMP, active, passive, trans-passive, and transient regions have been explored through current and voltage signals obtained from a data acquisition setup hooked up with the process. Extensive work has been done in characterizing and optimizing the process, but little work has been done in correlating the key process input variables (KPIV) such as voltage, platen speed and wafer carrier speed with the key process output variables (KPOV) such as the material removal rate (MRR) and surface roughness (R_a) using time-frequency patterns of the current-voltage signals and statistical models. Based on these analytical methods, optimal surface value was realized in the transient/trans-passive region. A mathematical model depicting ECMP was implemented in COMSOL to understand the characteristics of the process, which will be a great breakthrough in the field of semiconductor manufacturing.

TABLE OF CONTENTS

Chapter Page

LIST OF TABLES

Table Page

LIST OF FIGURES

Figure Page

APPENDICES

CHAPTER I

RESEARCH OVERVIEW AND OBJECTIVES

1.1 Introduction

Copper electrochemical mechanical planarization (ECMP) has been preferred as an alternative technology to copper chemical mechanical polishing (CMP) in semiconductor industries since the introduction of fragile, porous, low k dielectric materials and copper as interconnect materials in the fabrication of printed circuit boards (PCBs) [1,2,3]. Copper is generally used as interconnect material because of its higher conductivity and excellent electro migration resistance [4]. The use of fragile, low k dielectric materials, requires that the down force in CMP be greatly reduced to manage their weak mechanical strength and structural integrity and to reduce dishing and erosion during their fabrication [5, 6]. CMP problems are also related to stability in the slurry, scratches generated on the surface of the wafer, metal contaminants, post cleaning methods and the high cost of equipment and process maintenance [4]. Initially electrochemical polishing was thought of as an alternative to CMP to overcome these problems because of its non-contact nature. Later on, it was realized that ECP has limited application in polishing copper interconnects because of its pattern sensitivity, residual copper island formation, and very low planarization efficiency (<40%). However, ECMP has been proposed as a better alternative to meet industrial demands for bulk copper planarization because of its high material removal rate (MRR), the improved surface quality, and its exceptional planarization efficiency, reducing defects and attaining higher throughputs with very low applied pressure (<0.5 psi) [1,5,6,7]. In ECMP, an anodic potential serves as a thermodynamic driving force for oxidation instead of an oxidizing agent, as in the case of CMP. Thus, ECMP may not require strong oxidizers, complexing agents, and slurry particles, which make CMP waste slurry treatment costly. In CMP, slurry particles have a

tendency to form aggregates, which can get embedded on the wafer surface and cause scratches on the surface. Moreover, the aggregates can enter the polishing pad and can degrade the life of the pad. ECMP has eliminated the use of slurry particles and the reduction in pad replacement has reduced the cost of the consumables by about 30% [6, 7]. The other important factor that makes a big difference in the industry is the processing cost. For instance, the cost of the slurry in CMP is about $15 to $20 for processing a single wafer, whereas it is about $4.5 to $6 less in ECMP, because the electrolyte-based slurry used in ECMP reduces the cost [13]. In ECMP, the copper ions react with the components in the electrolyte to form a passivation layer, and a polishing pad helps in achieving better planarization. The passivation layer formed when the copper ions react with other components of the electrolyte can be removed with one-tenth of the mechanical down force (<0.5 psi) used in CMP. A high material removal rate (MRR) can be obtained, which helps in determining surface quality and improves planarization [3, 5, and 6].

Despite continual research carried out on ECMP, some of the technological gaps and challenges with respect to several aspects of the process are as follows:

a) There is little understanding of the relationship between the various key process input variables (KPIV) and key process output variables (KPOV) involved in the ECMP process.

b) There are not many real time monitoring techniques for ECMP.

c) The interaction effects of various input parameters on the output parameters are still unknown.

d) The absence of statistical models to provide a relationship between various key process input variables (KPIV) and key process output variables (KPOV) creates a great challenge.

e) There are few analytical models which can simulate the ECMP process.

Table 1-1 below interprets the relationship between the key process input variables (KPIV) and key process output variables (KPOV) in the ECMP process

Table 1-1: Various KPIV's and KPOV's involved in ECMP

FACTORS	KEY PROCESS INPUT VARIABLES (KPIV's)/ PROCESS PARAMETERS	STATE VARIABLES	KEY PROCESS OUTPUT VARIABLES (KPOV's)/ PERFORMANCE/RESPONSE VARIABLES
Machine (Including the External Power Source)	Down Force, Platen speed, Wafer carrier speed, Input Voltage	Stress Distribution, Velocity Distribution, Passivation Layer formation	Endpoint thickness of the wafer, Output Voltage and Output Current patterns, MRR and R_a
Polishing Pad	Stiffness, Topography, Conditioning, Pad Uniformity, Porosity	Contact area, Pad Pressure, Degradation and Temperature Distribution	Material Removal Rate (MRR)(nm/min) and Pad wear
Slurry	Acid based electrolyte, Chelating agent, Inorganic/Organic salt, Oxidizer, pH adjusting agent, Corrosion Inhibitor, Abrasive particulates, Solvent	pH drifts, Concentration, Size distribution, Dispersion, Agglomeration, Aggregation	Within Wafer Non-Uniformity (WIWNU), Wafer to Wafer Non-Uniformity, Within Die Non Uniformity (WIDNU), Erosion, Micro scratch and Pits
Wafer	Size, Curvature, Properties of coating, Coating thickness variation & Pattern Geometry	Direct contact, Mixed contact	Surface finish, Roughness

The goal of this research is to tackle the issue of process predictability and control by incorporating sensor based modeling and statistical analysis techniques. It focuses on developing models predicting the key process output variables (KPOV) with the help of the design of

experiments and sensor based modeling techniques [8]. A Real time monitoring of the process is performed by analyzing the process current signals. Comsol model was developed to relate various key process input variables (KPIV) such as voltage pH, polishing pad speed, wafer carrier speed, pad contact angle with key process output variables (KPOV) such as material removal rate (MRR) and surface roughness (R_a) in the ECMP process and various statistical models were developed for predicting key process output variables (KPOV).

1.2 Overview of ECMP process

1.2.1 Chemical Mechanical Polishing (CMP)

CMP is a process of smoothing surfaces with the combination of chemical and mechanical forces as shown in Figure 1-1. A chemical reaction takes place between the slurry and the work piece thus resulting in a polished surface removed by the mechanical action of the abrasives [7, 8].

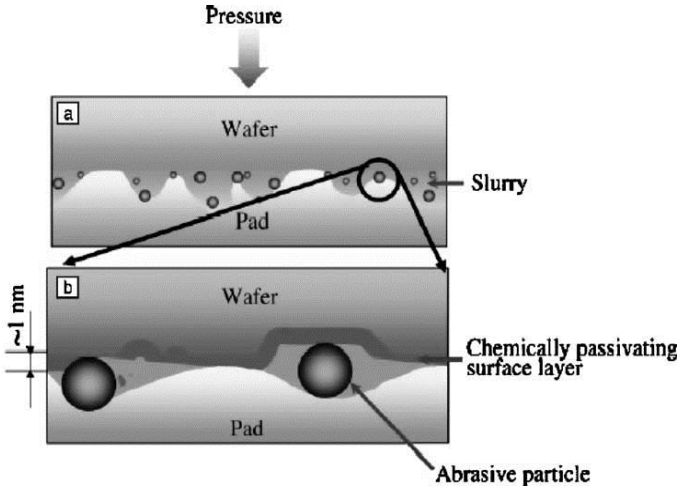

Figure 1-1: Schematic diagram of Chemical mechanical polishing [9]

1.2.2 Electro chemical Polishing (ECP)

ECP is a process of polishing using the combined effect of electric potential and chemical reaction. The schematic of the ECP process is shown in Figure 1- 2.

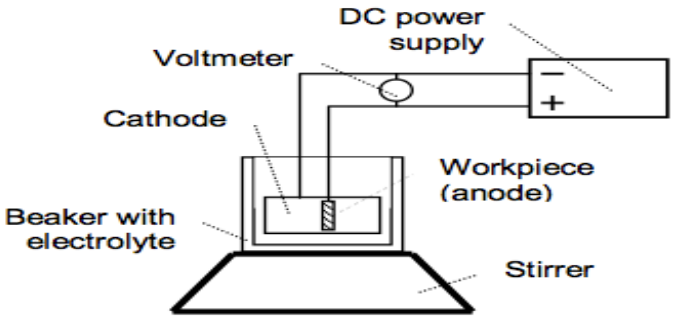

Figure 1-2: Diagram of Electrochemical polishing [10]

1.2.3 Electrochemical Mechanical Polishing (ECMP)

A chemical reaction is stimulated by giving an electric potential to the slurry wherein the work piece acts as an anode and a metal with less electro negativity acts as a cathode, resulting in the formation of a passivation layer which is swept off periodically by the polishing pad, thereby improving MRR and surface finish (R_a).

1.3 Schematics of the ECMP Process

In the ECMP process as shown in Figure 1-3, the copper wafer is placed inside a wafer carrier and the wafer acts as an anode. An aluminum bar, which is less electronegative compared to the anode, is used as a cathode.

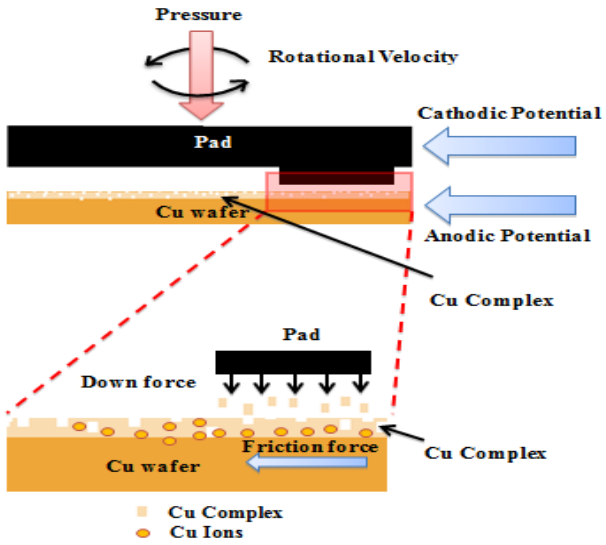

Figure 1-3: Schematic diagram of ECMP process [103]

The slurry is poured into the wafer carrier and the copper wafer is submerged in the slurry. The polishing pad faces downwards and the wafer carrier faces upwards, exhibiting a rotary motion. A galvanic corrosion takes place whenever a cathode and an anode are immersed in a conductive electrolytic bath, i.e. because of the anodic potential, the electrons migrate from the anode to the cathode and the copper at the surface is oxidized, which leads to the formation of Cu^{2+} ions as depicted in equations (1-1) and (1-2).

$$Cu(s) \rightarrow Cu^{+} + e^{-} \qquad (1\text{-}1)$$

$$Cu(s) \rightarrow Cu^{2+} + 2e^{-} \qquad (1\text{-}2)$$

Cu^{2+} ions are more predominant than Cu^{+} ions in ECMP due to applied anodic potential. The Cu^{2+}ions combine with the oxidizer and other components present in the slurry, leading to the formation of a 0.1 - 10^3 nm thin film of a soft copper oxide complex that serves as a passivation layer. The basic composition of the passivation layer comprises metallic oxides, hydroxides and metallic complexes. The formation of oxides in the passivation layer on the anode can be depicted by equations (1-3), (1-4) and (1-5) [11].

$$2Cu^{+} + H_2O \rightarrow Cu_2O + 2H^{+} \qquad (1\text{-}3)$$

$$Cu^{2+} + 2OH^{-} \rightarrow Cu(OH)_2 \qquad (1\text{-}4)$$

$$Cu_2O + H_2O \rightarrow 2CuO + 2H^{+} + 2e^{-} \qquad (1\text{-}5)$$

The formation of hydroxides and a copper complex with phosphoric acid slurry is given by equation (1-6)

$$Cu^{2+} + H_3PO_4 + H_2O \rightarrow [Cu\ OH] + [H_2PO_4]^{-} + 2H^{+} + 2e^{-} \qquad (1\text{-}6)$$

When applied to the slurry, the electrode potential stimulates a chemical reaction in the slurry. Thus, the removal of ions takes place from the copper wafer and a complex formation occurs on

the top of the copper, which is otherwise known as the passivation layer and which is removed by the hard polyurethane polishing pad.

1.4 Definition of key terms

1.4.1 Slurry

Slurry plays a key role in the electrochemical mechanical process in the form of a medium of contact between the polishing wafers and the supplied potential. It must be carefully selected so that the surface becomes completely devoid of topographical defects. Slurries basically consist of some fixed components, which are imperative in producing a good surface finish in electrochemical mechanical polishing [12].

The important components of the slurry are Acid-based electrolyte, Chelating agents, Inorganic or organic salts, Corrosion inhibitor, pH adjusting agent, Oxidizer and Abrasive particles.

1.4.2 Polishing pad

In ECMP, the mechanical action is given by the polishing pad, which helps in sweeping the passivation layer formed due to the electrochemical reaction on the work piece.

1.4.3 Voltage and current characteristics

The potential given to the slurry and the work piece plays a vital role in determining the material removal rate and surface finish. Voltage and current effects in the process help in determining various electrochemical states in active, passive, transient and trans-passive regions [13].

1.5 Challenges in ECMP

- The voltage and current signals obtained from a sensor associated with the process have not been analyzed to study the process characteristics.
- There is little understanding of the interaction effect of the KPIVs on the KPOVs of the process.
- The mapping of the process using voltage and current signals is limited to CMP and has not been done in ECMP.
- There are few statistical models depicting the effects of the KPIVs on the KPOVs of the process.
- There are very few models depicting the ECMP process.

1.6 Objective statement

- To integrate an ECMP setup with voltage and current sensors for Real - time data acquisition while performing statistically designed experiments.
- To conduct statistical analysis of the experimental data to determine the process conditions to optimize the material removal rate (MRR) and surface finish (R_a).
- To conduct validation experiments to realize optimal ECMP process quality and performance
- To develop a computational model of the ECMP process based on the experimental observations.
- To conduct simulations based on the computational model to study the effects of various process parameters on material removal rates.
- To verify the effects gathered from the model simulations with experimental data.

CHAPTER II

BACKGROUND AND LITERATURE REVIEW

2.1 Parameters affecting MRR and Surface Roughness

Shattuck *et al.* [7] used an electrolyte constituted of orthophosphoric acid, potassium phosphate as a pH adjusting agent, BTA as corrosion inhibitor, and deionized water. Experiments were conducted by controlling the pH of the slurry between 0 and 10 by varying the ratio of kH_2PO_4/k_2HPO_4in 1M potassium phosphate, inhibitor concentrations and salt concentrations from 0 to 0.1M and 0.1 to 1.6M respectively to observe the variations in surface finish and surface quality on a (4cm X 1cm) size sample. They found that an ideal electrolyte must consist of 1M salt concentration and BTA in order to enhance the material removal rate without increasing the surface roughness.

Andriacos *et al.* has suggested that phosphoric-acid-based slurry can be effectively used in Copper ECMP [7].

Goonetilleke *et al.* [39] studied the effect of complexing agent (Acetic acid), Oxidizer (Hydrogen Peroxide) and corrosion inhibitor (BTA) on ECMP of copper. Acetic acid was observed to provide good resistance against pH drift. Acetic acid can provide high planarization efficiency as it is used to remove oxides and hydroxides formed on the surface. Acetic acid can eliminate the need of a pH lowering additive.

Kwon *et al.* [40] used Potassium Hydroxide based slurry for Cu ECMP. The electrolyte consisted of KOH, H_2O_2 and citric acid. It was observed that the material removal rate increased when 5% by weight KOH, 5% by volume H_2O_2 and 0.3M citric acid were used.

Tripathi *et al*. [1] studied the influence of pH and a complexing agent on the surface quality and Cu removal rate during ECMP on blanket Cu-coated wafers. The Cu ECMP electrolyte

containing 5-phenyl-1-H-tetrazole (PTA) provided good Cu removal rates and planarization efficiencies but the surface roughness was considered to be higher than the roughness with Cu CMP. The surface roughness of the Cu wafer decreased when the pH of the slurry was increased from 3 to 6 and decreased with the replacement of a less aggressive complexing agent (glycine) for oxalic acid. Figure 2-1 shows the variation of pH with surface roughness in a glycine containing ECMP slurry. It was observed that the surface roughness decreased as the pH was increased from 3 to 6. Figure 2-2 shows the variation in Cu removal rate with the pH of the slurry. It was observed that the Cu removal rate decreased from 620 to 420 nm/min when the pH was raised from 3 to 6.Thus, the pH has a major role to play in the surface roughness and the Cu removal rate in Cu ECMP.

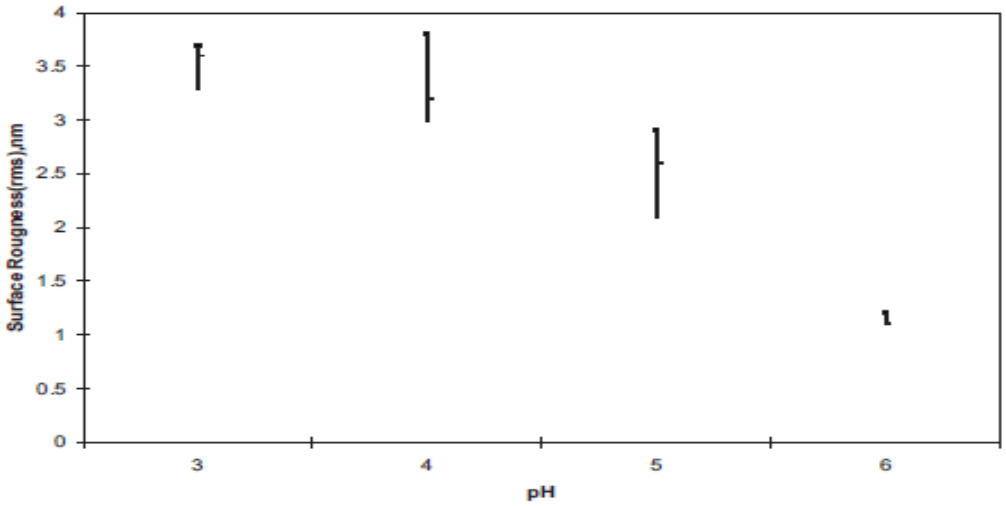

Figure 2-1: RMS surface roughness vs. pH for ECMP electrolytes containing 0.29 M HEDP ,0.13 M glycine, 1mM PTA and 3wt% colloidal silica .ECMP polishing done at 3.5V [1]

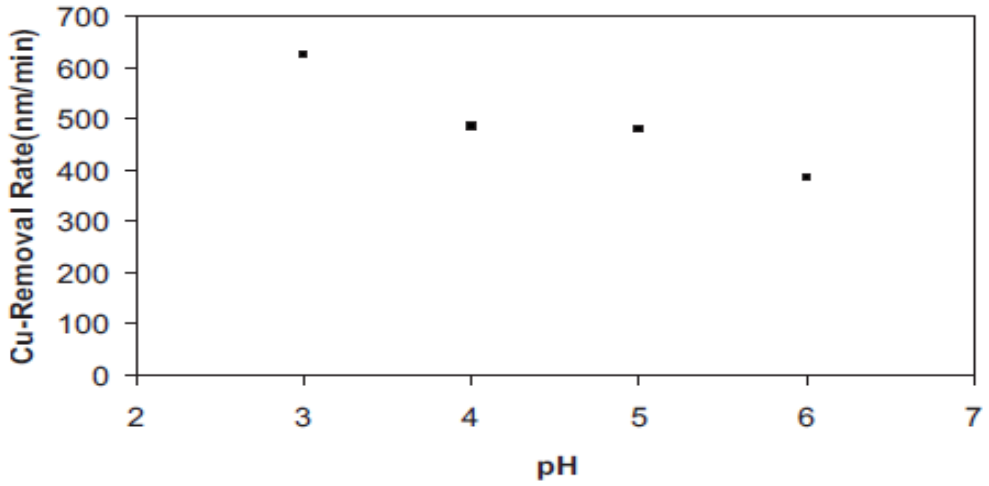

Figure 2-2: Cu removal rate as a function of pH for ECMP electrolytes containing 0.29 M HEDP, 0.13 M glycine, 1mM PTA and 3wt% colloidal silica. ECMP polishing done at 3.5V [1]

Oh *et al.* [4] indicated that the pH value of the electrolyte must be 14 or higher for a higher polishing rate. The higher polishing rate may be due to the effective formation of mechanically soft compounds such as $Cu(OH)_2$, $HCuO^{2-}$ and CuO_2 $^{-2}$ under the application of anodic potentials.

Ng *et al.* [43] suggested that the hard phase of Cu_2O is formed in the pH range of 6-14 at an applied anodic potential of 0.4 - 0.3V. The pH was maintained mainly at 6 to avoid the Cu_2O hard phase by adding phosphoric acid to the slurry, when an anodic potential of 0.4-0.1V was applied.

Liu *et al.* [5] studied the effect of down force in ECMP of Cu wafers and suggested that the low down force significantly reduces the erosion of dense features, which can be prominently observed in CMP due to the high pad pressure. The pad structure also plays a vital role in determining the planarization quality and efficiency in the ECMP process. Hard polyurethane polishing pads are generally used in Cu –ECMP.

Brown [14] found that polishing speed also plays an important role in ECMP. The conventional CMP cannot achieve a high speed until the pad pressure on the wafer is increased. If the speed is increased, the high pad pressure can crack and peel away the low-k dielectric film. Therefore, the polishing speed has to be reduced in CMP, which can lead to an increase in the polishing time of the wafer. ECMP can get the same planarization in less time because the electrochemical mechanism accompanies the mechanical polishing.

Gao [41] studied the effect of speed on Tantalum ECMP using impedance curves by keeping load and potential constant. It was observed that the data points of the impedance were random at 20rpm unlike those which followed a sine function. The average number of impedance was higher at 50rpm than that at 60rpm, but the period of the impedance curve at 50 rpm was shorter than the impedance curve obtained at 60 rpm. It was observed that the average impedance was highest at 20 rpm indicating that the formation of thick oxide layer and low mechanical power. Thus, there was little oxide material removal. The oxide removal rate increased with increase in rpm due to the development of high mechanical power .The oxide layer was thinner at 60 rpm due to lower average impedance as shown in Figure 2-3.

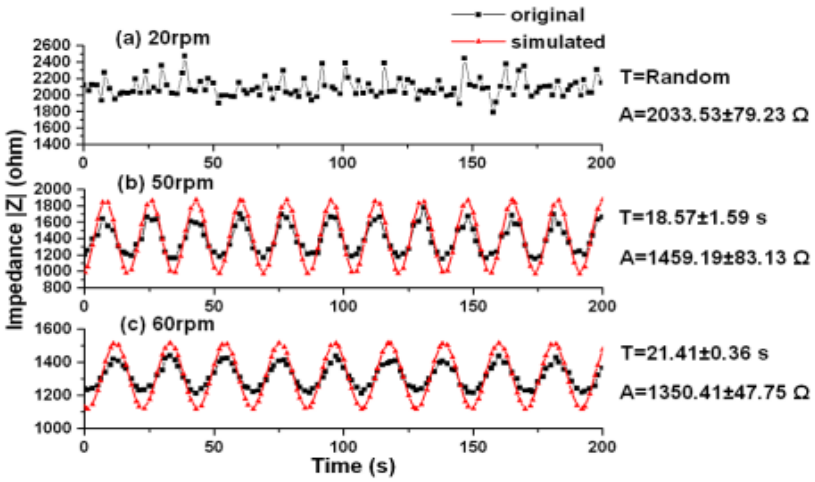

Figure 2-3: The enlarged impedance curves and sinusoidal simulation curves with different rotating speed under 4N and 1V [41]

Bae *et al.* [17] suggested that, as the ECMP process involves both mechanical as well as electrochemical processes, a polymeric pad must have mechanical integrity and chemical resistance to survive the rigors of polishing. Generally, a polishing pad must have an acceptable level of hardness, modulus, and good abrasion resistance to endure the Cu ECMP process. The polishing pad must also be able to survive aggressive electrolytic conditions such as highly alkaline and highly acidic conditions. In ECMP the contact of the polishing pad with the surface creates a low down pressure such that the metal film is not delaminated from the underlying low-k film. As a result, defects such as dishing, erosion, and scratching that are quite common among CMP processes are minimized. In ECMP, the passivation film protects the low-lying areas of the substrate, whereas the polishing pads remove the protruding peaks. The main role of the polishing pad is to remove the passivation layer by electrochemical reaction as shown in Figure 2-4.

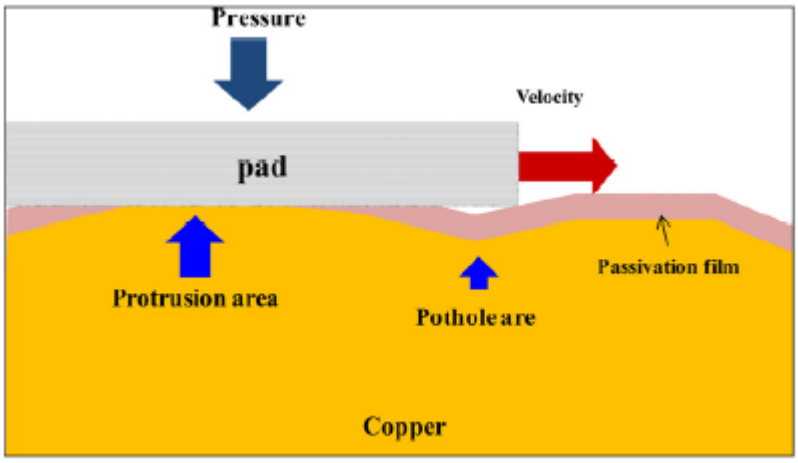

Figure 2-4: Role of polishing pad in Cu ECMP process [17]

Experiments were carried out to verify the effects of the mechanical properties of the polishing pad. Viscoelastic deformation and the strain of various polishing pads such as polymer impregnated felt pads (Suba 600, Nitta – Hass) and polyurethane pads (IC 1400 K-groove, Nitta – Hass) were analyzed. A type III polyurethane pad which had stable viscoelastic behavior and high chemical attack resistance in the electrolyte was chosen for the Cu ECMP process. As the

hardness of the polyurethane pads was higher than that of the polymer impregnated felt pads, global uniformity was achieved and the MRR was higher when the polyurethane pad was used in the Cu ECMP process. The abrasives on the polishing pad help in removing the passivation film formed by the electrochemical reaction in the electrolyte. Even when the abrasives do not play a vital role in improving the uniformity, when the concentration of abrasive was greater than the 10% volume of electrolyte, the roughness was decreased.

Jeong *et al*. [18] suggested that the copper ions are dissolved electrochemically by the application of an anodic potential on the copper surface in an aqueous electrolyte, whereas the copper complex layer is removed by the mechanical abrasion of the polishing pad or the abrasives present in the slurry in ECMP. The polishing pad used in the ECMP process is generally a conventional closed-cell pad (IC 1400 K-groove pad) with holes. It generally helps in supplying aqueous electrolyte to the copper surface, which in turn helps in removing the complex layer. MRR and the MRR profile were simulated and tested on different types of polishing pads with holes classified based on the change in the wafer overhang distance (WOD), i.e. the non-contact distance between the wafer surface, such as Type A, Type B, and Type C, and the polishing pad and by changing the electric contact area (ECA) such as Type 1, Type 2 and Type 3 as shown in Figure 2-5.

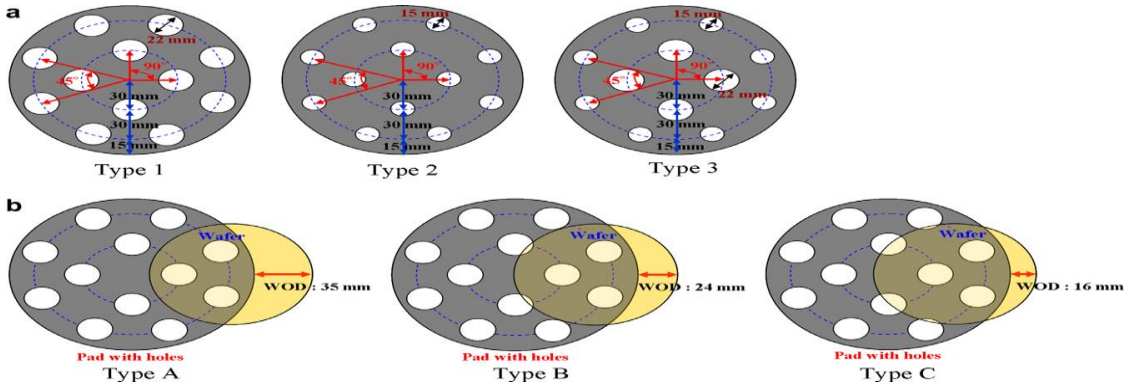

Figure 2-5: a) Polishing pad types by changed ECA, b) Polishing pad types by changed WOD [18]

The simulation and the experimental results suggested that the MRR and the uniformity of the Cu wafer were not only influenced by ECA types, but also by the WOD types of polishing pads with holes. MRR and WIWNU were greatly affected by the WOD-based polishing pads. It was observed that when the WOD and ECA were increased the MRR also increased.

Kondo *et al.* [19] developed a new ECMP setup which makes uses a 16-inch conductive carbon pad for polishing 300 mm wafers. The pad is composed of a surface carbon layer, which acts as an anode, an intermediate insulating layer, and an underlying cathode sheet. More than one hundred electro-cells were fabricated within the tri-layered structure, and it was about 5 mm thick. The intermediate insulating layer acted as a cushion layer to improve WIWNU. A soft carbon material was chosen to reduce the damage caused by direct contact with the copper surface. The power supply was connected to the anode and cathode at the edge of the pad. The main advantage of the carbon pad is that it has an adhesive back which can be easily replaced, and the transition from CMP to ECMP can be easily done by just replacing the conventional polyurethane pad with the carbon pad. It was observed that the removal rate increased and good non-uniformity was obtained in proportion with the current. Thus, this new ECMP resulted in a high material removal rate and better non-uniformity in the low-pressure region. Thus, it resolved several issues such as scratching, copper residues, and cathode regeneration, which were well known in conventional ECMP.

Chen *et al.* [11] suggested that the material removal rate is low at lower electric potentials because of the mechanical action of the pad, but the material removal rate increases at a higher potential because of the effect of electric potential enhancement by the mechanical force.

Tiley *et al.* [42] observed higher MRR in ECMP than CMP in case of titanium and nickel alloys. The oxide layer on the surface of the film was observed to be twice the thickness on application of current.

2.2 I-V characteristics

Seo *et al.* [15] have done significant work on the characterization of the electrochemical mechanism of the ECMP process. The voltage-activated electrochemical reactions of Cu were studied with different concentrations of HNO_3 electrolyte. Based on the I-V curve obtained from linear sweep voltammetry (LSV) and cyclic voltammetry (CV) methods, the effect of the concentration of electrolyte on the electrochemical surface reaction of the Cu electrode and various electrochemical characteristics of Cu, such as active, passive, transient, and trans-passive states, were estimated. The various electrochemical states were identified using IV curves as shown in Figure 2-6. The region where the relationship between voltage and current is linear is known as the active state. In the active state, the anode (Cu) undergoes a dissolution reaction. When the voltage is increased from -0.25V to 0.25V, the passive region is formed, where a passive film composed of a metallic hydroxide compound is found. The reactions are shown in equations (2-1) and (2-2):

$$Cu + 2H_2O \rightarrow CuOH.H_2O + H^+ + e^- \quad (2\text{-}1)$$

$$CuOH \rightarrow CuO + H^+ + e^- \quad (2\text{-}2)$$

As the increase in voltage cannot overcome the barrier, a plateau type of passive state is formed. The passive film starts to deteriorate when the anodic potential of 0.25 V is reached. It is very clear from Figure 2-6 that the passive state begins where the first voltage (V=IR) drop occurs and the second IR drop specifies the commencement of a trans-passive state, as shown in the dotted boxes (A) and (B) in Figure 2-6. A voltage drop indicates an abrupt increase in resistance. This phenomenon indicates the formation of passive oxides such as CuO or Cu_2O on the Cu surface. The material removal rate was calculated from the weight loss before and after the voltage – activated electrochemical reaction.

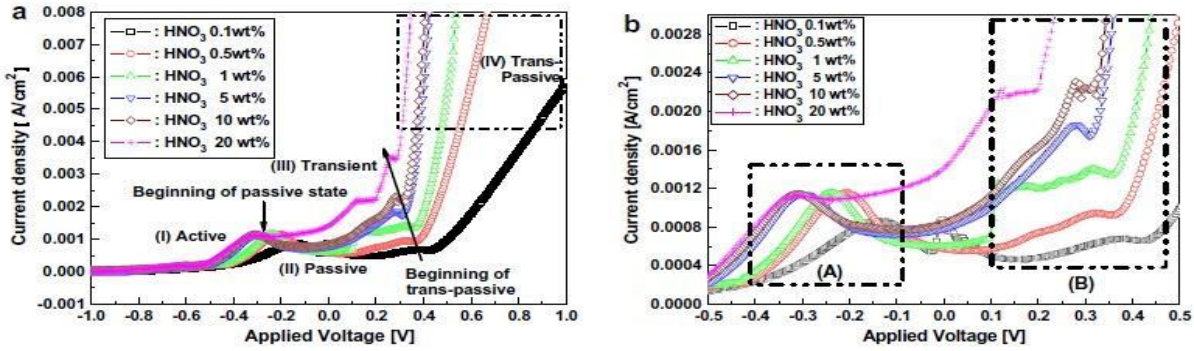

Figure 2-6: I-V curve of HNO_3 electrolyte with different concentration.(a) Full I-V curve, (b) Detailed I-V curve between -0.5V and 0.5V [15]

From the I-V plot obtained from cyclic voltammetry, it was observed that when the positive voltage was scanned from -2 to +2V, the electrochemical reaction corresponded to the oxidation reaction (2-3) and when the negative voltage was scanned from +2 to -2V, the electrochemical reaction corresponded to the reduction reaction (2-4).

$$Cu \rightarrow Cu^{2+} + 2e^{-} \qquad (2\text{-}3)$$

$$Cu^{2+} + 2e^{-} \rightarrow Cu \qquad (2\text{-}4)$$

The cyclic voltammetry curves also clearly showed the deposition and stripping of Cu .The cathodic current peaks corresponded to bulk deposition and under-potential deposition of Cu^{2+} on the Cu surface; the anodic peaks corresponded to the stripping of bulk and under-potential deposited copper.

SEM was used to characterize the surface at different electrochemical states. The voltages, which were decided from Figure 2-6, corresponded to the (b) active state (-1.0V), (c) the passive state (-0.25V) and the trans-passive state (0.7V) respectively. Some scratches were observed on the initial surface as shown in Figure 2-7(a). These scratches were less obvious; some bubble marks and pitting corrosion were observed on the surface as shown in Figure 2-7(b). Severe corrosion and passive oxide were observed in the passive state as shown in Figure 2-7(c). The surface

quality was completely different in the trans-passive state, as shown in figure 2-7(d). The stripping of Cu ions from the electrochemical Cu surface resulted in a sponge like uniform surface.

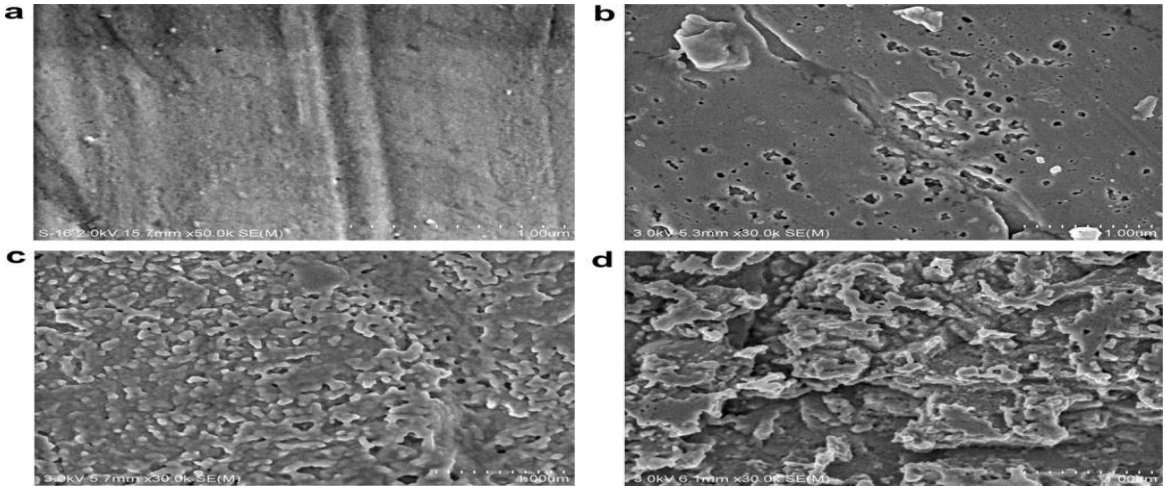

Figure 2-7: SEM surface photographs at different operating voltage in 0.1wt% HNO_3 electrolyte. (a)Original surface of no bias, (b) active state;-1.0V, (c) passive state;-0.25V and (d) trans-passive state; 0.7V [15]

Han and Seo [13] used I-V curves obtained from LSV and CV for evaluating the effect of electrolyte concentration on the electrochemical reaction trend and on the characterization of various electrochemical states in the active, passive, transient, and trans-passive regions. He carried out his ECMP experiments on 99.99% pure Cu disks 2cm X 2cm in size between 0.5V and 1V. The I-V curves in Figure 2-8 were plotted as a function of KNO_3 and HNO_3 electrolytes with concentrations of 5%, 10% and 20%. It was observed that the concentration of KNO_3 electrolyte increased as the trans- passive voltages were decreased and the current density was increased. A plateau region, called the passive state, was not formed because the continuous passive oxide or metallic hydroxide remained on the Cu surface. As the voltage was increased, the potential was great enough to pull the metallic ion through the passive film. As the concentration of the HNO_3 electrolyte was increased, the transient voltages were decreased and

the curve slope of the trans-passive state was observed to steeper, which indicated that the I-V relationship depends strongly on the concentration of the electrolyte.

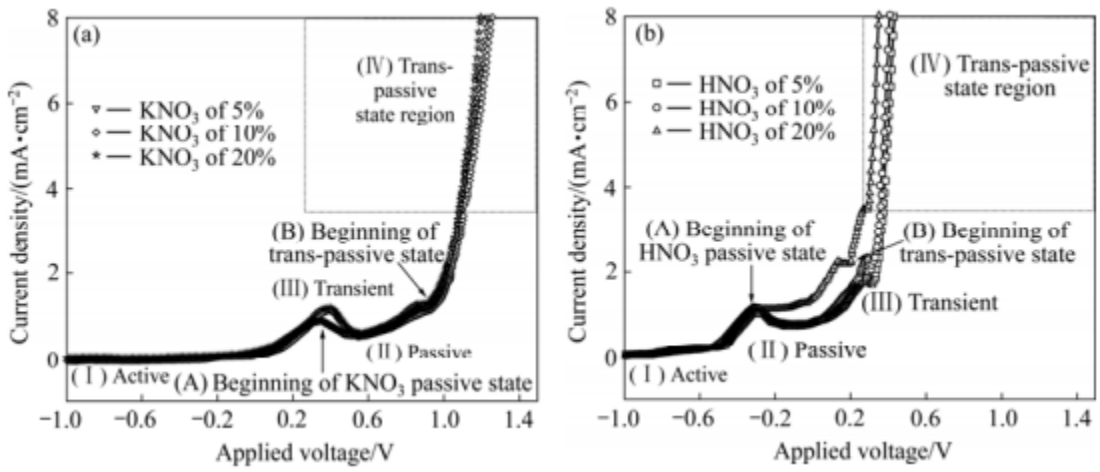

Figure 2-8: I-V curves as a function of electrolyte concentration of (a) KNO_3 and (b) HNO_3 for Cu after [13]

It was also observed that, when the concentration of the electrolyte and the operating time increased, the material removal rates also increased. And from the cyclic voltammetric curves, Han and Seo observed that the both anodic and cathodic currents and the originating surface reactions of both anodic and cathodic currents determine the surface reactivity of Cu under the given electrolyte conditions. The anodic stripping of Cu ions was indicated by the anodic peak and the under-potential deposition of Cu ions were indicated by the relatively cathodic peaks.

Lee *et al.* [16] investigated the polishing mechanism of the electrochemical mechanical polishing (ECMP) technology for tooling steel SKD11.The electrochemical characteristics such as the active, passive, transient, and trans passive stages of tooling steel SKD11 were studied. The I-V curve, as shown in Figure 2-9, represents a general electrochemical reaction. We can observe that the relationship between the applied voltage and current density is linear, as shown in the a-b region. The anode is under a normal dissolution reaction. It is called the active state. The initial

active potential of the anode (a) is very important for positioning the applied voltage of all electrochemical states under operating conditions. This potential can be derived from the Nernst equation as shown in (2-5).

$$E_d = E_r + \eta_c + \eta_a + IR = (E_r - E_a) + \eta_c + \eta_a + IR \qquad (2\text{-}5)$$

where E_d is the decomposition potential, E_r is the reversible potential, E_c is the cathodic reversible potential, E_a is the anode reversible potential ,η_c is the cathode overpotential, η_a is the anode over-potential, and IR is the potential drop.

When the anode reaches potential b, the concentration constraint sets the limit for dissolution. The passive film starts to pile up as the voltage is increased from c to d. The passive film is generally composed of a metallic hydroxide compound. It has high electrical resistance as well. As the increase in the voltage cannot overcome the barrier, a plateau region, c-d, also known as the passive state, is formed. Further increase in voltage makes the potential strong enough to pull the metallic ion through the passive film, causing the passive film to begin to peel off until it reaches the potential e. The d-e region is called the transient state. From transient state, it enters the trans-passive state, making the reaction very active. The substrate is exposed when the damaged passive film comes off, revealing more surfaces for electrochemical reaction. Thus, it is very important to understand the electrochemical mechanisms at various states of the I-V curve in order to understand the optimal mechanism and process parameters for the ECMP technology.

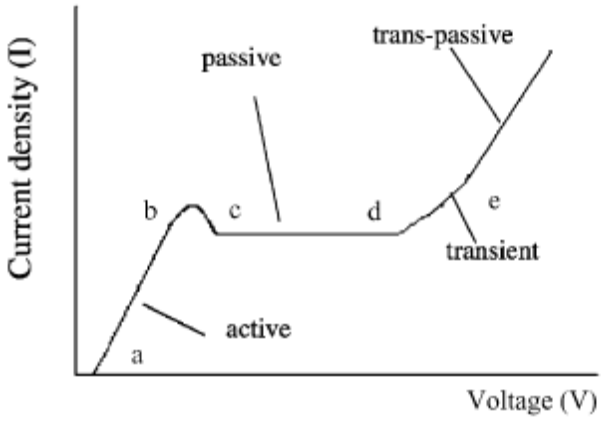

Figure 2-9: I-V curve showing different electrochemical states in ECMP of tool steel (SKD11) [16]

2.3 Computational Modeling of ECMP

Fukuda *et al.* **[**20**]** developed a method for simulating the Cu removal rate in the dissolution-type electro chemical mechanical process as shown in Figure 2-10.

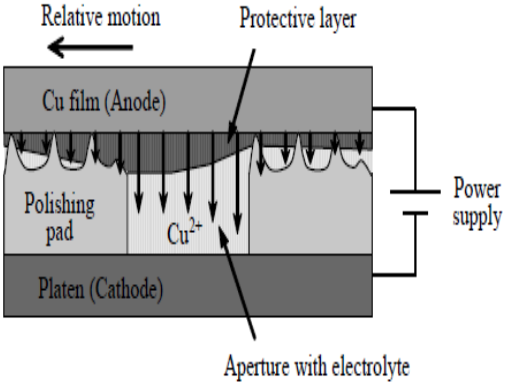

Figure 2-10: Dissolution type mechanism of Cu removal [20]

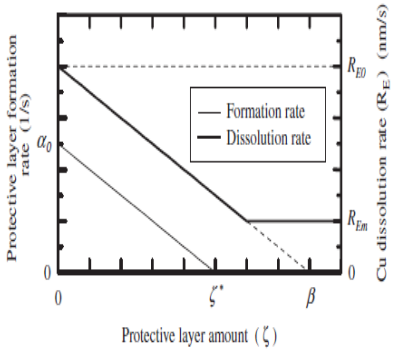

Figure 2-11: Fundamentals of simulation model [20]

Fukudu *et al*. [20] modeled the protective layer amount ζ assuming that the Cu dissolution rate depends on the protective layer amount on the Cu surface. The protective layer amount ζ was modeled as a dimensionless quantity using the following equation (2-6).

$$\zeta = \int \alpha_0 \left(1 - \frac{\zeta}{\zeta^*}\right) \mathrm{dt} - \int \mathrm{kpvdt_p} \qquad (2\text{-}6)$$

Where the amount of the protective layer formed by contact with the electrolyte is the first term on the right side and is expressed as the product of protective layer formation rate and time. The second term on the right side is the Preston equation, which represents the amount of protective layer removed by the polishing pad. It is represented as the product of the coefficient k[$(Pa.m)^{-1}$], the polishing pressure p (Pa), the relative speed between the polishing pad and Cu film v(m/s), and the time of contact with the polishing pad t_p (s).The protective layer formation rate decreases as the protective layer amount increases. The protective layer formation rate reaches a maximum α_0, and when the protective layer amount is 0, it is saturated at ζ^*. The relationship between the Cu dissolution rate and the protective layer amount is modeled by a linear function as shown in equation (2-7).

$$R_E = \max\left[R_{EO}\left(1 - \frac{\zeta}{\beta}\right), R_{EM}\right] \qquad (2\text{-}7)$$

Where R_E is the dissolution rate in the aperture region of the polishing pad expressed in (nm/s), R_{EO} is the maximum dissolution rate expressed in (nm/s), β is a coefficient determining the gradient of the dissolution rate, R_{EM} is the minimum dissolution rate expressed in (nm/s), and max is the function that returns the maximum value. $R_{E0,}$ R_{EM}, Cu removal rate and the electrical resistance of the aperture depend upon the electrolyte filling ratio, defined as the ratio of electrolyte volume to aperture volume. The Cu dissolution amount EA, expressed in (nm), can be obtained as the time integration of the dissolution rate, as explained in equation (2-8).

$$EA = \int R_E \, dt_h + \delta \int R_E \, dt_p \qquad (2\text{-}8)$$

On the right side of the equation, the first term represents the Cu dissolution amount in the aperture region, the second term represents the Cu dissolution amount in the non-aperture region of the polishing pad, R_E is Cu dissolution rate in aperture region (nm/s), t_h is the time required to pass through the apertures (s), t_p is the time of contact with the polishing pad (s), and δ is the ratio of the dissolution rate in the non-aperture region to that in the aperture region of the polishing pad. The simulation parameters used in all the equations are determined from experimental results. The simulations accurately demonstrated the dependence of the Cu removal rate on the aperture ratio. But, a discrepancy was observed between the simulation and experimental results as this method did not consider the dependence of the electrolyte-filling ratio in the apertures on the aperture diameter. If the electrolyte filling ratio in the apertures is small, then this model can accurately simulate the dependence of the Cu removal rate on the aperture diameter.

Truque *et al.* [22] proposed a wafer level dynamic ECMP model based on the current density distributions with respect to time across the wafer. The model was able to confine the wafer level non–uniformity and time-dependent ECMP removal, time-varying voltage zones and to produce optimal voltage zone control schemes. The wafer was discretized in order to calculate the potential and current distributions based on the applied voltage zones and metal film thickness. It was found that the copper removal rate was proportional to the current density and that the copper thickness can be calculated as a function of its position on the wafer and polish time. The key relationship in the model was achieved between the removal rate and the applied charge as shown in the equation (2-9).

$$I\left[\frac{C}{sec}\right].\frac{1}{area[cm^2]}.\frac{1atom_{cu}}{2e^-[C]}.\frac{1mole_{Cu}}{N_A\,atoms_{Cu}}.\frac{63.546g_{Cu}}{1mole_{Cu}} \qquad (2\text{-}9)$$

$$.\frac{1cm^3}{8.941g_{cu}}.\frac{10^7\,nm}{1\,cm}.\frac{60sec}{1\,min} = RR\left[\frac{nm}{min}\right]$$

$$area_{wafer} = 706.85\,cm^2 \;\rightarrow\; \frac{RR}{I} = 29.93\,\frac{nm}{A.min}$$

2.4 Statistical process Monitoring and Control

Chen *et al.* [21] described a feedback control process model of ECMP developed using the manufacturing analysis method (MAM), and an experimental system has verified the developed process model. The schematics of the ECMP experimental system are shown in the Figure 2-12.

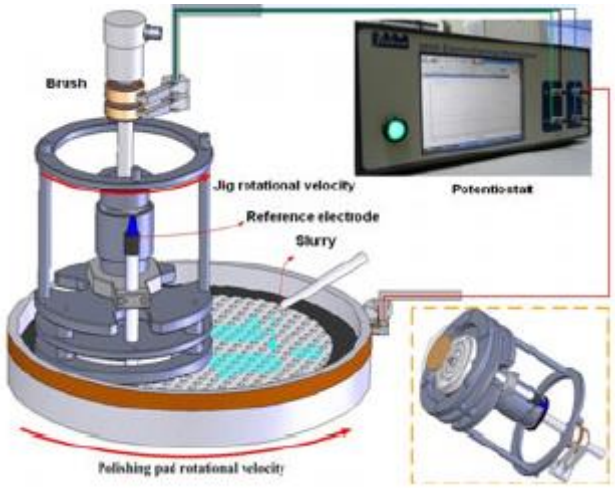

Figure 2-12: Schematics of the ECMP experimental system [21]

The feedback model is shown in Figure 2-12.It was used to analyze the effect of input energy and process parameters. The process parameters (α) include properties (e_p), equipment states (e_s), material properties (m_p), and material states (m_s), where, e_p includes pad hardness, slurry pH value ,pores on pad, type of electrolyte, chemical additive and oxidation and inhibitor concentrations of the slurry. e_s includes platen speed, down force, voltage, electrode space and temperature of the electrolyte; m_p includes the thickness of the Cu film and Cu pattern structure; m_s includes the normal force and friction force between pad and wafer and the bias voltage between wafer and cathode. The variation equation was used for optimal results by controlling the process stability, as shown in Figure 2-12. Δu was made 0 and the disturbance sensitivity term was minimized .The ECMP process feedback was achieved by compensating for the disturbances and manipulating the control inputs.

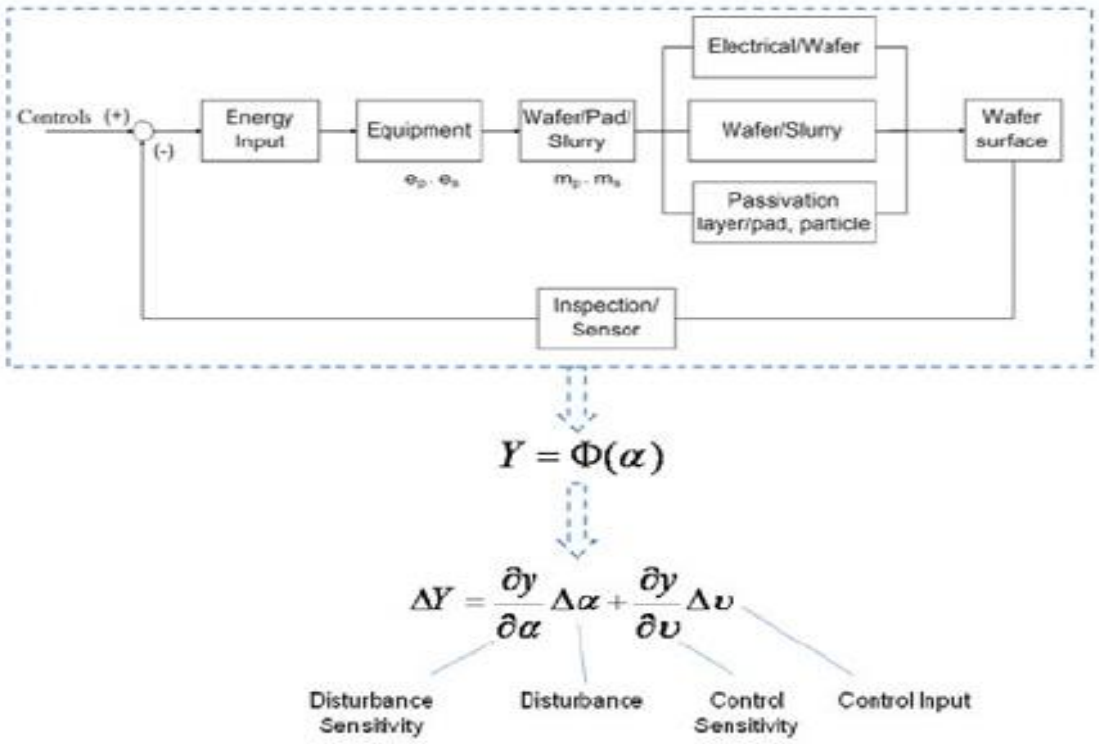

Figure 2-13: ECMP process model [21]

Potential dynamic polarization curves were used to characterize the active, passive, transient, and trans-passive regions of the reaction of H_3PO_4 based slurry with copper specimens. Based on the developed process model, experimental results revealed that the MRR was higher and less surface roughness was obtained in the transient region. The results showed a significant improvement of ECMP performance as the variation equation can be used to define the relationship between the disturbance, disturbance sensitivity, control input, and control sensitivity.

Gao *et al.* [23] developed a new method for finding a relationship between the oxidation state and tantalum processing during the ECMP process. Faraday's law was utilized to calculate the MRR, which was compared with the observations obtained from the atomic force microscope (AFM) measurements. The Preston equation was used to provide a relationship with MRR as a linear

function of mechanical force. According to Faraday's law, the relationship between the weight of oxidized metal and the released electrons from the metal is expressed in equation (2-10).

$$W = \frac{MQ}{nqN_o} \quad (2\text{-}10)$$

where W represents the weight of metal oxidized in (g), Q is the quantity of electrons released as a result of oxidation (C), M is the molar mass of the metal, n is the valence of the oxidized atoms, q is the elementary charge ($1.602X10^{-19}$ C), and N_o is Avogadro's number ($6.023X10^{23}$ mol^{-1}). And the material removal rate is given in equation (2-11).

$$MRR = \frac{MQ}{n\rho qN_0 At} \quad (2\text{-}11)$$

Where MRR is the material removal rate in (nm/min), ρ is the density, A is the sample area, and (t) is the polishing time. The quantity of electrons can be obtained by integrating the anodic current into total polishing time (T) in s as shown in the equation (2-12).

$$Q = \int_0^T I_{anodic} d\tau \quad (2\text{-}12)$$

Preston's equation, as shown in equation (2-13) has been modified to develop a relationship between the load, polishing speed, and material removal rate (MRR).

$$MRR = kPV \quad (2\text{-}13)$$

Where P is the load applied to the specimen, V is the polishing speed, and k is the Preston constant ($7.75 X 10^{-10} N^{-1}$).

It was observed that Faraday's law and the direct MRR calculation were not well correlated. By comparing the measured and calculated MRR, identification of Ta oxides was made possible. Mechanical force played a vital role in finding different Ta oxides.

Xu *et al.* [32] developed a least squares support vector machine (LS-SVM) based model for predicting surface quality and determining optimum processing parameters in electrochemical mechanical polishing of bearing rollers. The LS-SVM model, with the radial basis function (RBF) kernel with core adjustment parameters γ and σ, was built using dataset D =

$\{(x_k,y_k),k=1,2,..,N\}$ consisting of N- dimensional input data $x_k \epsilon R^N$ and output data $y_k \epsilon R$, as given in equation (2-14).

$$y = \sum_{k=1}^{N} \gamma e_k^T \exp\left(-\frac{\|x-x_k\|^2}{2\sigma^2}\right) + b \qquad (2\text{-}14)$$

where, γ is the regularization parameter, e_k represents the random error, $\exp\left(-\frac{\|x-x_k\|^2}{2\sigma^2}\right)$ is the kernel function, σ is the kernel width parameter and b is the bias term, which can be derived from equation (2-15).

$$\begin{bmatrix} \Omega + \gamma^{-1} I & \theta \\ \theta^T & 0 \end{bmatrix} \begin{bmatrix} \alpha \\ b \end{bmatrix} = \begin{bmatrix} y \\ 0 \end{bmatrix} \qquad (2\text{-}15)$$

where $y = [y_1,\ldots,y_N]^T$, $\theta = [1,\ldots,1]^T$, $\alpha = [\alpha_1,..,\alpha_N]^T$, I is an identity matrix, Ω is a square matrix, and α can be determined using equation (2-15).

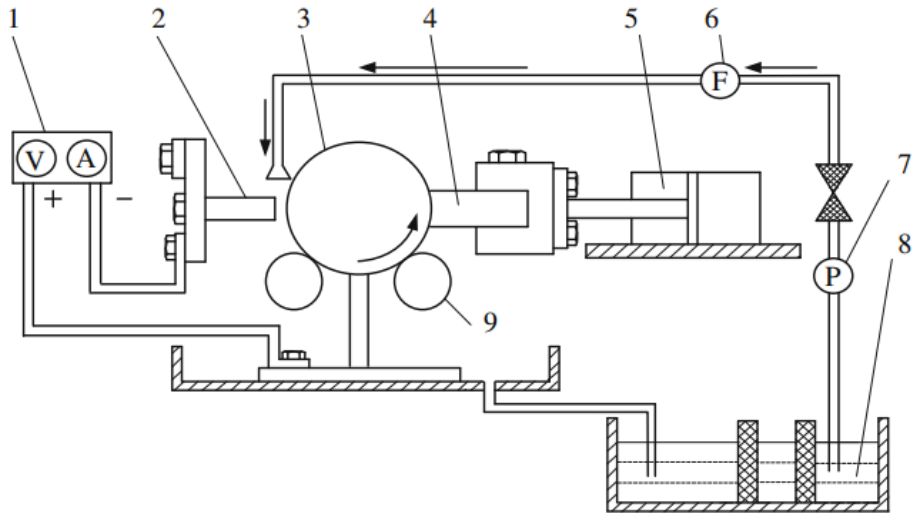

1. DC power; 2. tool cathode; 3. workpiece anode; 4. grinding tool;
5. cylinder; 6. flowmeter; 7. pump; 8. eletrolyte; 9. driving wheels

Figure 2-14: Experimental Principle of the ECMP process for bearing rollers [32]

An experimental setup as shown in Figure 2-14 was used to collect an experimental dataset to validate the model. The rotating speed of the work piece, the pressure of the grinding tool, current density, grit size, and machining time were chosen as the most important input parameters, and

surface roughness R_a was considered the output parameter. It was found that the values based on the LS-VSM prediction model with a RBF kernel were in reasonable agreement with the experimental values as shown in Figure 2-15. The mean absolute percent error and root mean square error values were found to be 5.4% and 6.5% respectively. Current density was identified to exert a stronger effect on surface roughness than the other polishing input parameters, with R=0.00809 as shown in figure 2-15. The mean absolute percent error and root mean square error values were found to be 4.8% and 6.6% respectively.

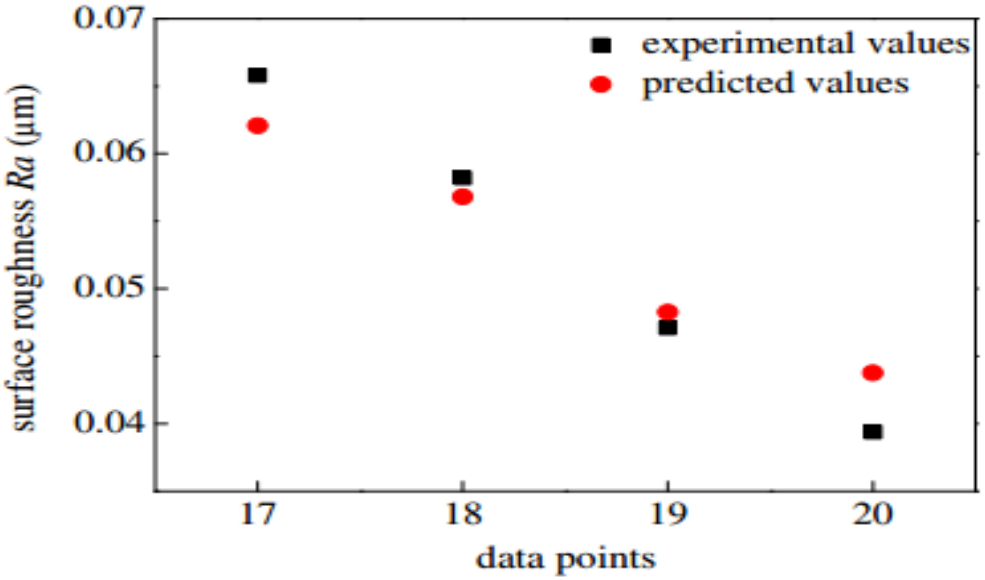

Figure 2-15: Comparison between predicted and experimental values of surface roughness [32]

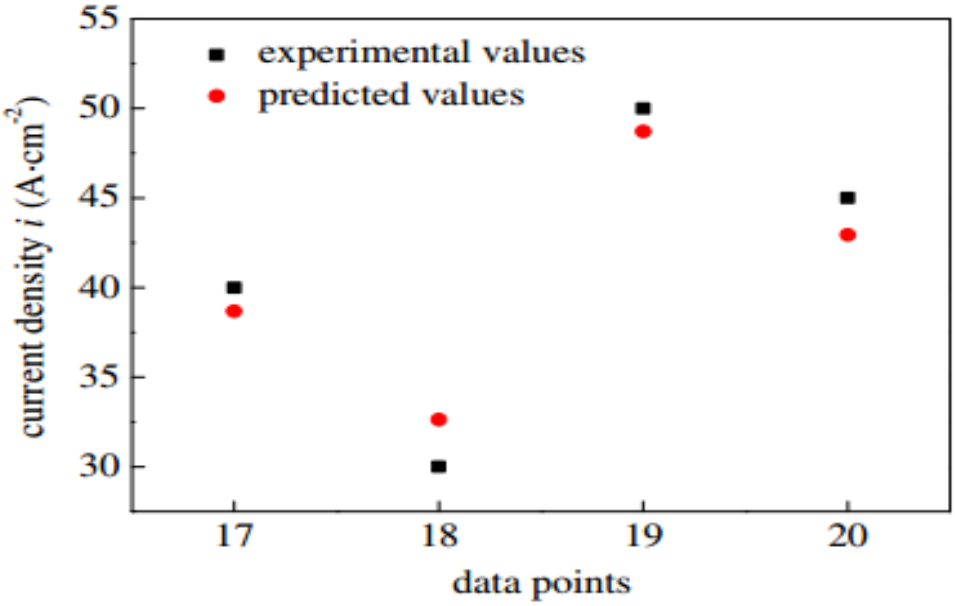

Figure 2-16: Comparison between predicted and experimental values of current density [32]

CHAPTER III

EXPERIMENTAL OPTIMIZATION OF ECMP PROCESS

3.1 Sensor Integrated ECMP apparatus development

A face-up ECMP apparatus as shown in Figure 3-1was designed and fabricated for polishing 4-inch dia copper wafers. Two mini vertical milling machines (Model 44991) from Central Machineries were arranged in such a way that one milling machine holds the wafer carrier and the other milling machine provides a rotary motion for the wafer carrier by means of a drive pulley and a V-belt. The axes of the wafer carrier and the pad holder tables were offset so that the Cu wafers could be completely polished by the polishing pad as they rotate relative to each other. An aluminum bar was used as cathode as it has a higher electrode potential compared to copper. The rotational speeds of the polishing pad and wafer carrier were controlled using the knobs in each milling machine. The wafer carrier position was adjusted with respect to the polishing pad by moving the working table using the cross feed handle wheel and the longitudinal feed handle wheel. A Shenzhen Mastech power supply, having a working range of 0.1 – 1.2V was used to make the anode (wafer) and the cathode conductive. A wooden base was used to insulate the first mini milling machine from the positively charged anode in the wafer carrier assembly. The apparatus was placed under a fume hood to exhaust the chemical fumes formed during the process.

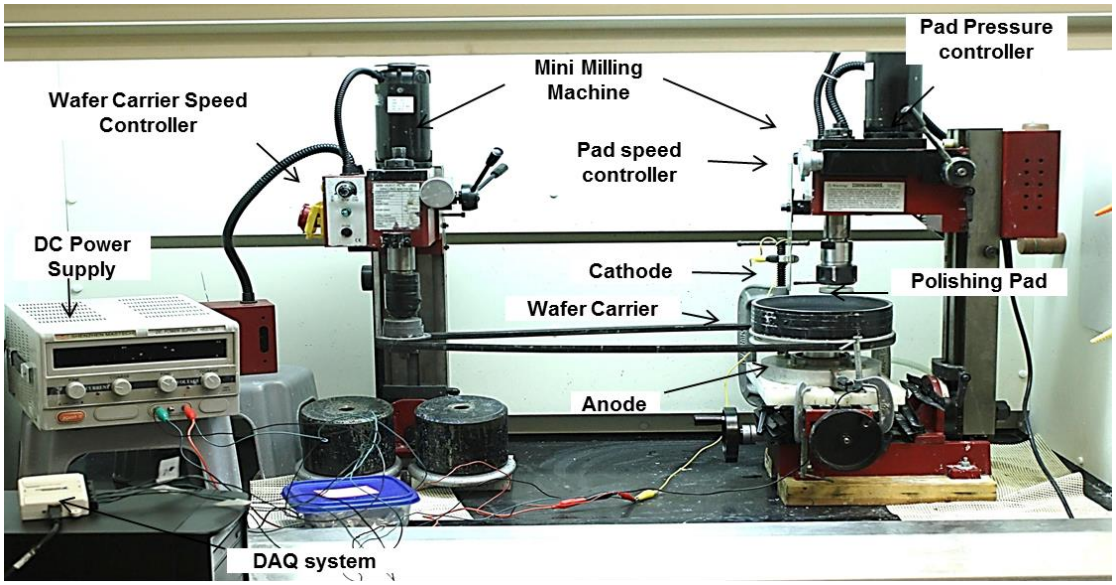

Figure 3-1: ECMP Apparatus

3.2 Sensor Instrumentation

The basic circuit used for signal acquisition from the ECMP process is shown in Figure 3-2. The voltage and current signals from the setup were collected by means of an NI DAQmx data acquisition driver as shown in Figure 3-3. A DC power supply was used to control the anodic potential (V). A 10Ω resistor was connected across the system to measure the process current (I). Three nodes, a_0, a_1 and a_2 of the DAQ driver were assigned to the process current (I), output voltage from the process (V_1), and input anodic potential (V) respectively. The DAQ was linked to Lab VIEW software so that the analog outputs could be converted to continuous signals, which can be recorded from the process. For further analysis, these signals were converted to discrete signals at a sampling rate of 100Hz.

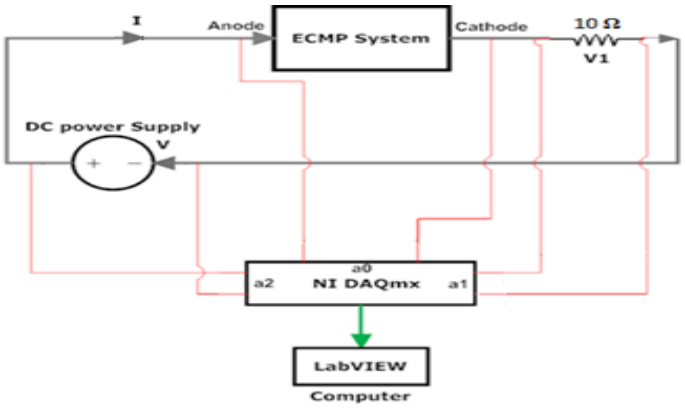

Figure 3-2: Sensor Integrated ECMP circuit [103]

Figure 3-3: NI DAQmx data acquisition [26]

3.3 Experimental Procedure

Buehler Chemomet polishing pad and a standard polishing time of 10 minutes were used in all the experiments. The spindle speed and wafer carrier speed were maintained at 325 RPM and 22 RPM respectively. Phosphoric acid slurry was prepared using a composition of 6% (vol.) of phosphoric acid, 2% (vol.) of ethylene glycol, 0.3% (wt.) of BTA, 4% (wt.) of potassium hydroxide (KOH), 0.45 % (vol.) of H_2O_2, and 0.15% (wt.) of 0.05 µm alumina particles [12]. For each experimental run, the copper wafers were cleaned thoroughly using acetone and distilled water and were subjected to an ultra-sonic cleaning process for 5 minutes. The initial surface roughness of the copper wafers (see

Figure 3-4) was around 22.203 nm. The initial wafer surface contains some shallow scratches made during the slicing of the wafer or from mishandling.

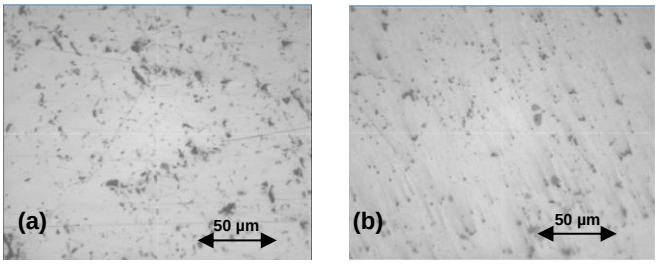

Figure 3-4: Initial condition of copper wafer (a) R_a = 22.203 nm and (b)R_a = 25.858nm

The wafer weight at the beginning and the end of every experimental run was recorded using a Sartorius microbalance [25, 27] as shown in Figure 3-5.

Figure 3-5: Sartorius digital weighing machine [25, 27]

The material removal rate (MRR) was calculated using equation (3-1).

$$MRR = \frac{Initial\ Wt.of\ the\ Cu\ wafer\ (before\ polishing) - Final\ Wt.of\ the\ Cu\ wafer\ \ (after\ polishing)}{Polishing\ Time\ (in\ min.)} \quad (3\text{-}1)$$

The initial and final weights were measured in grams. The surface characteristics were measured using a Nikon Labphot-2© upright optical microscope and a MicroXAM, optical laser interference microscope from ADE Phase Shift Technologies, as shown in Figure 3-6, with up to 0.5 nm resolution [25]. The profile measurements from the MicroXAM were used to estimate R_a.

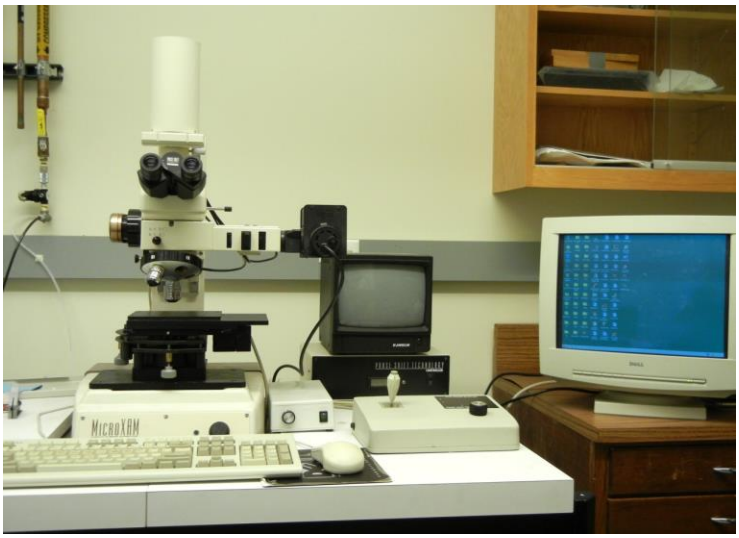

Figure 3-6: MicroXAM, optical laser interference microscope [25]

3.4 Optimization of MRR and R_a with respect to Voltage

A general full-factorial design of experiments (DOE) as shown in Table 3-1 was used in considering three main factors, voltage, pH, and polishing pad angle, to optimize the process parameters. It was found that an operating voltage of 4.5 V (between the transient and trans-passive regions) and a pH range of 6.5 - 6.75, produced the best surface finish and optimum MRR. Figure 3-7 and Figure 3-8 show the initial condition of 2 different Cu wafers having an average surface roughness of 56.82 and 46.89 respectively.

After polishing for 10 minutes under the experimental conditions mentioned above, the average surface roughness was reduced to 11.98 nm and 15.78 nm respectively, as shown in Figure 3-9 and Figure 3-10. The MRR was around 7.66 nm/min and 7.52 nm/min respectively.

Table 3-1: Full factorial design of ECMP experiments

Run	Voltage (V)	pH	Pad Pressure Angle (rpm)
R1	3.5	2.5	360
R2	3.5	2.5	361
R3	3.5	6.5	360
R4	3.5	6.5	361
R5	4.5	2.5	360
R6	4.5	2.5	361
R7	4.5	6.5	360
R8	4.5	6.5	361
R9	5.5	2.5	360
R10	5.5	2.5	361
R11	5.5	6.5	360
R12	5.5	6.5	361

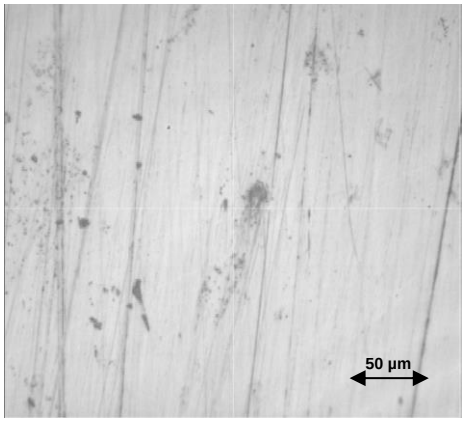

Figure 3-7: Initial condition of wafer 1 (R_a = 56.82 nm)

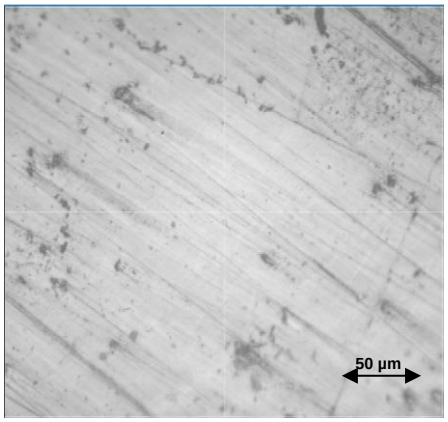

Figure 3-8: Initial condition of wafer 2 (R_a = 46.89 nm)

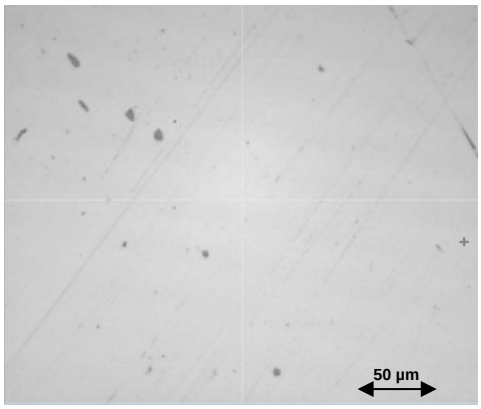

Figure 3-9: Polished wafer 1 after 10 min (R_a = 15.78 nm)

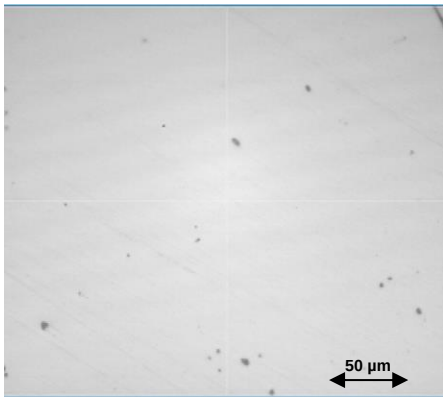

Figure 3-10: Polished wafer 2 after 10 min (R_a = 11.98 nm)

3.5 Analysis of Process Current and Voltage signals

The waveforms of the current and voltage signals revealed some interesting time-frequency patterns. As shown in Figures 3-11 to 3-15, the waveform exhibits a near-stationary and near average periodic pattern interspersed with bursts where the current is close to zero. As summarized in Table 3-2, as the mean-level of the current, and the fraction of time at the level increase (from 40% of the total time at 1 V to 75% at 5 V) with the applied voltage i.e., as the applied voltage increases, the fraction of the

current waveform exhibits higher and near steady behavior near its mean level, and the near-zero current values. The near steady behavior exhibits certain consistent frequency patterns. As shown in Figure 3-16, the frequency portraits show dominant peaks at 0.34 and 5.45 Hz. It may be noted that the frequency of 0.34 corresponds to the RPM of the rotary wafer carrier table and 5.45 Hz to the spindle speed.

Table 3-2: Variation of MRR with anodic voltage and process current signal features

Voltage (V)	Threshold Value	MRR (nm/min)	R_a (nm)	% occurrence of the upper peaks	% occurrence of the down peaks
1	3.29E-05	1.97	25.209	32.87	67.13
2	5.64E-04	1.92	30.901	76.52	23.47
3	0.0174	3.34	16.511	63.39	36.60
4	0.0378	7.52	15.822	75.13	24.86
5	0.0324	7.66	13.709	77.17	22.83

It was also observed from the time portraits of current at various voltages, as shown in Figures 3-11 to 3-15, that the current signal suddenly drops as the passivation film forms and increases as the passivation film is removed as a result of mechanical action enforced by the polishing pad. The average film formation frequency scales in current signals were captured as shown in Figure 3-11.

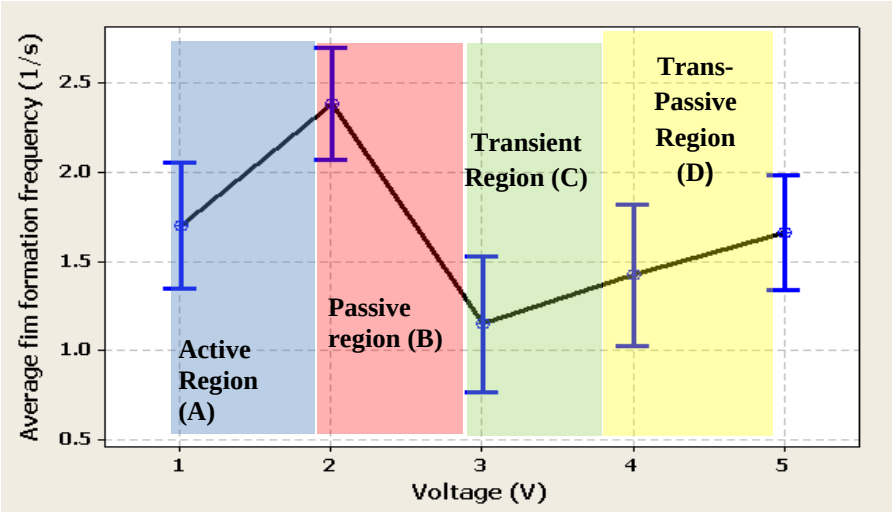

Figure 3-11: Average film formation frequency vs. voltage plot

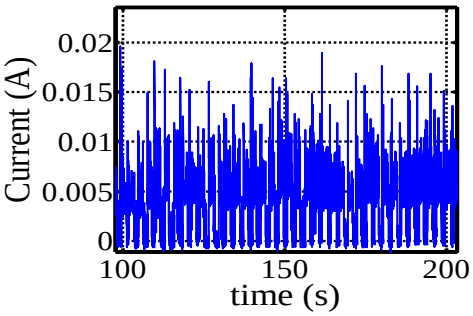

Figure 3-12(a): Time portrait of current at 1V

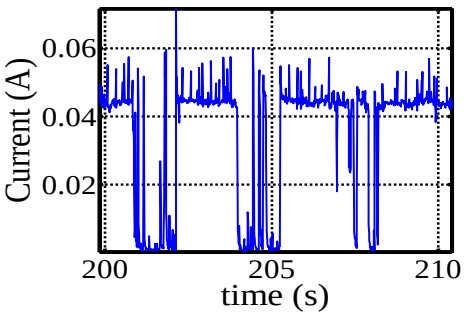

(b) Waveform of current at 1V

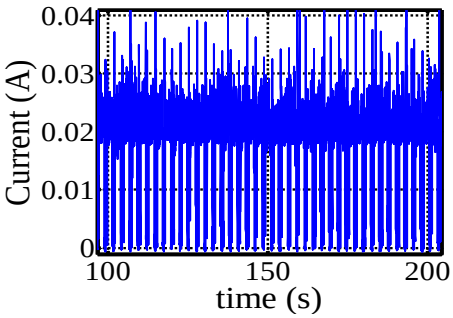

Figure 3-13(a): Time portrait of current at 2V

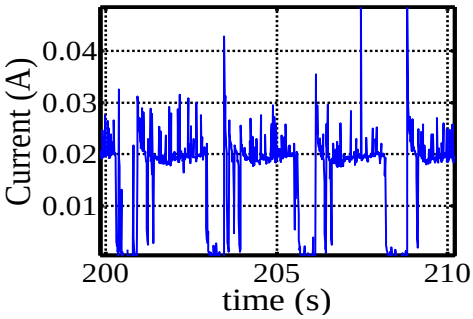

(b) Waveform of current at 2V

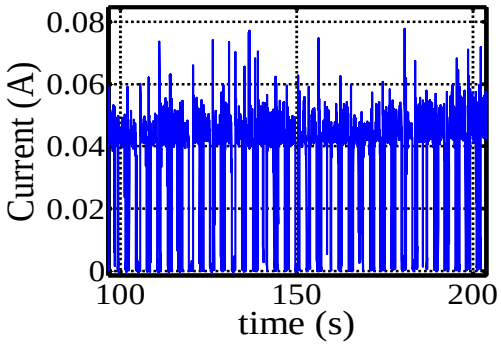

Figure 3-14(a): Time portrait of current at 3V

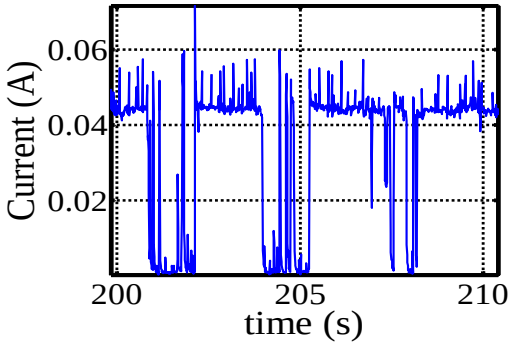

(b) Waveform of current at 3V

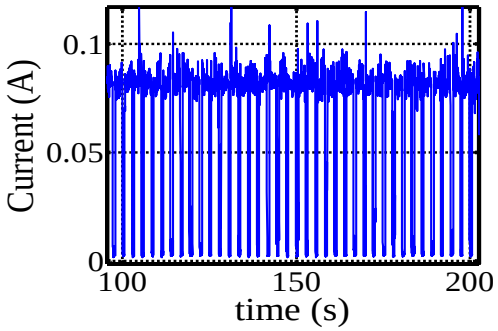

Figure 3-15(a): Time portrait of current at 4V

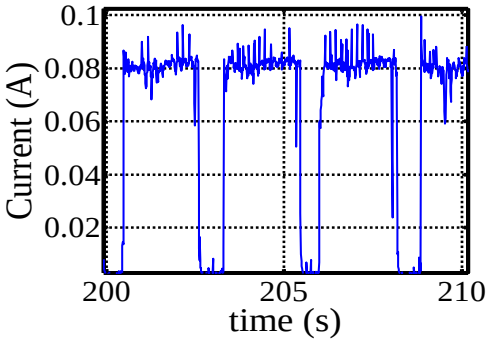

(b) Waveform of current at 4V

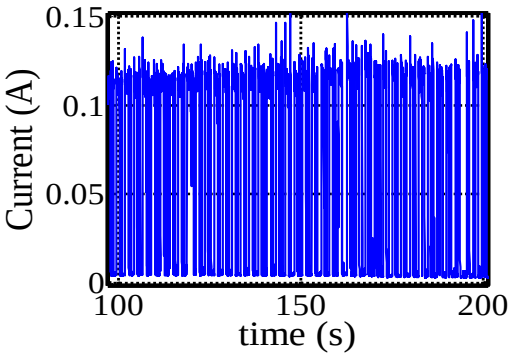

Figure 3-16(a): Time portrait of current at 5V

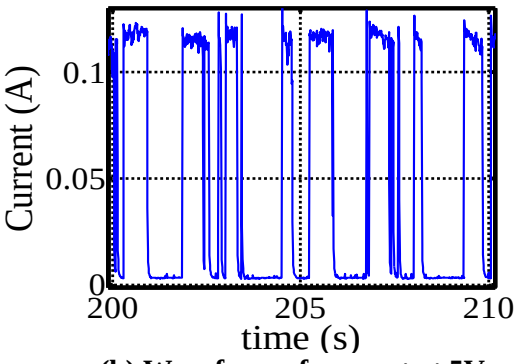

(b) Waveform of current at 5V

3.6 Dynamic analysis of the process current signals

The dynamics of the ECMP process were analyzed by transforming the voltage and current signals from the time domain to the frequency domain using a Fast Fourier Transform (FFT) to map out some of the process parameters such as pad speed, wafer carrier speed, and MRR from the process current signals. The anodic voltage was varied randomly between 1 and 5 V in order to capture the changes in MRR with respect to the applied anodic potential. Figure 3-16 (a) – (e) depict the FFT plots of the process current signal at anodic potentials between 1 and 5 V at a pH of around 6.5. The X axis represents the frequency in Hz and the Y axis represents the amplitude of the current signals. A detailed view of 2 particular windows is shown at the top of each FFT graph. These micrographs depict the magnified view of FFT peaks at *~0.339Hz* and *~5.449Hz.*

From the FFT plots of the process current signals at different anodic potentials, we can identify peaks occurring at *~0.339Hz*, which when multiplied by a time factor of 60 represent the wafer carrier speed of *~22 RPM*. Similarly, the peaks occurring at *~5.449Hz*, which when multiplied by a time factor of 60, represent the head speed of *~325 RPM*.

Similarly we were able to observe that the amplitude of both these peaks is able to depict changes in MRR with variation in the anodic potential of the slurry. There is a gradual increase in the amplitude of the peak at *~0.339Hz* and at *~5.449Hz* with the increase in the anodic potential, which can be seen clearly in the two magnified micrographs. Hence the variation in MRR can be predicted from the amplitude of the peak at *~0.339Hz* and*~5.449Hz.*

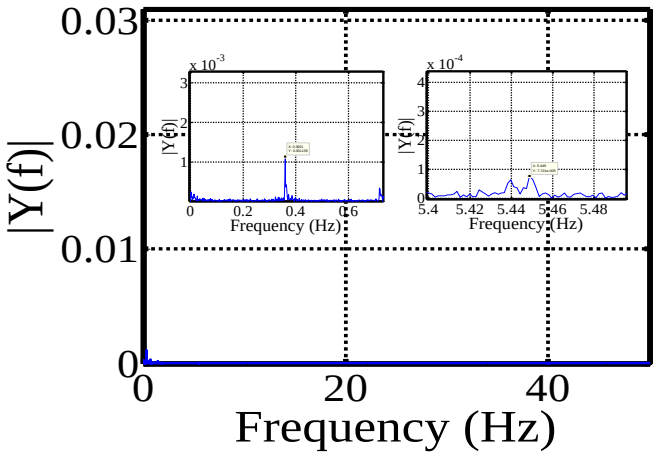

Figure 3-17 (a): FFT plot and Time series of process current at 1 V

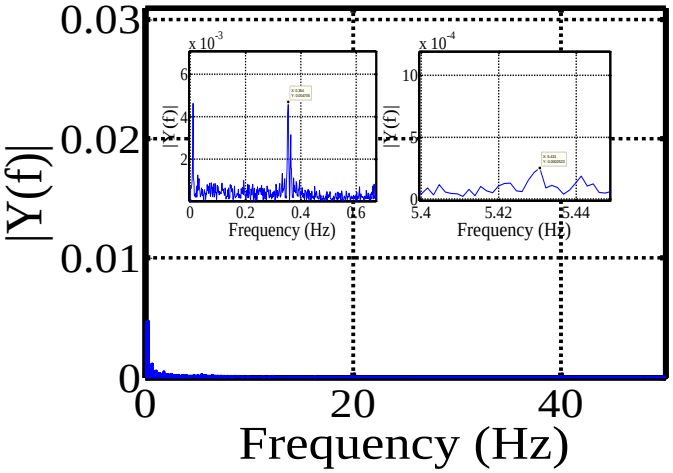

Figure 3-17 (b): FFT plot and Time series of process current at 2V

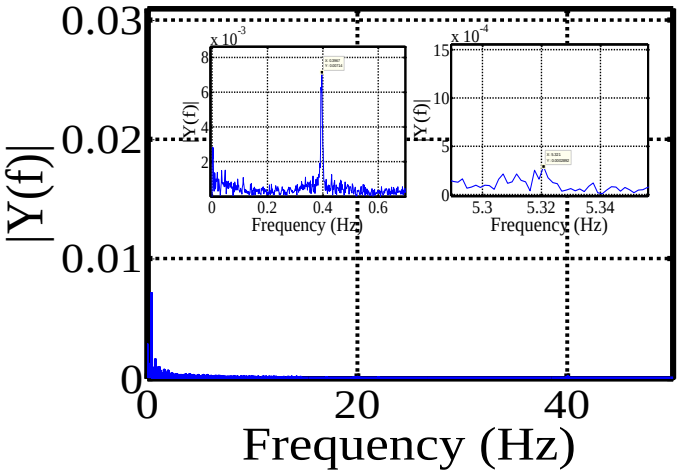

Figure 3-17(c): FFT plot and Time series of process current at 3 V

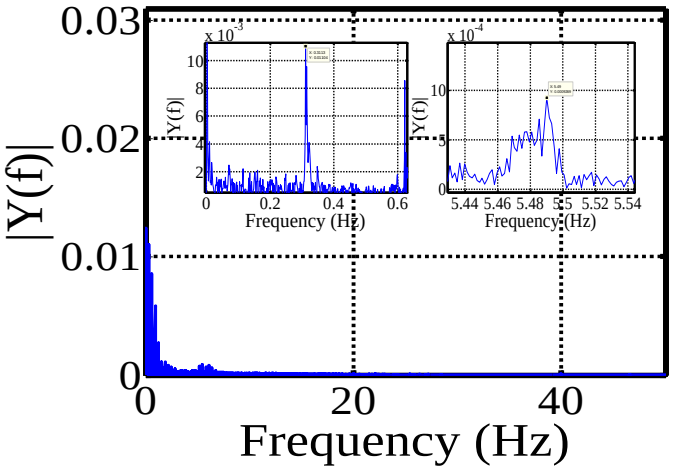

Figure 3-17(d): FFT plot and Time series of process current at 4V

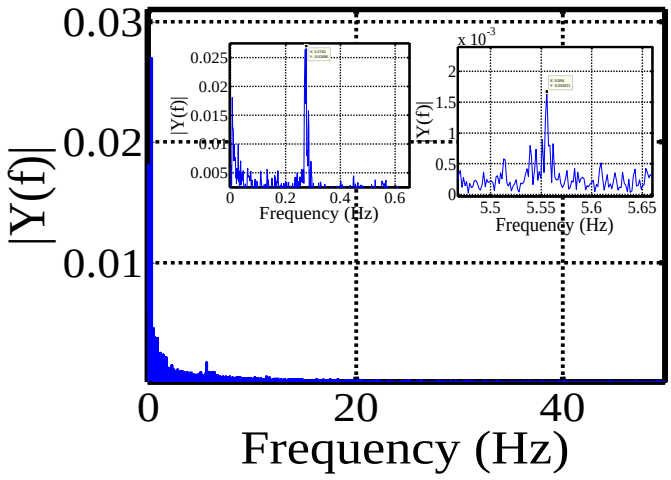

Figure 3-17(e): FFT plot and Time series of Process current at 5 V

The variation of the MRR with respect to the amplitude of the two peaks is depicted in Table 3-4.

Table 3-3: Variation of MRR with amplitude of frequency peak

Anodic Voltage (V)	**Amplitude of peak at** *~0.339Hz*	**Amplitude of peak at** *~5.449Hz*	**MRR (g/min)**
1	0.001139	0.00007721	1.97
2	0.004705	0.0002523	1.92
3	0.00714	0.0002892	3.34
4	0.01104	0.0009269	7.52
5	0.02695	0.001671	7.66

The process characteristic peaks were observed primarily over the 0–5 Hz range. Hence threshold values were fixed as shown in Table 3-4, and all the peaks above the thresholds were considered for further analysis. We were able to clearly observe the electrochemical phase transition in the analysis carried out using 256 samples FFT. FFT analysis of current signals at 1 V over a 0-5V range (shown in the green box in Figure 3-17 (A)-(E) indicates a very low peak magnitude (< 0.4), suggesting the formation of an active region where active dissolution of ions takes place, the R_a is very high, and the MRR is low. As the applied voltage is increased to 2 V, we can see a gradual 3.13% increase in the magnitude of the peaks in the 0 – 5 Hz range. With a further increase in average current, the dissolution of copper ions commences. The R_a value decreases and the MRR increases gradually. At 3 V, the magnitude of the peaks in the 0 – 5 Hz region increases progressively as the average current is increased, indicating the transition to the passive region, the MRR increases rapidly and R_a is also comparatively low. At 4 V the magnitude of the peaks is comparatively higher than at 3 V, as the average current is increasing rapidly, causing passive film to pile up and thus leading to the transient state, where we can observe a good surface finish and very high MRR. Finally, when 5 V are applied, the average current increases sharply, indicating the appearance of peaks having large magnitudes, and a transition from the transient to the trans-passive state. In this phase, we observe a 12-15nm surface finish.

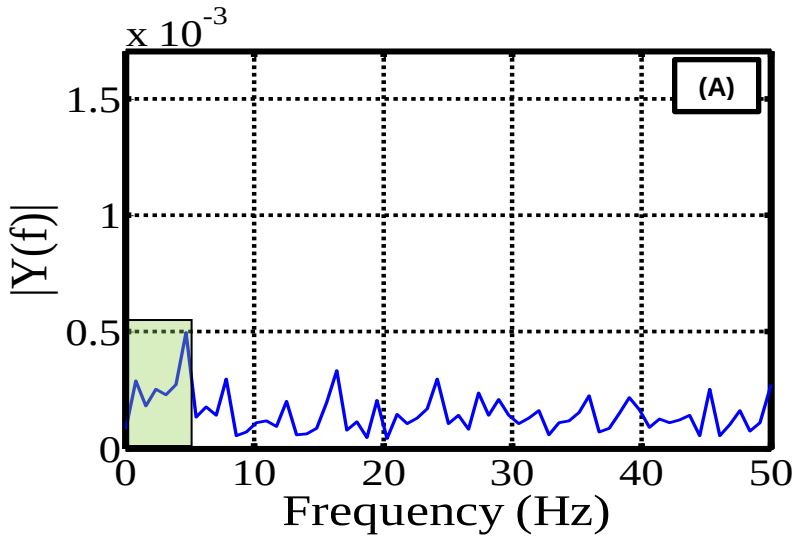
x 10-3
(A)
1.5
1
0.5
0
|Y(f)|
0
10
20
30
40
50
Frequency (Hz)

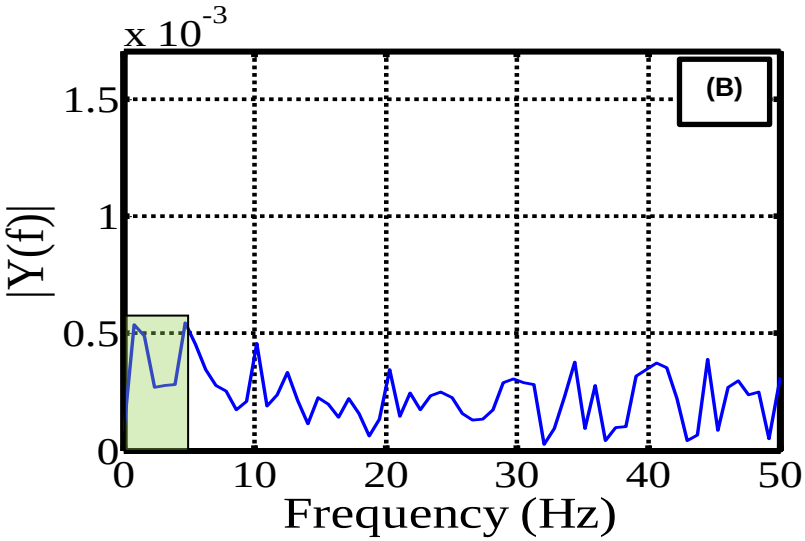
x 10-3
(B)
1.5
1
0.5
0
|Y(f)|
0
10
20
30
40
50
Frequency (Hz)

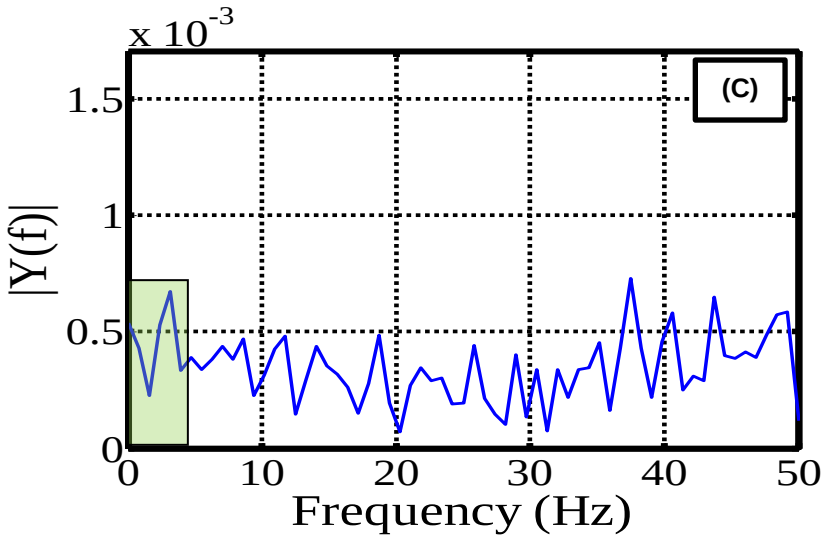
x 10-3
(C)
1.5
1
0.5
0
|Y(f)|
0
10
20
30
40
50
Frequency (Hz)

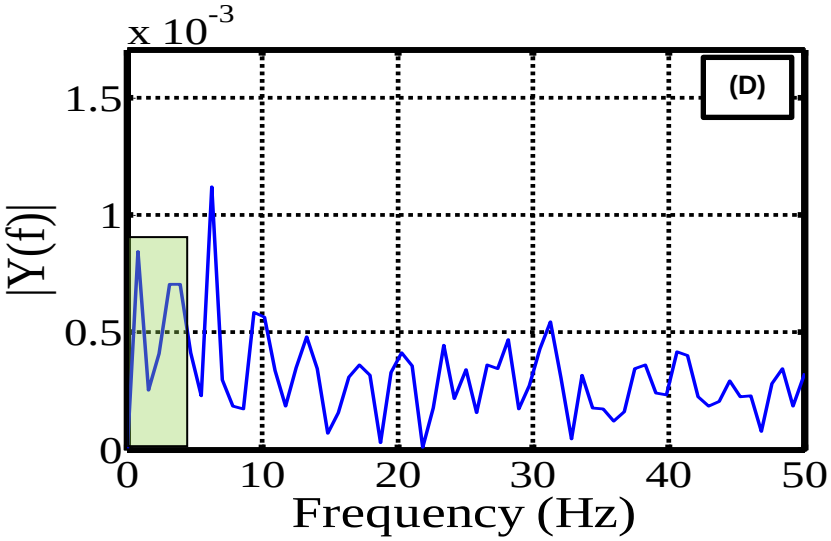
x 10-3
(D)
1.5
1
0.5
0
|Y(f)|
0
10
20
30
40
50
Frequency (Hz)

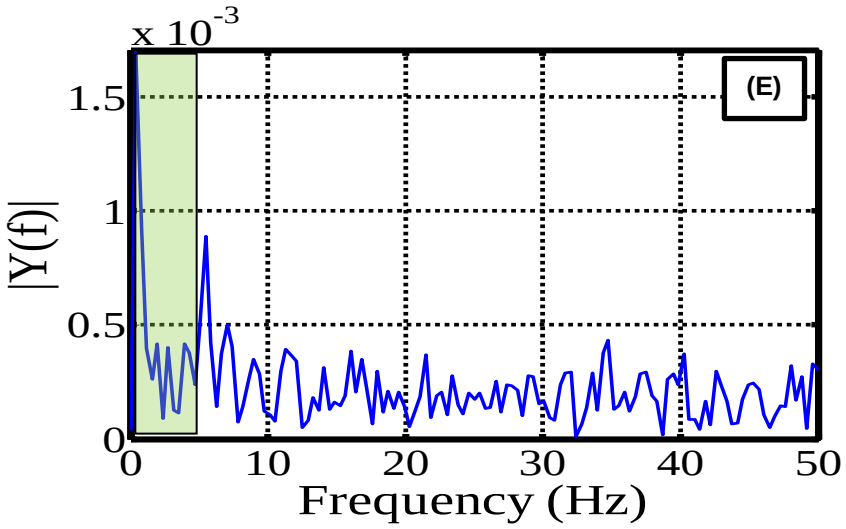

Figure 3-18: FFT of 256 process current peaks above the threshold value at:

(a) 1 V, (b) 2 V, (c) 3 V, (d) 4 V, (e) 5 V

3.7 I-V characteristics

The trends of the I-V characteristics (Figure 3-18) can be used to identify the process conditions and track MRR, R_a and other quality and performance variables of the ECMP process in real-time. In contrast with prevailing approaches to delineating I-V characteristics, we capture not only the first moment and the average trend, but also the time-frequency patterns of the current signals at various applied voltage conditions. As shown in Figure 3-18, the first moment trend indicates that for low applied voltage, < 1 V, the average current of < 0.005 A was noted, corresponding to active dissolution. The average current exhibits a slight increase as the voltage V_1 is increased to 2 V. Upon further increase in V_1 to 3 V, the current shows a marked increase (average current of 0.08 A at 3 V), and increases linearly until 5 V. Upon further increase, the increasing trend becomes somewhat sharper, suggesting a transition from a transient to a trans-passive electrochemical phase.

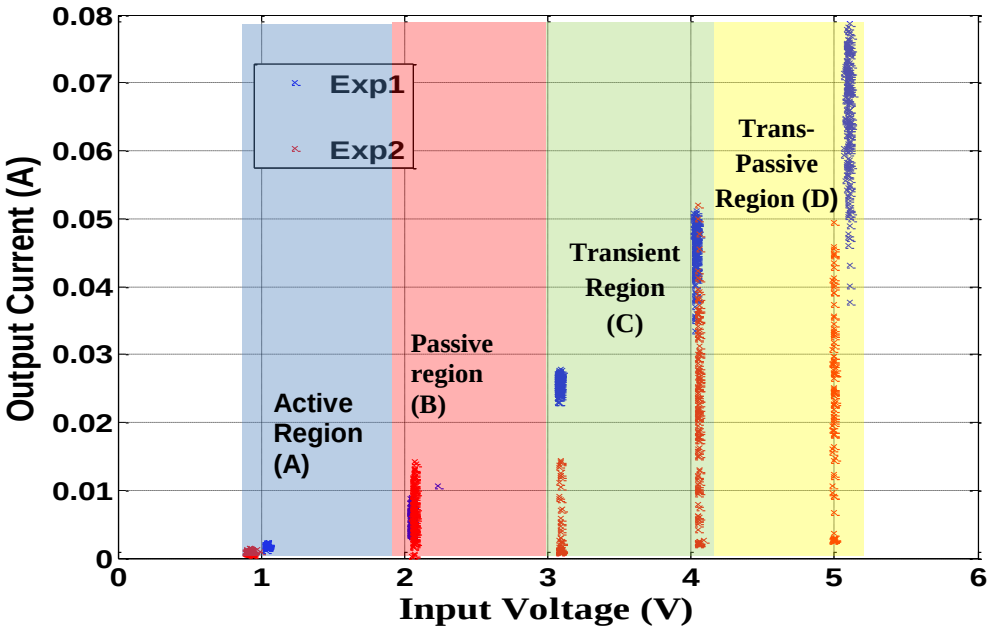

Figure 3-19: I-V curves of H_3PO_4 electrolyte under different voltage conditions

3.8 Introduction to Statistical modeling

A DOE was designed using voltage, pH, pad pressure angle, polishing pad speed and wafer carrier speed as input variables, or the predictors. MRR and R_a were considered the response variables. All the experiments were based on the DOE and signals for all sets of experiments were recorded. Various signal features, statistical features, and non-linear features were extracted from the collected experimental current data.

The current signal features were divided into three parts: statistical, time-frequency, and non-linear features. The response surface methodology (RSM)-based regression modeling was developed to improve the Surface roughness (R_a) and MRR models as follows: statistical features only; statistical and frequency features; statistical, frequency, and non-linear features; statistical, frequency, nonlinear features, and signal peaks features. This model can track roughness and MRR involving linear characteristics, time frequency characteristics, and nonlinear characteristics. The statistically

significant p-value was chosen to be 0.09 [31].

3.9 Regression modeling of material removal rate (MRR)

The current signals obtained from the experiment captured the process dynamics through a good regression fit of the model. Modeling of MRR with process parameters is discussed in section 3.9.1; modeling of MRR with statistical features is discussed in section 3.9.2; modeling of MRR with statistical and energy features is discussed in section 3.9.3; modeling of MRR with statistical, energy, and RQA features is discussed in section 3.9.4; modeling of MRR with signal characteristics only is discussed in section 3.9.5; and modeling of MRR with statistical, energy, RQA features, and current signal characteristics is discussed in section 3.9.6.

3.9.1 Regression model of MRR (nm/min) with process parameters

In this section, the MRR of the copper sample is fitted against process features including their statistically significant two-way interactions. Equation (3-1) gives the regression fit for the MRR. The process parameters, namely voltage, pH and pad pressure angle are used for regression modeling of MRR. Table 3-4 shows the significant values for each of the process parameters. R^2 are found to be 65.8% with df_e = 23. For effective modeling of MRR, process parameters are insufficient. The regression fit for MRR with process parameters is as follows.

$$R^2 = 65.8\%,\ R^2\ (\text{adj.}) = 56.3\%,\ df_e = 19$$

$$\begin{aligned} MRR = {} & 27 + 0.813\,voltage - 25.3\,pH - \\ & 0.065\,pad\_pressure\_angle + 0.0231\,voltage*pH + 0.070\,pH*pad\_pressure\_angle \end{aligned} \quad (3\text{-}1)$$

Table 3-4: Regression model of MRR model using process parameters alone

Predictor	p-value
Constant	0.000
Voltage	0.068
pH	0.045
Pad Pressure Angle	0.008
Voltage*pH	0.145
pH*Pressure Angle	0.092

3.9.2 Regression model of MRR (nm/min) with statistical features

In this section, the MRR of the copper sample is fitted against statistical features, including their statistically significant two-way interactions. Since modeling using process parameters is not sufficient to examine the process, sensor features were extracted for modeling MRR effectively. Equation (3-2) gives the regression model for MRR. Table 3-5 shows the significant value for each of the statistical features and their interactions. Statistical features alone are able to explain some part of the model. However, they are not sufficient for good modeling.

$$R^2 = 78.7\%,\ R^2\,(\text{adj.}) = 71.2\%,\ df_e = 19$$

$$\text{MRR} = 3.83 + 19.6\ \text{PTP} - 0.54\ \text{max} + 0.269\ \text{skew} - 0.766\ \text{kurt} + 20.4\ \text{PTP*skew} + 12.9\ \text{max*kurt} \quad (3\text{-}2)$$

Table 3-5: Regression model of MRR using statistical features

Predictor	p-value
Constant	0.002
Peak to Peak Amplitude	0.053
Maximum	0.621
Skew	0.435
Kurtosis	0.029
Peak to Peak Amplitude*Skewness	0.002
Maximum*Kurtosis	0.000

3.9.3 Regression model of MRR (nm/min) with statistical features and energy features

Equation (3-3) gives the regression fit incorporating energy features from the spectrogram as well as the statistical features. Table 3-6 shows the significant value for each of the statistical features, energy features, and their interactions. The model performances using the statistical features alone are not sufficient for good estimation of the MRR; therefore, energy features were incorporated into it. The energy features from the spectrogram were calculated at 5-10 Hz. For this model, two energy features were extracted using MATLAB. After adding energy features, there was approximately a 9% increase in the R^2 value.

$$R^2 = 87.0\%,\ R^2\ (\text{adj.}) = 77.0\%,\ df_e = 14$$

$$\begin{aligned} MRR = {} & 2.55 + 82.7\ mean - 2.30\ cov - 0.340\ skew - 0.107\ alpha + 0.076\ gamma - 0.552\ max - \\ & 0.043\ cov*alpha - 0.0028\ skew*gamma + 5.94\ skew*max + 0.497\ max*alpha \end{aligned} \quad (3\text{-}3)$$

Table 3-6: Regression model of MRR using statistical and energy features

Predictor	p-value
Constant	0.000
Mean	0.005
Covariance	0.056
Skewness	0.025
Energy α,db	0.187
Energy γ,db	0.048
Maximum	0.053
Covariance* Energy α,db	0.007
Skew* Energy γ,db	0.082
Skew*Maximum	0.412
Maximum* Energy α,db	0.076

3.9.4 Regression model of MRR (nm/min) with statistical, energy, and RQA features

As shown in section 3.5, current signals are found to be nonlinear; therefore, nonlinear features were added to the model. Equation (3-4) gives the regression model for MRR. Table 3-7 shows the significant values for each of the statistical, energy, and RQA features and their interactions. This model leads to a decrease in R^2 value by about 5%.

$$R^2 = 82.1\%,\ R^2\ (\text{adj.}) = 75.7\%,\ df_e = 13$$

$$\begin{aligned} MRR = {} & 6.47 + 0.63\ max + 1.49\ skew - 0.237\ lam - 1.26\ Lmax - 0.005\ gamma - 8.60 max*skew - 2.13 \\ & max*lam + 19.6\ max*Lmax - 0.00598\ lam*gamma + 0.0090\ Lmax*gamma + 0.090\ max*gamma \end{aligned} \quad (3\text{-}4)$$

Table 3-7: Regression modeling of MRR using statistical, energy, and RQA features

Predictor	p-value
Constant	0.042
Maximum	0.066
Skewness	0.055
lam	0.424
Lmax	0.095
Energy γ,db	0.036
Maximum*skewness	0.078
Maximum*lam	0.102
Maximum* Lmax	0.095
lam* Energy γ,db	0.127
Lmax* Energy γ,db	0.054
Maximum* Energy γ,db	0.286

3.9.5 Regression model of MRR (nm/min) with signal characteristics only

Equation (3-5) gives the regression model for MRR using signal characteristics only. Table 3-8 shows significant values for each of the signal characteristics and their interactions. The signal characteristics are the duration of upper peaks and lower peaks.

$$R^2 = 47.3\%,\ R^2\ (\text{adj.}) = 37.1\%,\ df_e = 19$$

$$\text{MRR} = -15.3 - 10.5\ \text{up*down} + 1.81\ \text{up*up} - 2.62\ \text{down*down} + 5.4\ \text{ups} + 24.0\ \text{downs} \quad (3\text{-}5)$$

Table 3-8: Regression modeling of MRR using signal characteristics only

Predictor	p-value
Constant	0.125
Duration of upper peaks	0.027
Duration of lower peaks	0.091
Duration of upper peaks*Duration of lower peaks	0.234
Duration of upper peaks* Duration of upper peaks	0.374
Duration of lower peaks* Duration of lower peaks	0.098

3.9.6 Regression model of MRR (nm/min) with statistical, energy features, RQA and signal characteristics features

Equation (3-6) gives the regression model for MRR. Table 3-9 shows the significant value of each of the statistical, energy, RQA, and signal characteristics and their interactions. After adding signal characteristics, the R^2 of the model increased to 91.8%. Since the p-value of the interactions is below 0.09, they are statistically significant.

$$R^2 = 91.8\%,\ R^2\ (\text{adj.}) = 81.1\%,\ df_e = 11$$

$$\begin{aligned} MRR = {} & 25.2 - 0.89\ max - 0.399\ kurt + 0.197\ alpha + 0.0584\ gamma + 0.0179\ lam - \\ & 0.642\ Lmax + 4.95\ upper\_peak + 0.045\ lower\_Peak + 0.00001\ lam*lam + \\ & 1.29\ max*kurt - 0.0173\ kurt*Lmax + 0.126\ alpha*up + 0.0058\ lam*Lmax \end{aligned} \quad (3\text{-}6)$$

Table 3-9: Regression modeling of MRR using statistical, energy, RQA, and Signal characteristics

Predictor	p-value
Constant	0.004
Maximum	0.047
Kurtosis	0.605
Energy α,db	0.007
Energy γ,db	0.271
lam	0.085
Lmax	0.242
Duration of upper peaks	0.055
Duration of lower peaks	0.097
lam*lam	0.081
Maximum*Kurtosis	0.039
Kurtosis*Lmax	0.014
Energy α,db* Duration of upper peaks	0.026
lam*Lmax	0.065

Table 3-10 summarizes all the MRR regression models.

Table 3-10: Sensor fusion based MRR estimation

Features	R^2	R^2(adj.)	R^2 (Pred.)	df_e
Process parameters	65.8	56.3	44.7	19
Statistical Features	78.7	71.2	60.3	18
Statistics + Energy Features	87.0	77.0	74.1	14
Statistics+Energy+RQA	82.1	75.7	70.5	13
Signal Characteristics	47.3	37.1	31.3	19
Statistics+Energy+RQA+Signal characteristics	91.8	81.1	72.5	11

3.10 Regression modeling of Surface Roughness

In this section, the roughness of the copper sample is fitted against sensor features using response surface analysis including two-way interactions of the features which are found to be statistically significant in the model. The current signal was found to capture the dynamics using a regression fit. Modeling of surface roughness with process parameters is discussed in section 3.10.1; modeling of surface roughness with statistical features is discussed in section 3.10.2; modeling of surface roughness with statistical and energy features is discussed in section 3.10.3; modeling of surface roughness with statistical, energy, and RQA features is discussed in section 3.10.4; modeling of surface roughness with signal characteristics only is discussed in section 3.10.5; and modeling of surface roughness with statistical, energy, RQA ,and signal characteristics is discussed in section 3.10.6.

3.10.1 Regression model of Surface Roughness (nm) with process features

In this section, the surface roughness of the copper sample is fitted against process features, including their statistically significant two-way interactions. The process parameters, namely voltage, pH and pad pressure angle are used for regression modeling of surface roughness. Table 3-11 shows the significant values for each of the process parameters. The R^2 is found to be 64.5% with df_e =19. For effective modeling of MRR, process parameters are insufficient. The regression fit for R_a with process parameters is as follows

$$R^2 = 64.5\%,\ R^2\ (\text{adj.}) = 54.7\%,\ df_e = 19$$

$$\begin{aligned} Ra = {} & -513 - 1.68\ \text{voltage} + 38\ \text{pH} + 1.50\ \text{pad\_pressure\_angle} + \\ & 0.062\text{voltage*pH} - 0.107\text{pH*pad\_pressure\_angle} \end{aligned} \tag{3-7}$$

Table 3-11: Regression model of R_a model using machine parameters alone

Predictor	p-value
Constant	0.224
Voltage	0.026
pH	0.032
Pad Pressure Angle	0.253
Voltage*pH	0.148
pH*Pressure Angle	0.005

3.10.2 Regression model of surface roughness (nm) with statistical features

In this section, the surface roughness of the copper sample is fitted against statistical features, including the statistically significant two-way interactions. As, the model using process parameters is not sufficient to investigate the process, statistical features were extracted for modeling surface roughness effectively. Equation (3-8) gives the regression model for MRR. Table 3-12 shows the significant value for each of the statistical features and their interactions. The R^2 is 80.5% with df_e =18. Statistical features alone are able to explain some part of the model. However, they are not sufficient for good modeling. The surface roughness model using statistical features is given as follows.

$$R^2 = 80.5\%,\ R^2\ (\text{adj.}) = 73.7\%,\ df_e = 18$$

$$Ra = 15.8 + 26.2PTP - 0.55\ max - 0.101skew - 0.937kurt + 20.7\ PTP*skew + 12.5max*kurt \quad (3\text{-}8)$$

Table 3-12: Regression model of MRR using statistical features

Predictor	p-value
Constant	0.000
Peak to Peak Amplitude	0.011
Maximum	0.006
Skew	0.085
Kurtosis	0.060
Peak to Peak Amplitude*Skewness	0.002
Maximum*Kurtosis	0.000

3.10.3 Regression model of surface roughness (nm) with statistical and energy features

Equation (3-9) gives the regression fit incorporating energy features from the spectrogram as well as the statistical features. Table 3-13 shows the significant value for each of the statistical and energy features and their interactions. The model performance using the statistical features alone is not sufficient for good estimation of the surface roughness; therefore, energy features were incorporated into it. The energy features such as energy α,db and energy γ,db from the spectrogram were calculated at 5-10 Hz. For this model, two energy levels are extracted using Matlab. After adding energy features, there was approximately an 8% increase in the R^2 value.

$$R^2 = 88.7\%,\ R^2\ (\text{adj.}) = 80.0\%,\ df_e = 14$$

$$\begin{aligned} Ra = {} & 19.8 + 87.8\ \text{mean} - 15.3\ \text{cov} + 0.583\ \text{skew} - 0.132\ \text{alpha} + \\ & 0.191\ \text{gamma} + 0.71\ \text{max} - 0.274\ \text{cov*alpha} + 0.0009\ \text{skew*gamma} \\ & + 9.25\ \text{skew*max} + 0.331\ \text{max*alpha} \end{aligned} \tag{3-9}$$

Table 3-13: Regression model of MRR using statistical and energy features

Predictor	p-value
constant	0.096
Mean	0.009
Covariance	0.179
Skewness	0.025
Energy α,db	0.165
Energy γ,db	0.015
Maximum	0.048
Covariance* Energy α,db	0.066
Skew* Energy γ,db	0.094
Skew*Maximum	0.282
Maximum* Energy α,db	0.029

3.10.4 Regression model of surface roughness (nm) with statistical, energy, and RQA features

In this, the roughness of the copper is fitted against statistical, energy, and RQA features, including their statistically significant two-way interactions. As shown in section 3.6, current signals are nonlinear; therefore nonlinear features to capture nonlinearity were added in the model. Equation (3-10) gives the regression model for surface roughness. Table 3-14 shows the significant value for each of the statistical, energy, and RQA features and their interactions. This model leads to a decrease in R^2 value of approximately 6%.

$$R^2 = 82.6\%,\ R^2\ (\text{adj.}) = 76.6\%,\ df_e = 13$$

$$\begin{aligned} Ra = {} & 21.5 - 0.25\ max + 1.43\ skew - 0.210\ lam - 0.42\ Lmax + 0.051\ gamma \\ & - 9.06\ max*skew - 1.99\ max*lam + 16.2\ max*Lmax - 0.00550\ lam*gamma \\ & + 0.0140\ Lmax*gamma - 0.059\ max*gamma \end{aligned} \tag{3-10}$$

Table 3-14: Regression modeling of MRR using statistical, energy, and RQA features

Predictor	p-value
constant	0.041
Maximum	0.087
Skewness	0.079
lam	0.035
Lmax	0.803
Energy γ,db	0.066
Maximum*Skewness	0.037
Maximum*lam	0.019
Maximum* Lmax	0.021
lam* Energy γ,db	0.054
Lmax* Energy γ,db	0.274
Maximum* Energy γ,db	0.007

3.10.5 Regression model of surface roughness (nm) with signal characteristics only

In this model, the roughness of the copper sample is fitted against signal characteristics only. Equation (3-11) gives the regression model for surface roughness using signal characteristics only. Table 3-15 shows the significant value for each of the signal characteristics and their interactions. The signal characteristics are the duration of upper peaks and of lower peaks.

$$R^2 = 36.5\%,\ R^2\ (\text{adj.}) = 24.3\%,\ df_e = 19$$

$$Ra = 62.6 + 37.5\ up*down - 16.1\ up*up - 18.6\ down*down - 1.0\ ups - 2.0\ downs \quad (3\text{-}11)$$

Table 3-15: Regression modeling of surface roughness using signal characteristics only

Predictor	p-value
Constant	0.275
Duration of upper peaks	0.091
Duration of lower peaks	0.037
Duration of upper peaks*Duration of lower peaks	0.025
Duration of upper peaks* Duration of upper peaks	0.984
Duration of lower peaks* Duration of lower peaks	0.049

3.10.6 Regression model of surface roughness (nm) with statistical, energy, RQA, and signal characteristic features :

In this model, the roughness of the copper sample is fitted against vibration and temperature sensor features, including their statistically significant two-way interactions. Equation (3-12) gives the regression model for surface roughness. Table 3-16 shows the significant value of each of the statistical, energy, RQA, and signal characteristic features and their interactions. After adding signal characterstics, the R^2 of the model increases to 92%. Since the p-value of the interactions is below 0.09, they are statistically significant.

$$R^2 = 92.0\%,\ R^2\ (\text{adj.}) = 81.7\%,\ df_e = 11$$

$$\begin{aligned} Ra = {} & 35.6 - 0.90\ max - 0.365\ kurt + 0.174\ alpha + 0.0520\ gamma + 0.0204\ lam - \\ & 0.680\ Lmax + 5.84\ upper\_peak - 0.154\ lower\_peak - 0.00127\ lam*lam + \\ & 2.89\ max*kurt - 0.0033\ kurt*Lmax + 0.144\ alpha*up + 0.0147\ lam*Lmax \end{aligned} \quad (3\text{-}12)$$

Table 3-16: Regression modeling of surface roughness using statistical, energy, RQA, and Signal characteristic features

Predictor	p-value
Constant	0.001
Maximum	0.048
Kurtosis	0.067
Energy α,db	0.016
Energy γ,db	0.340
lam	0.232
Lmax	0.079
Duration of upper peaks	0.033
Duration of lower peaks	0.086
lam*lam	0.062
Maximum*Kurtosis	0.059
Kurtosis*Lmax	0.003
Energy α,db* Duration of upper peaks	0.016
lam*Lmax	0.029

Table 3-17 summarizes all surface roughness regression models.

Table 3-17: Sensor fusion based surface roughness estimation

Features	R^2	R^2(adj.)	R^2 (pred.)	df_e
Process parameters	64.5	54.7	42.5	19
Statistical Features	80.5	73.7	65.4	18
Statistics + Energy Features	88.7	80.0	76.2	14
Statistics+Energy+RQA	82.6	76.6	68.6	13
Signal Characteristics	36.5	24.3	21.4	19
Statistics+Energy+RQA+Signal characteristics	92.0	81.7	74.7	11

Response optimizer was used to determine the process conditions to optimize the material removal rate (MRR) and surface finish (R_a) as shown in Figure 3-20.

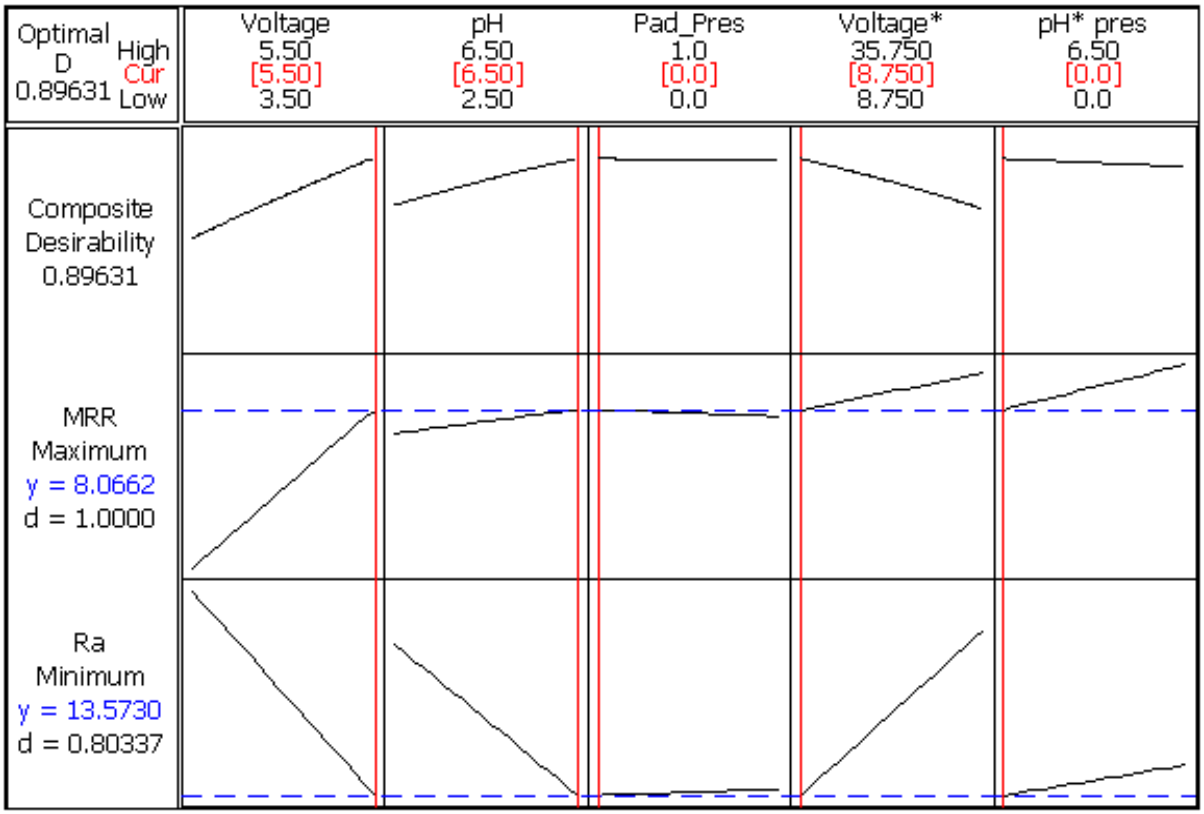

Figure 3-20: Response optimizer plot

3.11 Confirmation Experiments

A confirmation experiment was run to verify the process conditions as shown in Table 3-18 to optimize MRR and surface roughness (R_a) obtained through statistical model predicting MRR and Surface roughness.

Table 3-18: Optimal process conditions

Factors	Optimized Value
Voltage (V)	4.5
pH	6.5
Pad pressure angle (degree)	0

Phosphoric acid based slurry, Buehler Chemomet polishing pad, and a standard polishing time of 10 minutes was used in the experiment. The spindle speed and wafer carrier speed were maintained at 325 RPM and 22 RPM respectively. The initial condition and final condition of the copper wafer are shown in Figure 3-21 and 3-22 respectively.

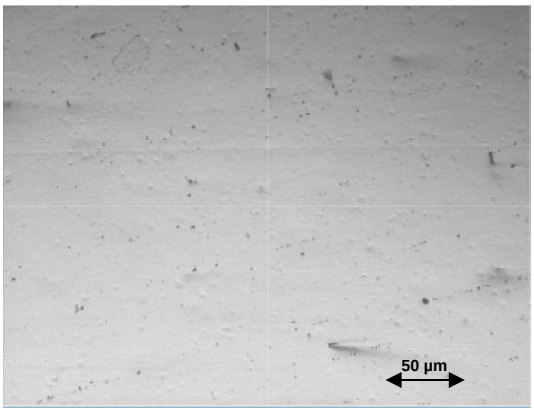

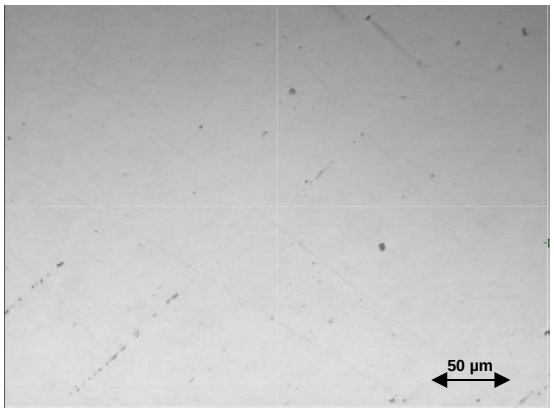

Figure 3-21: Initial condition of Cu wafer **Figure 3-22: Final condition of Cu wafer**

The material removal rate (MRR) was calculated to be around 8.69 nm/min and the surface finish was reduced from 30.25 nm to 15.57 nm in 10 minutes.

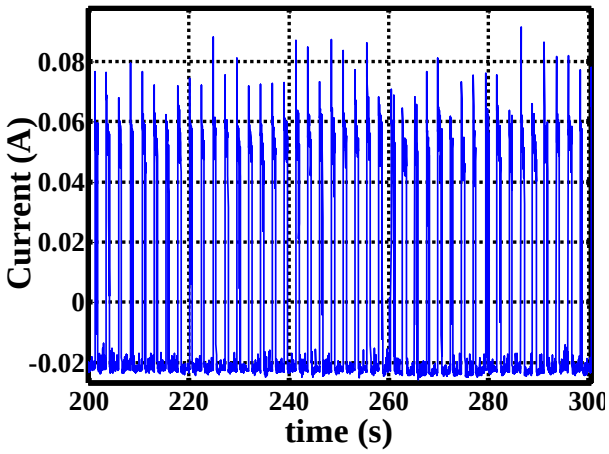

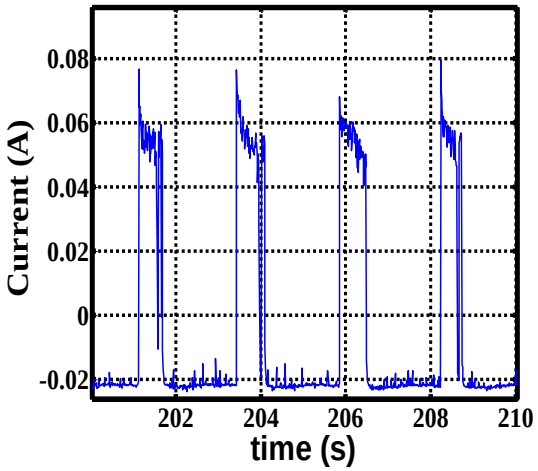

Figure 3-23(a): Time portrait of current at 4.5V **(b) Waveform of current at 4.5V**

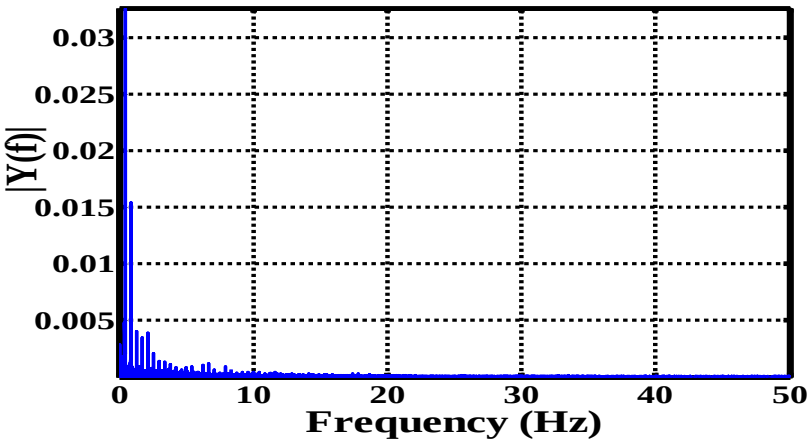

Figure 3-24: FFT plot of current at 4.5V

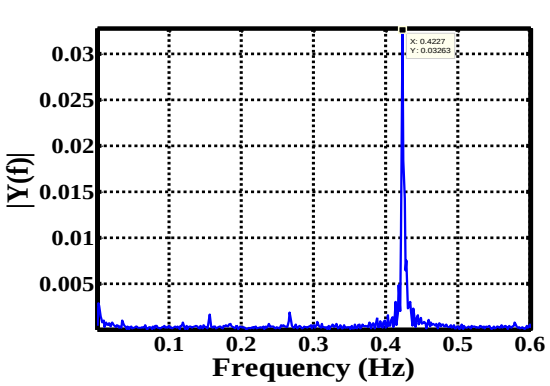

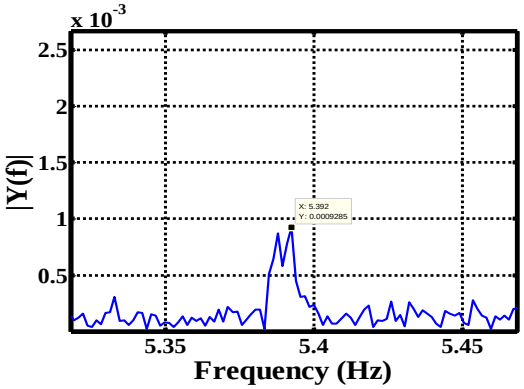

Figure 3-24(a): Wafer carrier speed frequency **Figure 3-24(b): Polishing pad speed frequency**

From Figure 3-23 we can clearly observe that the amplitude of current varies between - 0.02A to 0.08A with average passivation film time scale of 0.00041s. From Figure 3-24, we can clearly observe the magnitude of the peak depicting the wafer carrier speed frequency *~0.4227 Hz* is 0.03263 and the magnitude of the peak depicting the polishing pad speed frequency *~5.392 Hz* is 0.0009285. Figures 3-25a – 3-25f were plotted taking the predicted MRR as the mean and the model standard deviation and fitting a normal distribution. Distribution limits such as $\mu\pm\sigma$, $\mu\pm2\sigma$, $\mu\pm3\sigma$ were considered for building the normal curve plot.

In detail, Figure 3-25a shows the actual realizations of MRR from confirmation experiments superposed on the MRR estimates (the mean and the standard deviation) from the regression model shown in Eq. (3-1). Since R^2 is rather low (65.8%), the realizations were outside the 6S range.

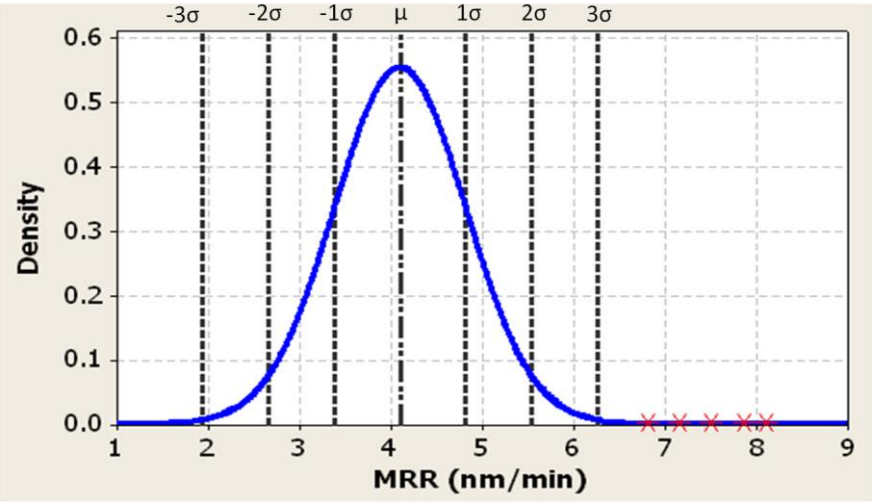

Figure 3-25a: Confirmation run plot considering process parameters

In detail, Figure 3-25b shows the actual realizations of MRR from confirmation experiments superposed on the MRR estimates (the mean and the standard deviation) from the regression model shown in Eq. (3-2). Since R^2 is rather low (78.7%), the realizations were outside the 6S range.

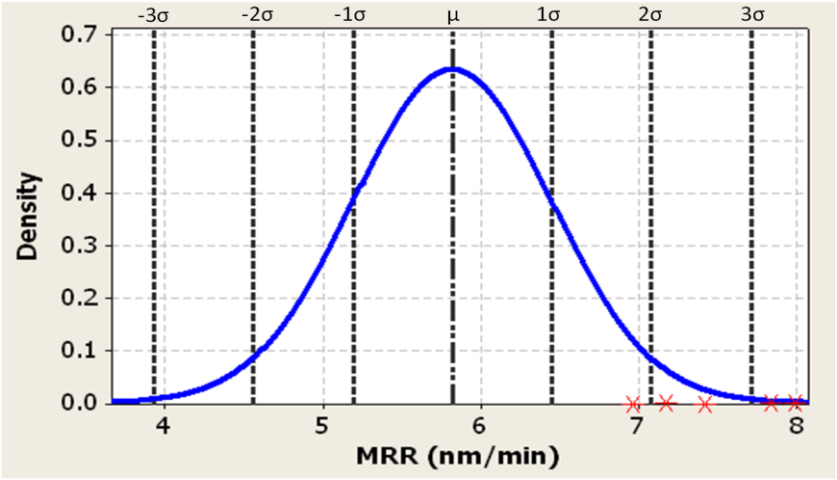

Figure 3-25b: Confirmation run plot considering statistical features

In detail, Figure 3-25c shows the actual realizations of MRR from confirmation experiments superposed on the MRR estimates (the mean and the standard deviation) from the regression model shown in Eq. (3-3). Since R^2 is rather low (87.0%), the realizations were outside the 6S range.

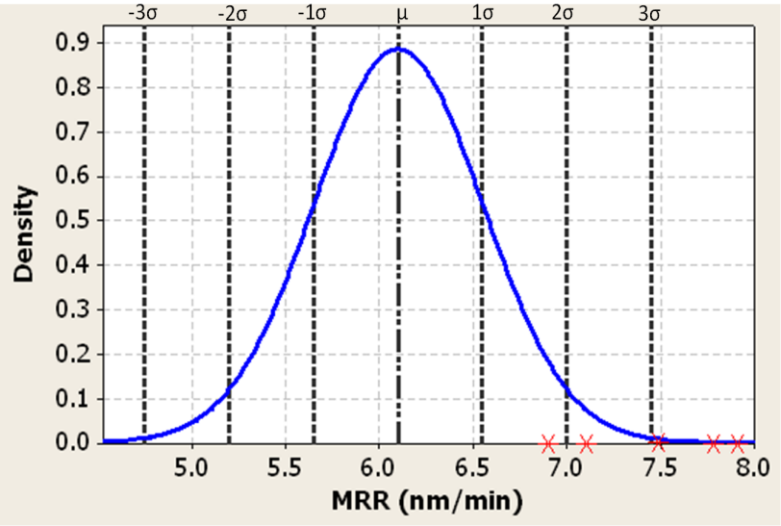

Figure 3-25c: Confirmation run plot considering statistical and energy features

In detail, Figure 3-25d shows the actual realizations of MRR from confirmation experiments superposed on the MRR estimates (the mean and the standard deviation) from the regression model shown in Eq. (3-4). Since R^2 is rather low (82.1%), the realizations were outside the 6S range.

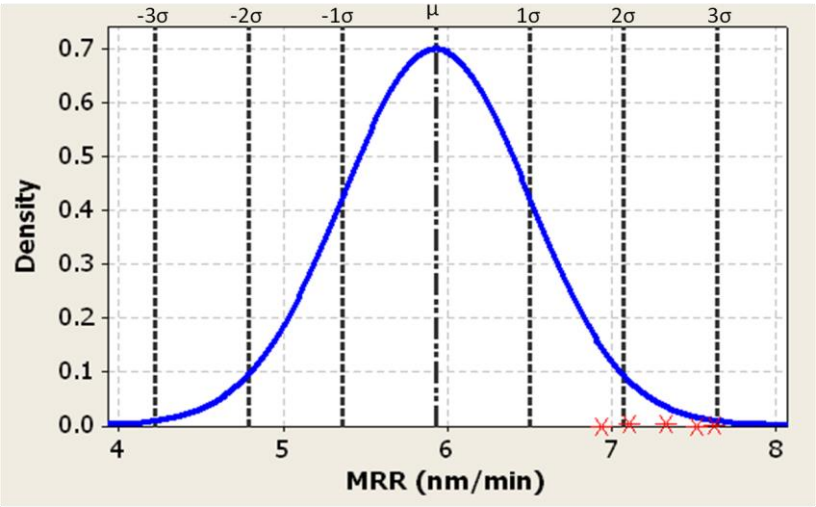

Figure 3-25d: Confirmation run plot considering statistical, energy and RQA features

In detail, Figure 3-25e shows the actual realizations of MRR from confirmation experiments superposed on the MRR estimates (the mean and the standard deviation) from the regression model shown in Eq. (3-5). Since R^2 is rather low (47.3%), the realizations were outside the 6S range.

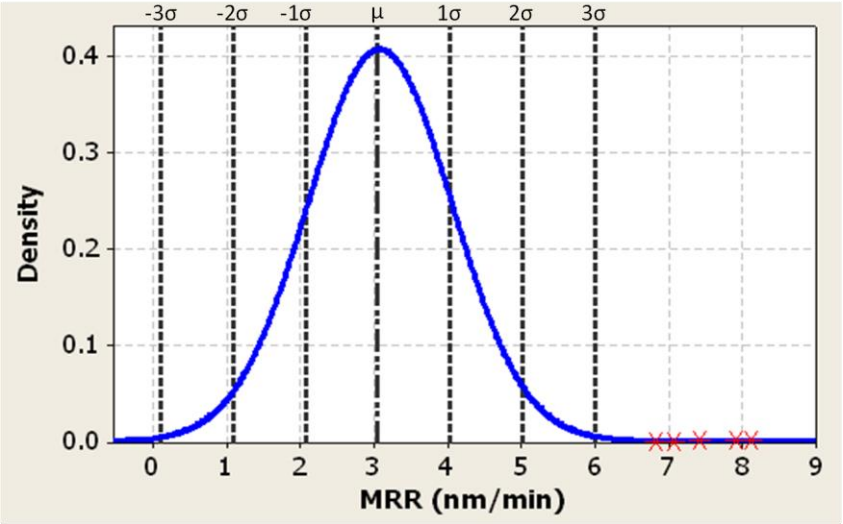

Figure 3-25e: Confirmation run plot considering signal characteristics

In detail, Figure 3-25f shows the actual realizations of MRR from confirmation experiments superposed on the MRR estimates (the mean and the standard deviation) from the regression model shown in Eq. (3-6). Since R^2 is rather low (91.8%), the realizations were outside the 6S range.

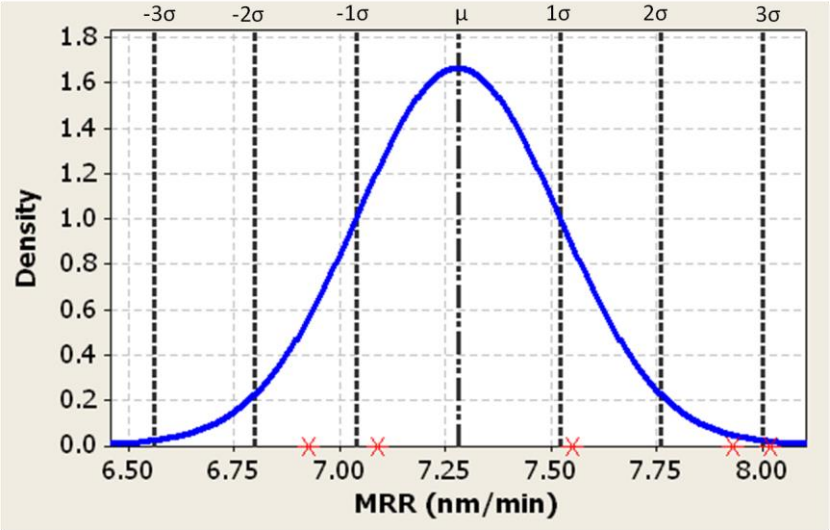

Figure 3-25f: Confirmation run plot considering statistics, energy, RQA & signal characteristics

In summary, we can observe that the statistical model built using process parameters, statistical features, energy features, RQA features, and signal characteristics having R^2 value of 91.8% can be effectively used to predict MRR as optimized experimental run results lie within the 6σ range. The optimized experimental run results lie within the 6σ range when the R^2 value is high and lie outside the 6σ range when the R^2 value is low.

Figures 3-26a – 3-26f were plotted taking the predicted R_a as the mean and the model standard deviation and fitting a normal distribution. Distribution limits such as μ±σ, μ±2σ, μ±3σ were considered for building the normal curve plot. In detail, Figure 3-26a shows the actual realizations of R_a from confirmation experiments superposed on the R_a estimates (the mean and the standard deviation) from the regression model shown in Eq. (3-7). Since R^2 is rather low (64.5%), the realizations were outside the 6S range.

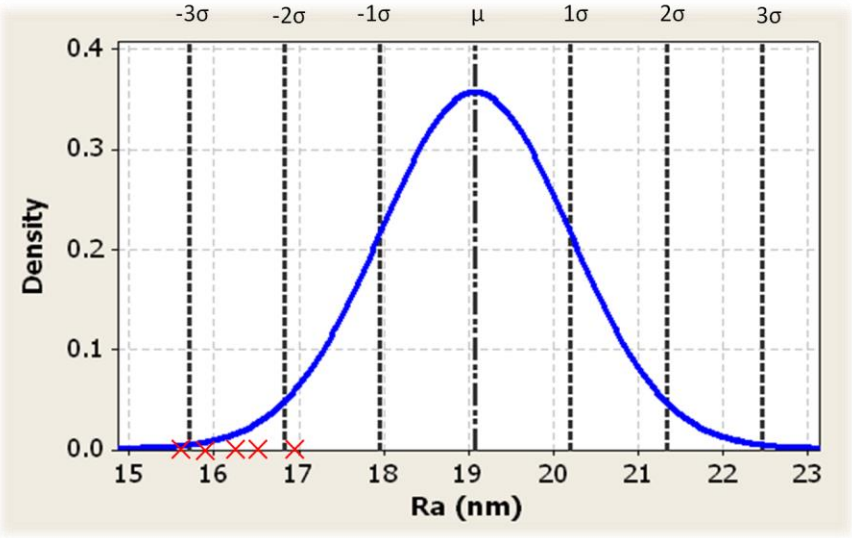

Figure 3-26a: Confirmation run plot considering process parameters

Figure 3-26b shows the actual realizations of R_a from confirmation experiments superposed on the R_a estimates (the mean and the standard deviation) from the regression model shown in Eq. (3-8). Since R^2 is rather low (80.5%), the realizations were outside the 6S range.

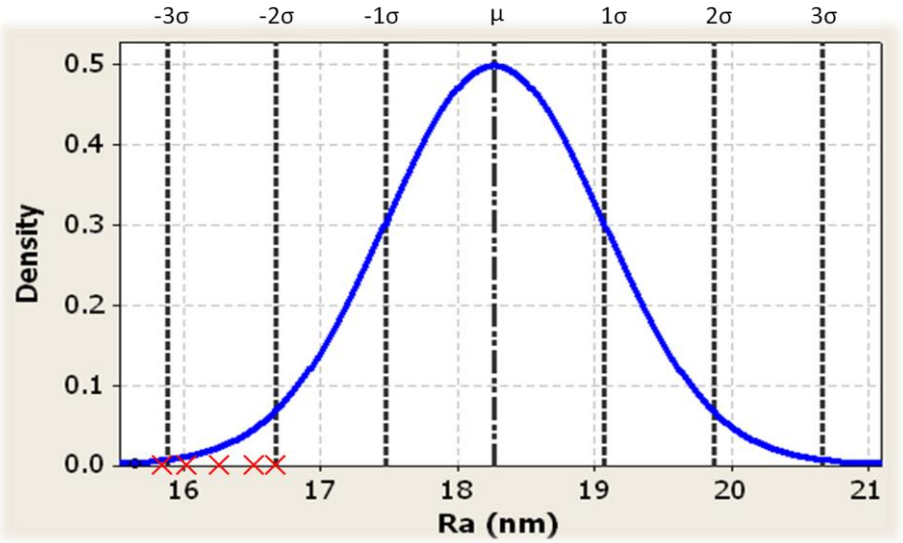

Figure 3-26b: Confirmation run plot considering statistical features

Figure 3-26c shows the actual realizations of R_a from confirmation experiments superposed on the R_a estimates (the mean and the standard deviation) from the regression model shown in Eq. (3-9). Since R^2 is rather low (88.7%), the realizations were outside the 6S range.

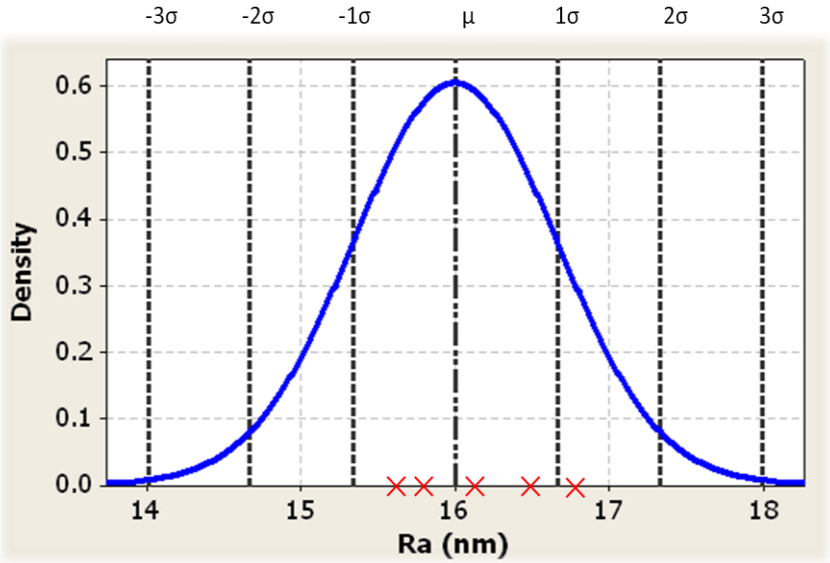

Figure 3-26c: Confirmation run plot considering statistical and energy features

Figure 3-26d shows the actual realizations of R_a from confirmation experiments superposed on the R_a estimates (the mean and the standard deviation) from the regression model shown in Eq. (3-10). Since R^2 is rather low (82.6%), the realizations were outside the 6S range.

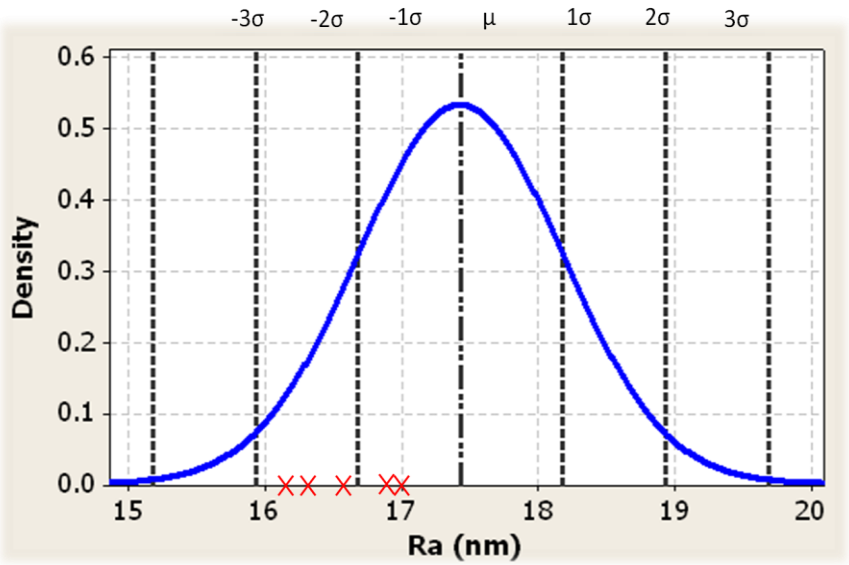

Figure 3-26d: Confirmation run plot considering statistical, energy and RQA features

Figure 3-26e shows the actual realizations of R_a from confirmation experiments superposed on the R_a estimates (the mean and the standard deviation) from the regression model shown in Eq. (3-11). Since R^2 is rather low (36.5%), the realizations were outside the 6S range.

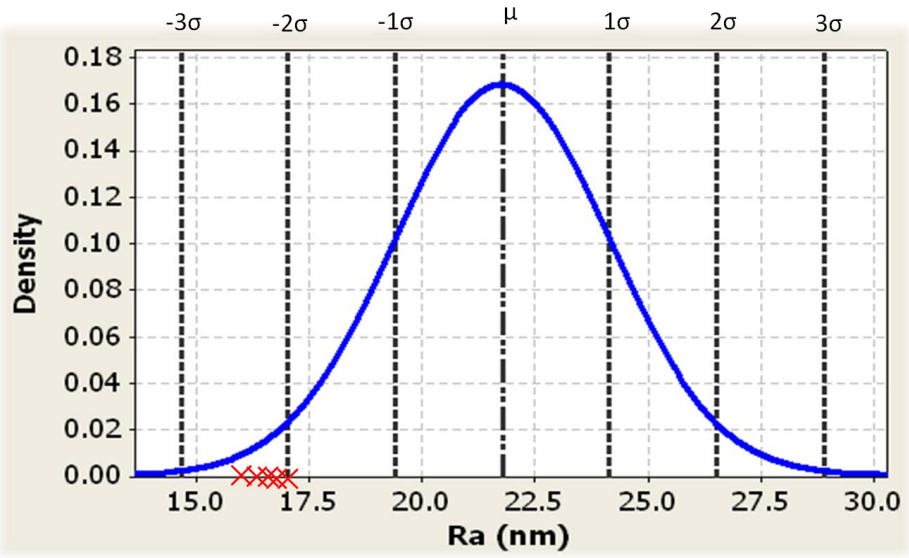

Figure 3-26e: Confirmation run plot considering signal characteristics

Figure 3-26f shows the actual realizations of R_a from confirmation experiments superposed on the R_a estimates (the mean and the standard deviation) from the regression model shown in Eq. (3-12). Since R^2 is rather low (92.0%), the realizations were outside the 6S range.

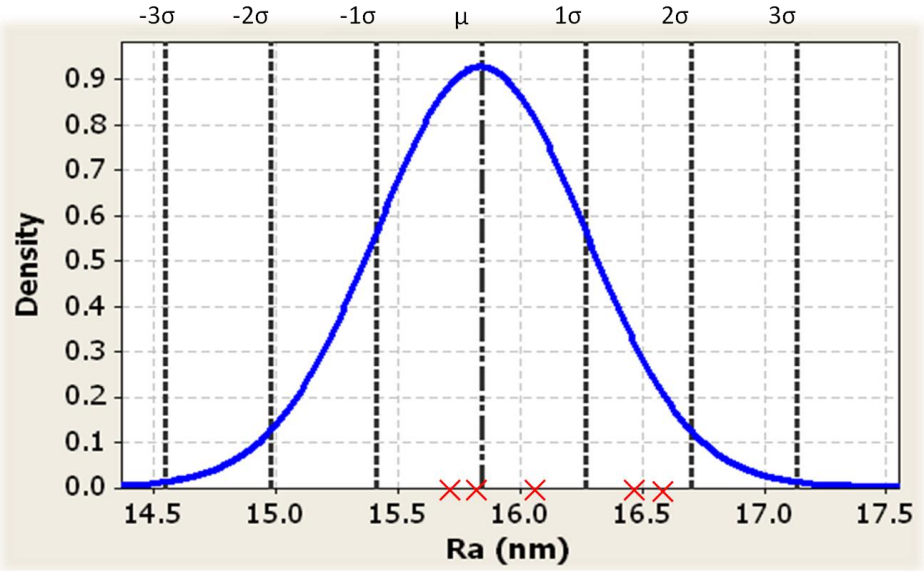

Figure 3-26f: Confirmation run plot considering statistical, energy, RQA & signal characteristics

In summary, Figures 3-26a – 3.26f were plotted taking the predicted R_a as the mean and the model standard deviation and fitting a normal distribution. Distribution limits such as $\mu\pm\sigma$, $\mu\pm2\sigma$, $\mu\pm3\sigma$ were considered for building the normal curve plot. We can observe that the statistical model built using process parameters, statistical features, energy features, RQA features, and signal characteristics having R^2 value of 92.0% can be effectively used to predict R_a as optimized experimental run results lie within the 6σ range. The optimized experimental run results lie within the 6σ range when the R^2 value is high and lie outside the 6σ range when the R^2 value is low. Thus, the process conditions to optimize surface finish (Ra) obtained from the statistical model have been experimentally verified.

CHAPTER IV

COMPUTATIONAL MODELING OF ECMP

4.1 Introduction

The ECMP model considers a steady state of dissolution of copper; species transport inside the electrolyte; ion transport, which includes convection, diffusion and migration; and representation of electrodic reactions using the Butler-Volmer equation. A mixture of 85% phosphoric acid and 15% water was considered the electrolyte. Equation (4-1) and equation (4-2) represent the chemical reactions considered in building the model [24].

$$H_3PO_4 + H_2O \rightleftharpoons H_2PO_4^- + H_3O^+ \quad (4\text{-}1)$$

$$Cu(s) + 6H_2O \rightleftharpoons [Cu(H_2O)_6]^{2+} + 2e^- \quad (4\text{-}2)$$

Water, the copper (II) hexahydrate complex ion, the hydronium ion, and dihydrogen phosphate were the species of interest considered in building the model. The concentration of water [H_2O], copper (II) hexahydrate complex ion [Cu $(H_2O_6)^{2+}$], hydronium ion [H_3O^+], and dihydrogen phosphate [$H_2PO_4^-$] were represented by c1, c2, c3 and c4 respectively.

The electrical conductivity (k) of the solution was estimated by equation (4-3).

$$k = \frac{F^2}{RT}\sum_i z_i^2 D_i c_i \quad (4\text{-}3)$$

The species flux density (N_i) was calculated using equation (4-4).

$$N_i = -z_i u_i F c_i \nabla\Phi - D_i \nabla c_i + c_i v \quad (4\text{-}4)$$

Where $-z_i u_i F c_i \nabla\Phi$ represents the migration flux, $- D_i \nabla c_i$ represents the diffusion flux and $c_i v$ represents the convection flux;

z_i is defined as the number of proton charges on the ion; F is Faraday's constant; R is the reaction rate constant; T is the temperature of the electrolyte; u_i is the mobility of species i and is given by $u_i = D_i/RT$; D_i is the diffusion coefficient for species i in m^2/s; c_i is the concentration of species i in mol/m^3, and v is the velocity vector in m/s.

The current density of the electrolyte is given by equation (4-5).

$$I = F \sum_i z_i N_i \qquad (4\text{-}5)$$

The species conservation equation is given by $\frac{\partial c_i}{\partial t} = -\nabla N_i + R_i$, where R_i is the volumetric production of species i.

Equation (4-5) can be modified by substituting the flux density equation as in equation (4-6).

$$i = -F^2 \nabla \Phi \sum_i z_i^2 u_i c_i - F \sum_i z_i D_i \nabla C_i + FV \sum_i z_i c_i \qquad (4\text{-}6)$$

In order to determine the electrolyte potential Φ, current conservation equation $\nabla . i = 0$ was used to obtain equation (4-7).

$$\nabla . [-\kappa \nabla \Phi - F \sum_i z_i D_i \nabla c_i] = 0 \qquad (4\text{-}7)$$

The Nernst equation (4-8) was used to compute the zero equilibrium potential across the double layer at the surface of each electrode.

$$E = E^0 - \frac{RT}{nF} \log(\frac{c_2}{c_1^6}) \qquad (4\text{-}8)$$

Where E^0 is the standard electrode potential and n is the number of electrons in the reaction.

The relationship that governs the current flow is given by the Butler-Volmer equation, (4-9).

$$i = i_0[\exp(\frac{\alpha_a F}{RT} \eta_s) - \exp(\frac{\alpha_c F}{RT} \eta_s)] \qquad (4\text{-}9)$$

Where η_s is the surface potential and is given by $\eta_s = V_a - E$, α_a is the anodic transfer coefficient, and α_c is the cathodic transfer coefficient [24].

4.2 Implementation of the ECMP model in COMSOL

A COMSOL FEM model was developed for simulating electrochemical removal of copper from the surface in ECMP considering process parameters such as electrolyte concentration and applied voltages. The plate corresponding to the wafer was assumed to be surface coated with a film of copper, which is the prime concern for removal and acts as a working electrode maintained at a constant potential V_a. The potential drops through the film are completely neglected. The other plate acts as a counter electrode and is maintained at a potential V_c. The motion of the polishing pad is rotational and is represented in the x direction, resulting in a linear velocity profile in the vertical direction, u(y) as shown in Figure 4-1[24].

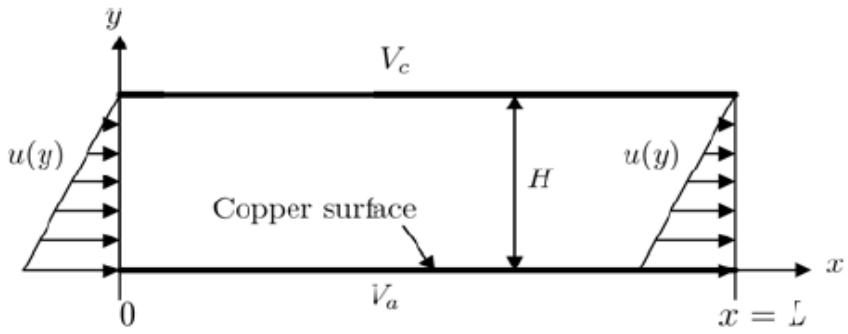

Figure 4-1: Geometry for COMSOL model development [24]

A 2D model was developed as shown in Figure 4-2, representing the flow of a mixture of H_3PO_4 and water between two parallel plates of length 82mm, namely the top and bottom plates, representing the pad and wafer respectively. The plates were separated by 2.92mm.

A COMSOL Multiphysics Tertiary Current Distribution, Nernst-Planc interface along with the electric current interface was used in building the model. The electrolyte was assumed to flow from the left boundary to the right boundary with a constant velocity of 6mm/s as shown in Figure 4-2.

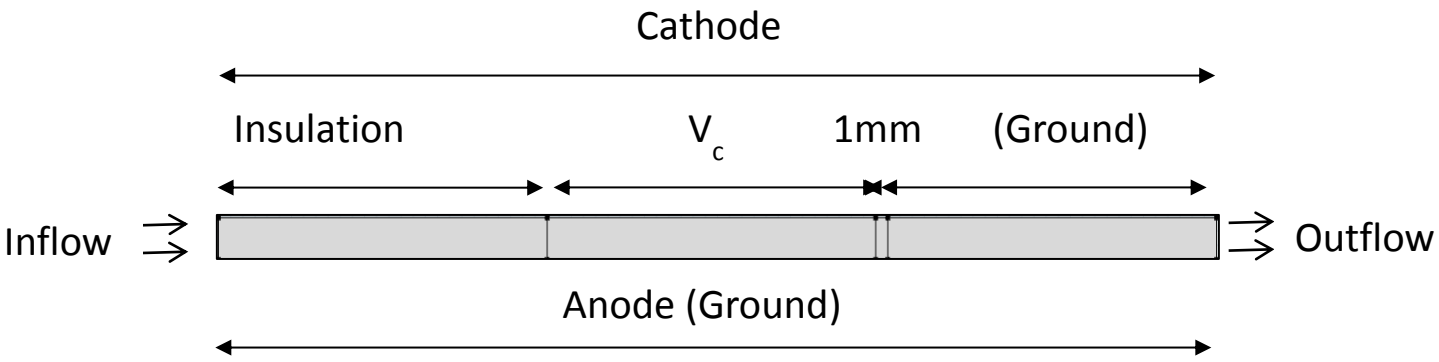

Figure 4-2: 2D COMSOL implementation of ECMP

The geometry of the ECMP model as shown in figure 4-2 was built in COMSOL as a combination of 4 rectangles: (27mm x 2.92mm), (27mm x 2.92mm), (1mm x 2.92mm), and (27mm x 2.92mm) respectively. About 27mm of cathode was insulated; the consecutive 27mm length of cathode was provided with a potential V_c, 1mm of length was insulated, and the final 27mm length of cathode was grounded. The entire length of the anode was also grounded.

Various parameters are described in the global definition column, as shown in Table 4-1.

Table 4-1: Global parameters used in building the ECMP model

Name	Expression	Description
D1	5e-9[m^2/s]	Diffusion coefficient of species 1
D2	1.4e-9[m^2/s]	Diffusion coefficient of species 2
D3	3e-9[m^2/s]	Diffusion coefficient of species 3
D4	0.9e-9[m^2/s]	Diffusion coefficient of species 4
R	8.314[J/(mol*K)]	Rate constant
T	298[K]	Temperature
z1	0	Number of proton charges on species 1
z2	2	Number of proton charges on species 2
z3	1	Number of proton charges on species 3

Name	Expression	Description
z4	-1	Number of proton charges on species 4
F	96500[C/mol]	Faraday's constant
v	6e-3[m/s]	Fluid flow velocity
u1	2.02e-12[(m^2*mol)/(s*J)]	Mobility of species 1
u2	5.65e-13[(m^2*mol)/(s*J)]	Mobility of species 2
u3	1.21e-12[(m^2*mol)/(s*J)]	Mobility of species 3
u4	3.63e-13[(m^2*mol)/(s*J)]	Mobility of species 4
n	2	Number of electrons in the reaction
aa	1.5	Anodic Transfer coefficient
ac	0.5	Cathodic Transfer Coefficient
Va	0[V]	Anodic Potential
Vc	-0.8[V]	Cathodic Potential
i0	10[A/m^2]	Exchange Current Density
ka	7.25e-3[1/s]	Equilibrium constant
E0	0.34[V]	Standard electrode potential of copper
ba	26[mV]	RT/F
tk	1[mol/m^3]	Concentration of species 1 under neutrality condition
kb	1.79e-2[m^3/(mol*s)]	Backward reaction rate
c0	17000[mol/m^3]	Concentration of Phosphoric Acid
c10	8330[mol/m^3]	Concentration of Species 1
kf	1.3e-4[m^3/(mol*s)]	Forward reaction Rate

Variables are defined in the model definition column as shown in Table 4-2.

Table 4-2: Variables used in building the ECMP model

Name	Expression	Description
k	(F^2/(R*T))*(z1^2*D1*c1 + z2^2*D2*c2 + z3^2*D3*c3 + z4^2*D4*c4)	Electrical Conductivity of the solution
E	E0 - (ba/n)*log(c2/tk)	Equilibrium Potential

In the electrolyte field of the Tertiary Current Distribution Nernst-Planc interface, velocity, the diffusion coefficient mobility and the number of proton charges for all four species were specified. And in the initial values field, the initial values of the hydronium ion, the copper-water complex and the dihydrogen phosphate were specified. In the reactions field, the volumetric production of the hydronium ion was specified. The concentration of the hydronium ion, the copper-water complex, and the dihydrogen phosphate were specified at the inlet in the inflow interface. The concentrations of the three species at the anode were specified under the concentration 1 interface, and the concentrations of all three species at the cathode were specified under the concentration 2 interface. Then in the electrolyte – electrode boundary interface, the electric potential V_c to be applied at the cathode was specified. Under the electrode reaction 1 field, the equilibrium potential at the reference temperature was specified. The exchange current density, anodic transfer coefficient, and cathodic transfer coefficient were specified by selecting the Butler-Volmer reaction equation in the electrode kinetics field. The number of participating electrons was specified as n, and the stoichiometric coefficients of species 1 and species 2 were mentioned in the stoichiometric coefficients field.

The electrical conductivity of the electrolyte was specified in the electric current interface under current conservation. The current density in both x and y directions was specified under the external current density interface. The cathodic potential V_c was specified using the electrical potential interface. The segment to the right of the segmented electrode along with the anode boundary was

grounded and was specified under the ground interface. A user-controlled mesh and steady state study was chosen for the model.

4.3 Results and Discussions

4.3.1 Conformational results

A cathodic potential of 0.8V was applied to the cathode, and the variation of potential from cathode to anode is shown in Figure 4-3.We observe that the electric potential is maximum at the cathode and decreases when it moves towards the anode and finally becomes 0 at the anode.

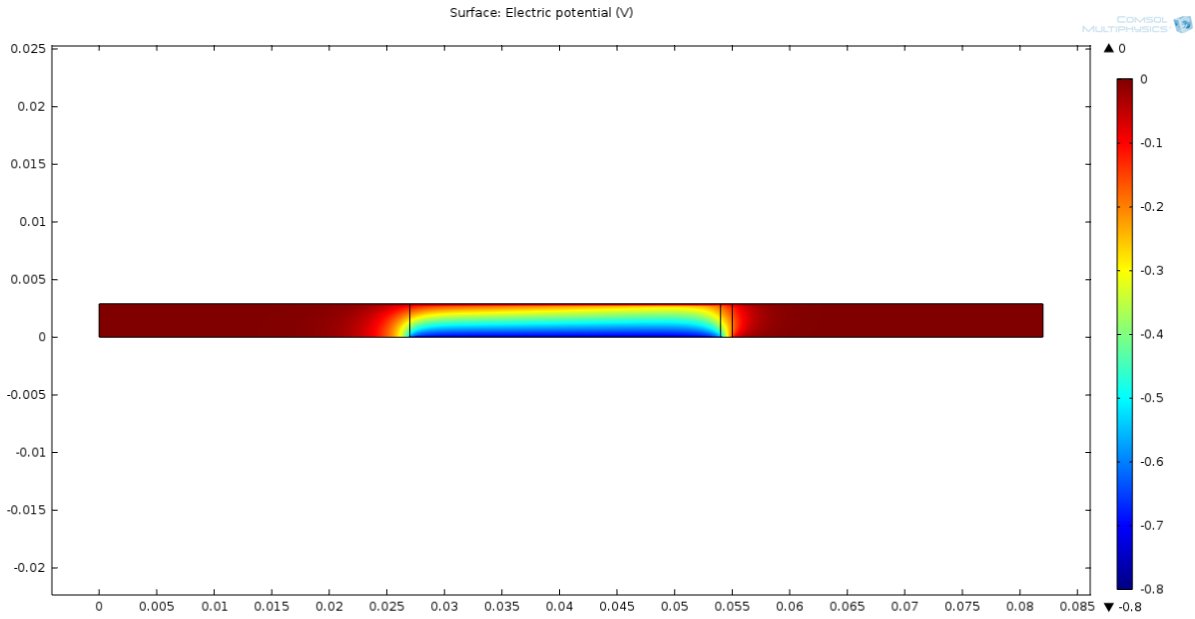

Figure 4-3: Distribution of Electric Potential

The presence of the hydronium ion in equilibrium concentrations is prominent in most of the electrolyte except near the electrodes. It is clearly visible that at the anode, water depletion results in hydronium ion depletion and at the anode the ion gives up the positive charge to the electrode. This process can be clearly seen in the concentration variation of the hydronium ion from cathode to anode as shown in Figure 4-4[24].

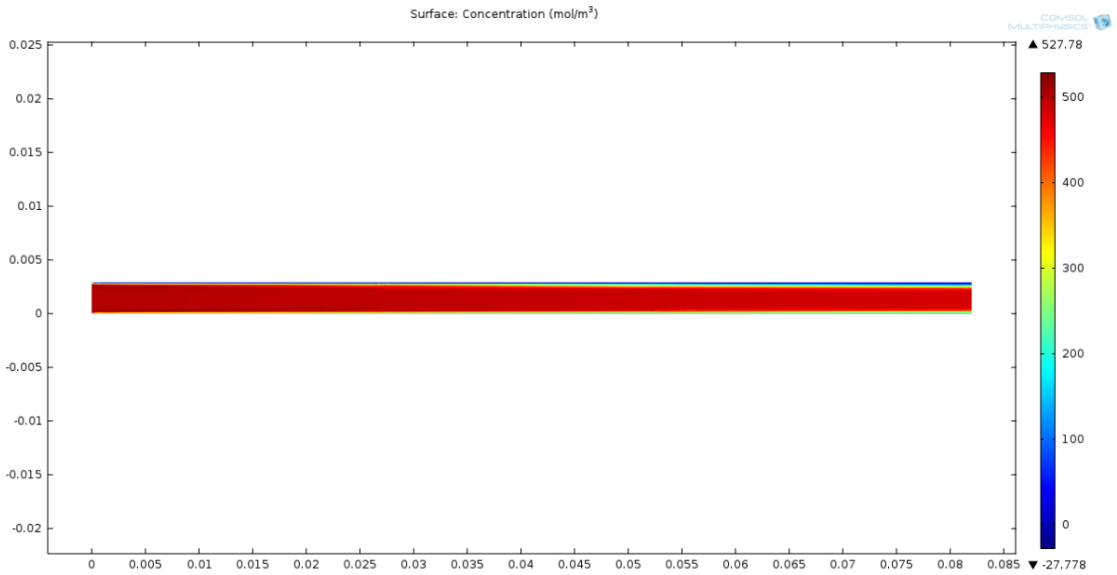

Figure 4-4: Distribution of Hydronium ion concentration throughout the electrolyte

The concentrations of the hydronium ion and dihydrogen phosphate are maximum near the cathode, remain constant for a while, and decrease when nearing the anode as the hydronium ion combines with water to form copper complex near the anode, as shown in Figure 4-5.

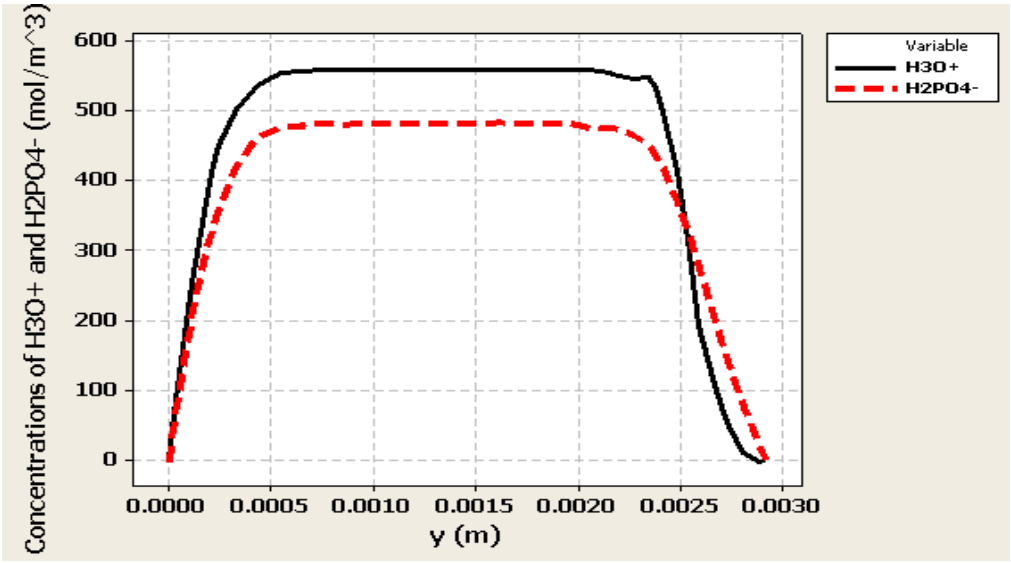

Figure 4-5: Distribution of hydronium ion and dihydrogen phosphate from cathode to anode

The concentration of c2 is zero at the cathode, as there is no complex formation at the cathode and increases near the anode as copper combines with water and the hydronium ion near the anode. The concentration of copper complex increases and reaches a maximum value and then the concentration of c2 decreases because of the depletion of water and hydronium ions.

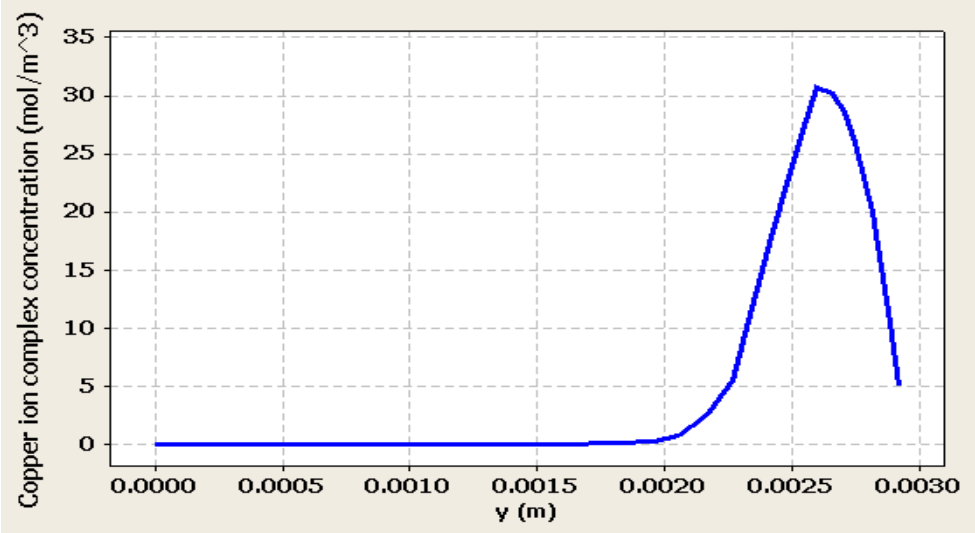

Figure 4-6: Distribution of copper ion complex from cathode to anode

The copper polishing rate in Angstrom/min at the anode was calculated from the concentration gradient of c2 as shown in Figure 4-7.

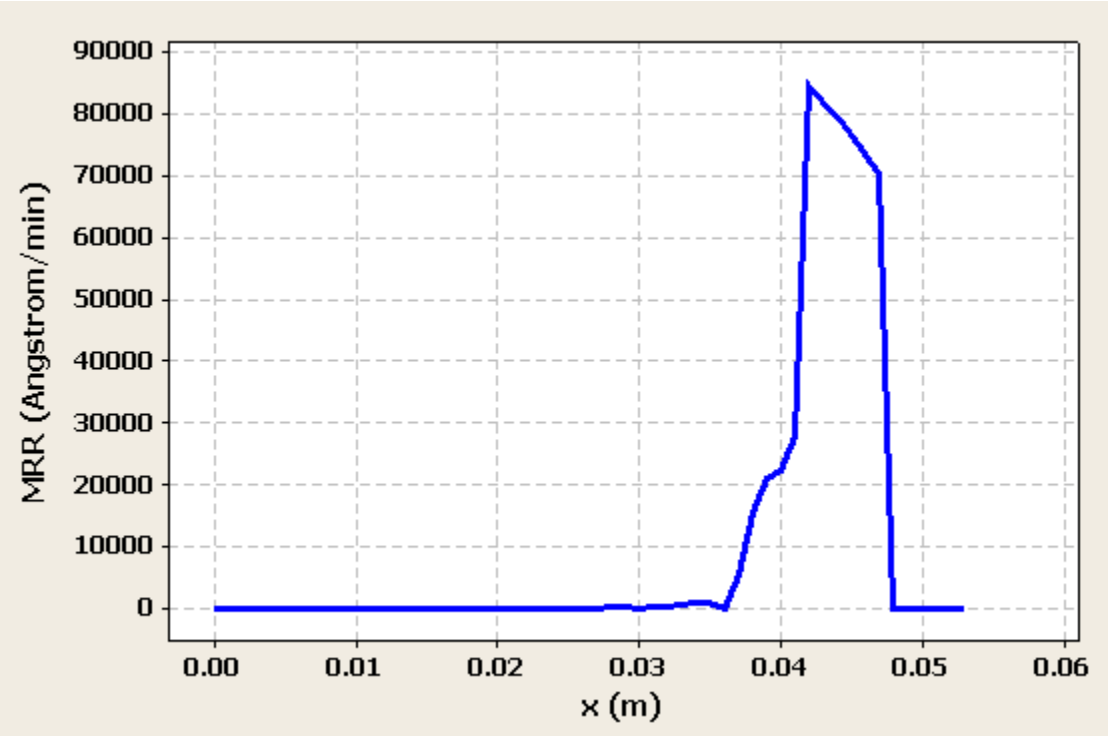

Figure 4-7: Copper polish rate in nm/min at the anode

It was observed that the polishing rate decreased in the direction of flow as less water was available to create the copper complex. Finally it becomes zero at the end of the anode due to depletion of water as well as hydronium ion near the anode [24].

4.3.2 Voltage variation study

The cathodic potential (V_c) was increased from 1 to 5V and the change in MRR and the I-V characteristics were studied. The MRR obtained by performing experiments are shown in Figure 4-8. The simulated MRR is shown in Figure 4-9.The experimental and the simulated IV characteristics are shown in Figure 4-10 and Figure 4-11 respectively.

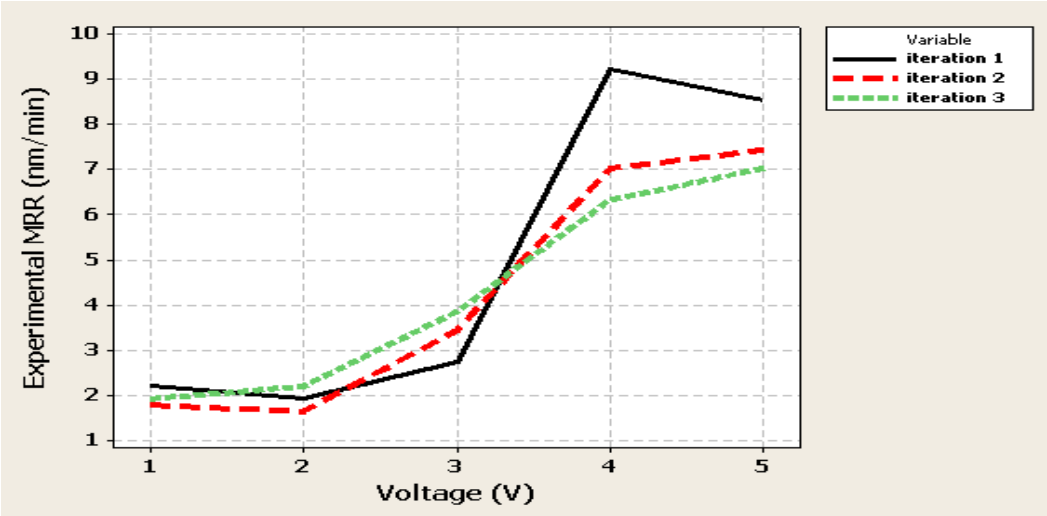

Figure 4-8: Experimental MRR vs applied voltage

From Figure 4-8,we can observe that as the voltage is gradually incresed from 1 to 5 V, the MRR also increases. And a similar trend was observed for all the three iterations.The MRR was found to decrease at 2V first 2 iterations but it was observed to increase with increase in voltage for the iteration 3. So, we can conclude that the MRR increase with increase in voltage.

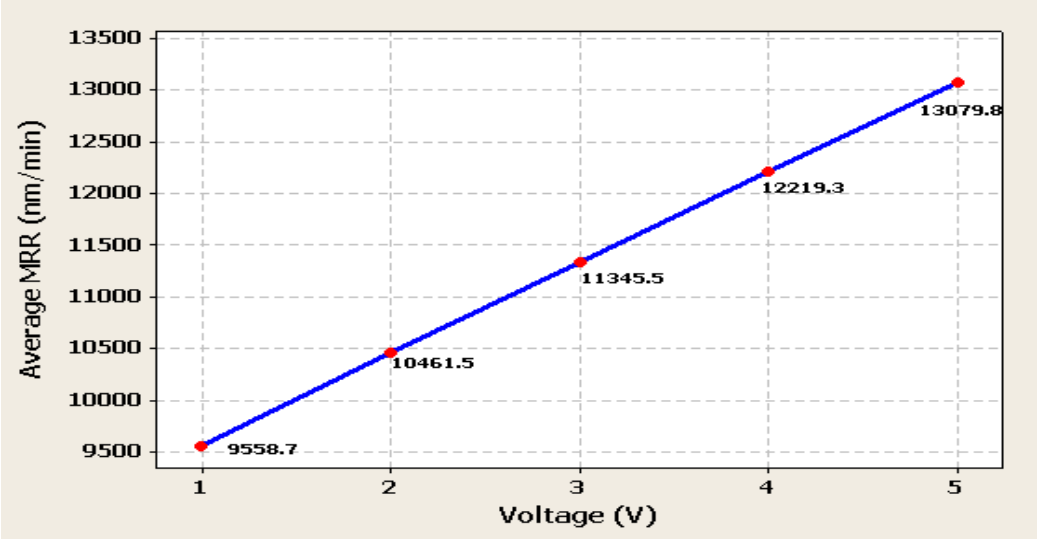

Figure 4-9: Simulated Average MRR vs. applied voltage

The average MRR was observed to increase with increase in cathodic potential as shown in Figure 4-9.Eventhough the simulated average MRR values were different from those obtained from the experiment but followed a similar trend as that of the Experimental MRR.

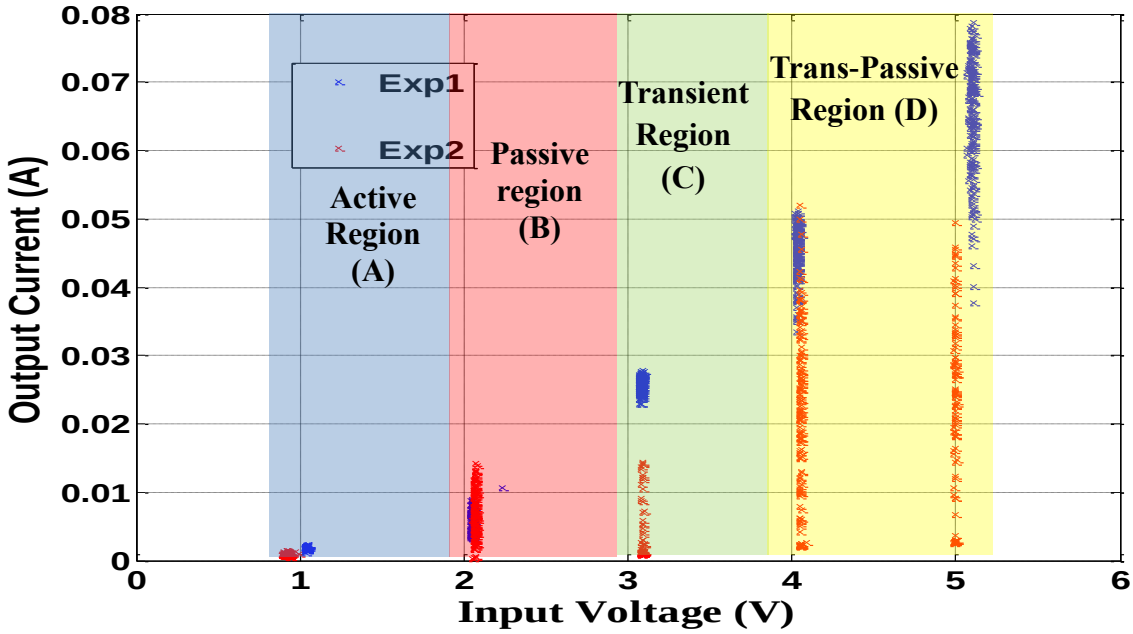

Figure 4-10: Experimental I-V characteristics curve

Figure 4-10 shows the I-V characteristics obtained from the experiment. Various electrochemical phases have been identified and the average current was found to increase with increase in voltage from 1 to 5V.

We observe from the simulated IV characteristics that the average current density increases with increase in average electrolyte potential .The increasing trend observed in the I-V characteristics obtained from the experiment is similar to that of the simulated I-V characteristics as shown in Figure 4-11.

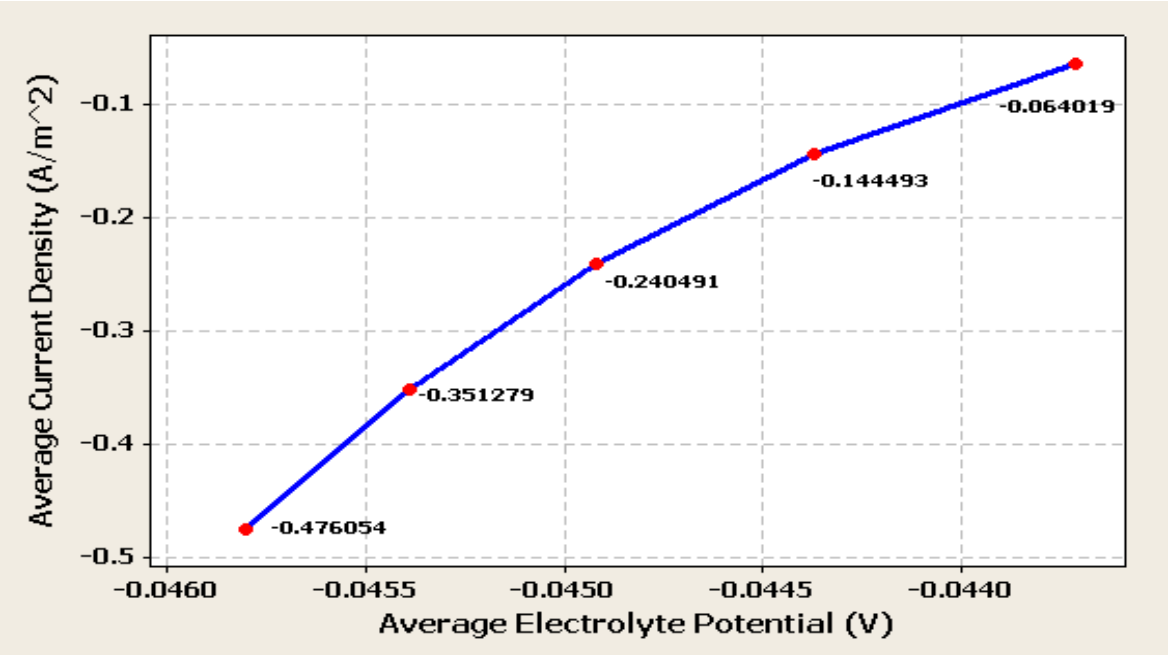

Fig 4-11: Simulated I-V characteristics

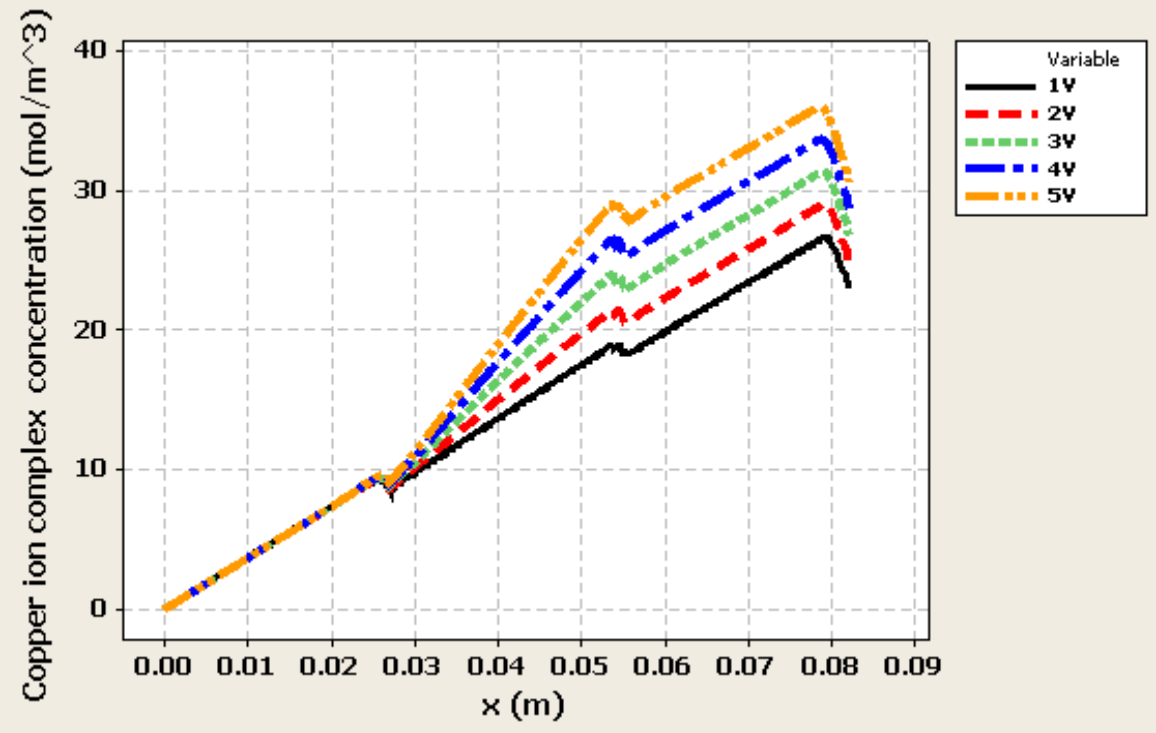

Figure 4-12: Copper ion complex concentration variation with voltage

The concentration of copper complex at the anode was found to increase with the increase in cathodic potential from 1to 5V as shown in Figure 4-12. The concentration change pattern was observed to follow a trend similar to the increase in cathodic potential. We can see from Figure 4-12 that the average copper complex concentration increased with the increase in applied voltage.

Table 4-3: % difference of Copper complex concentration with variation in voltage

Cathodic Potential (V)	% difference of Copper complex concentration
1	36.63
2	25.02
3	15.33
4	7.09
5	0

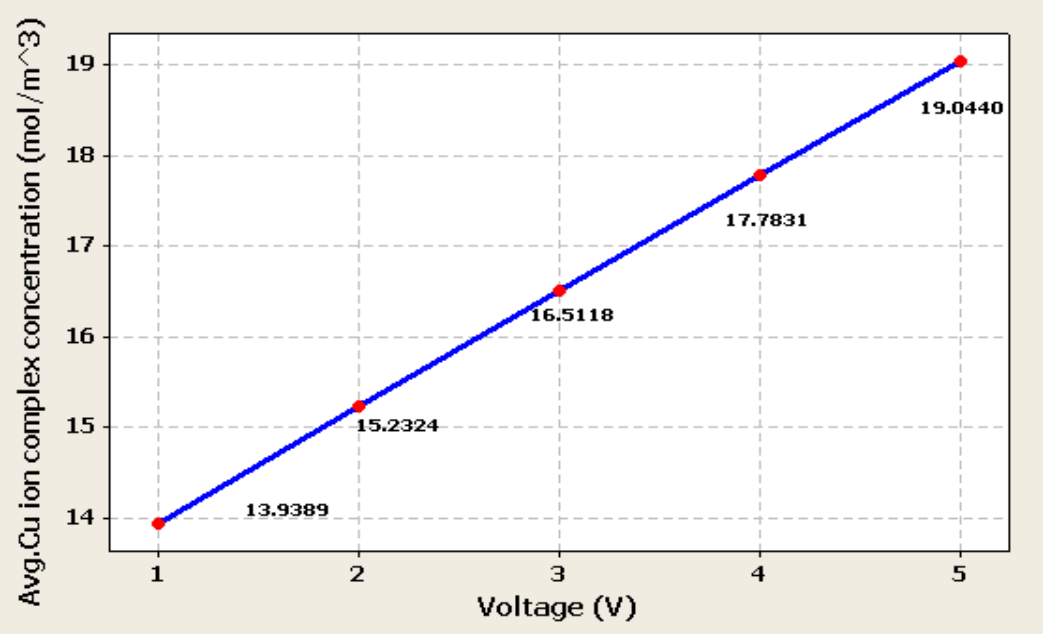

Figure 4-13: Change in average copper complex concentration with variation in voltage

From Figure 4-13 we observe that the average copper ion complex concentration increases with increase in cathodic potential and it was maximum at 5V.We can observe from the Table 4-3 that the percentage difference between the average copper ion complex concentration at various cathodic potentials is minimum at 4V when compared with the average copper ion complex concentration at 5V.

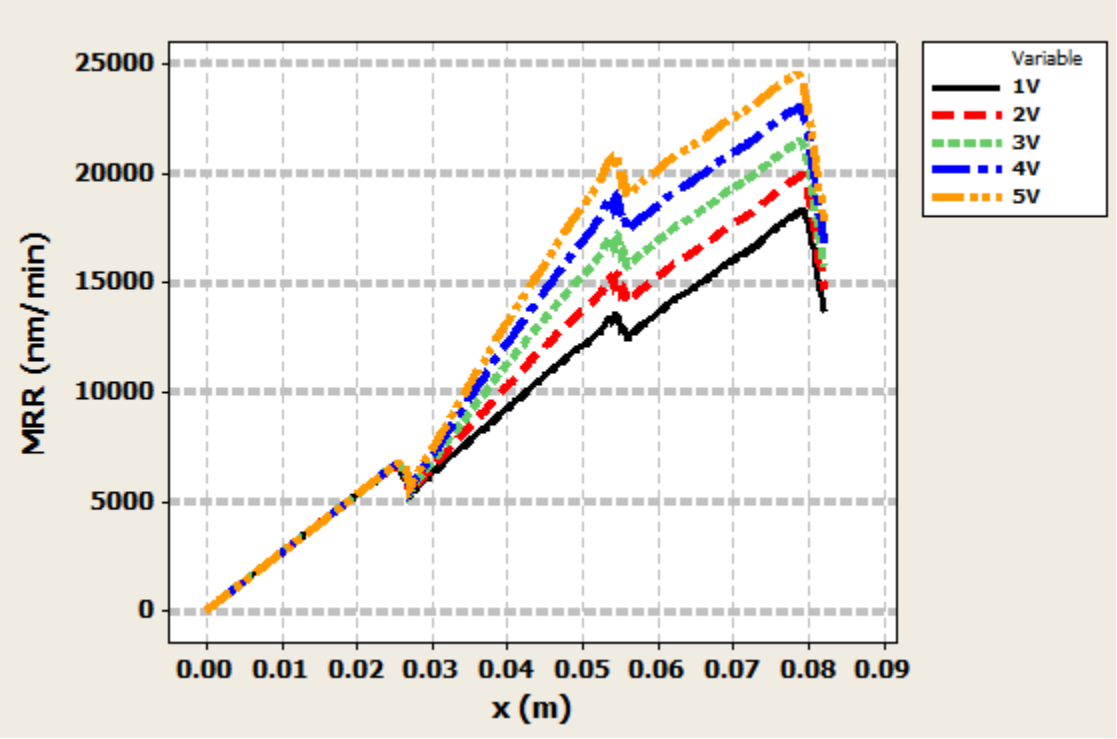

Figure 4-14: MRR concentration variation with voltage

The copper removal rate at the anode increased with the increase in applied cathodic potential as shown in Figure 4-14. The MRR change pattern was observed to follow a similar trend. We can observe from Figure 4-14 that the Copper removal rate increases with an increase in applied cathodic potential.

Table 4-4: % difference of MRR with variation in voltage

Cathodic Potential(V)	% difference of MRR
1	3.68
2	2.50
3	1.53
4	0.70
5	0

From Table 4-4, we can observe that the percentage difference between the MRR at various cathodic potentials is minimum at 4V when compared with the observed maximum MRR at 5V.And the % difference in MRR decreases with increase in cathodic potential.

4.3.3 Speed variation study

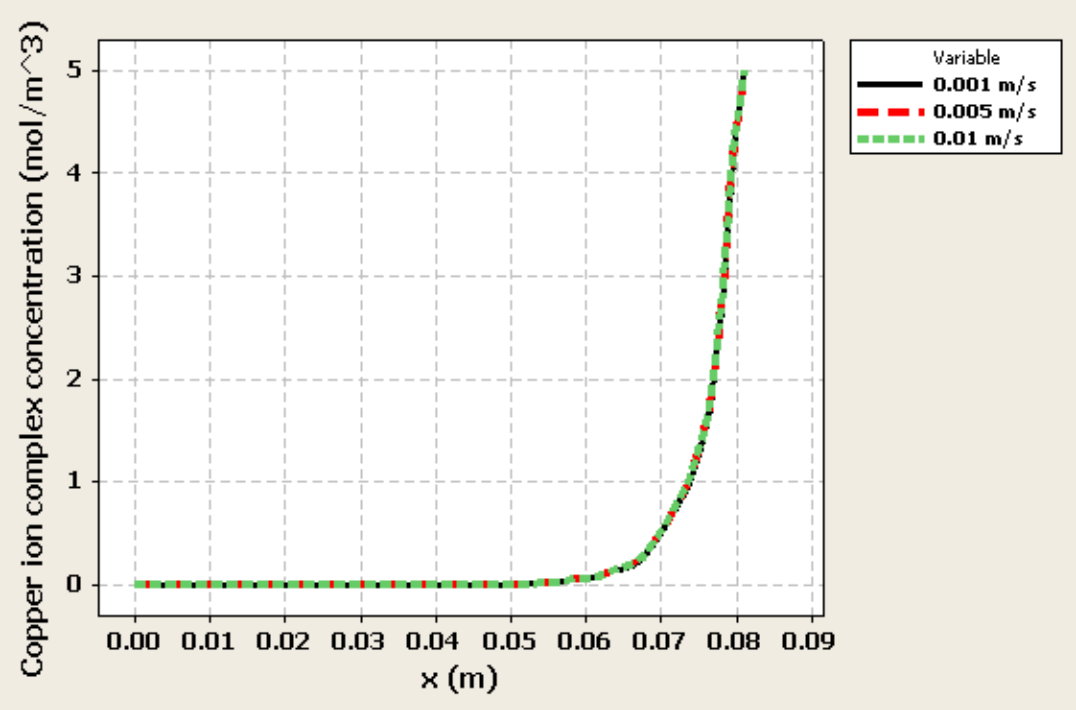

Figure 4-15: Copper ion complex concentration variation with electrolyte flow velocity

The concentration of copper complex at the anode increased with the increase in electrolyte flow velocity as shown in Figure 4-15. The difference in concentration change was observed to be very small with increase in electrolyte flow velocity.

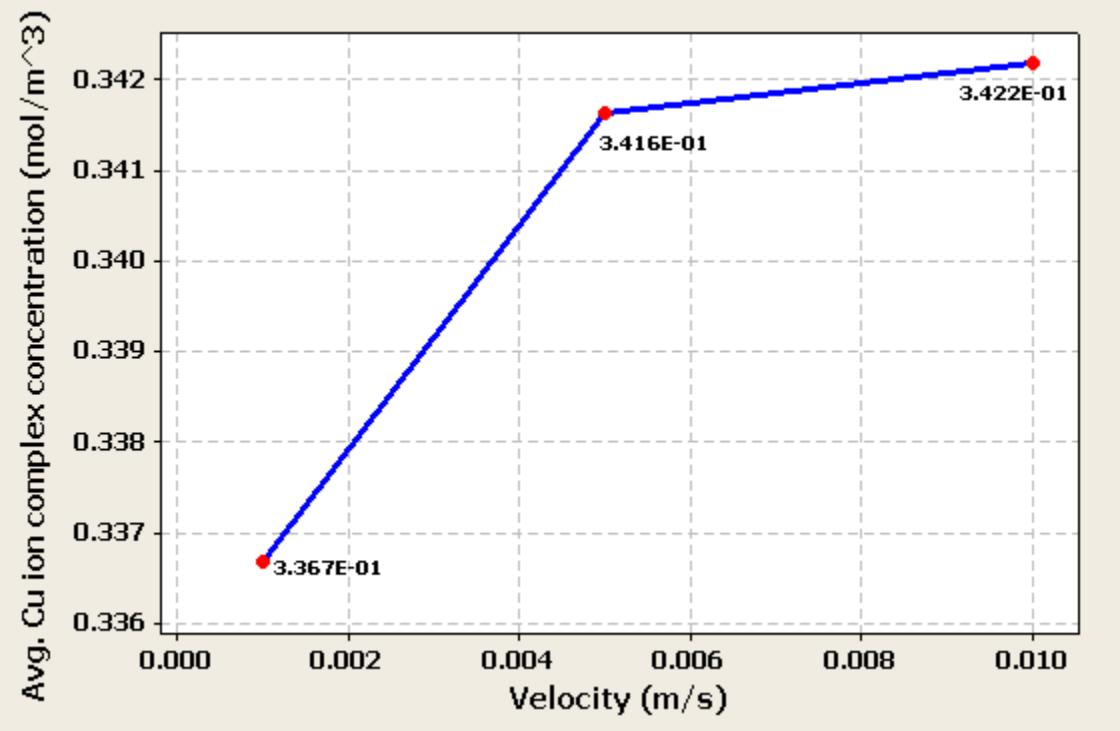

Figure 4-16: Change in average copper complex with variation in velocity

We can observe from Figure 4-16 that the average copper complex concentration increases with the increase in electrolyte flow velocity. The copper complex concentration at a velocity of 0.001 m /s was 1.64% greater than the concentration of copper complex at a velocity of 0.01 m/s, and the copper complex concentration at a velocity of 0.005 m/s was 0.16% greater than that at velocity of 0.01m/s.

The MRR also increased with the increase in electrolyte flow velocity, as shown in Figure 4-18. The MRR difference was observed to be very minimum with increase in velocity. The trend is also prominent from the experiment as shown in Figure 4-17 that the MRR increases with increase in electrolyte flow velocity.

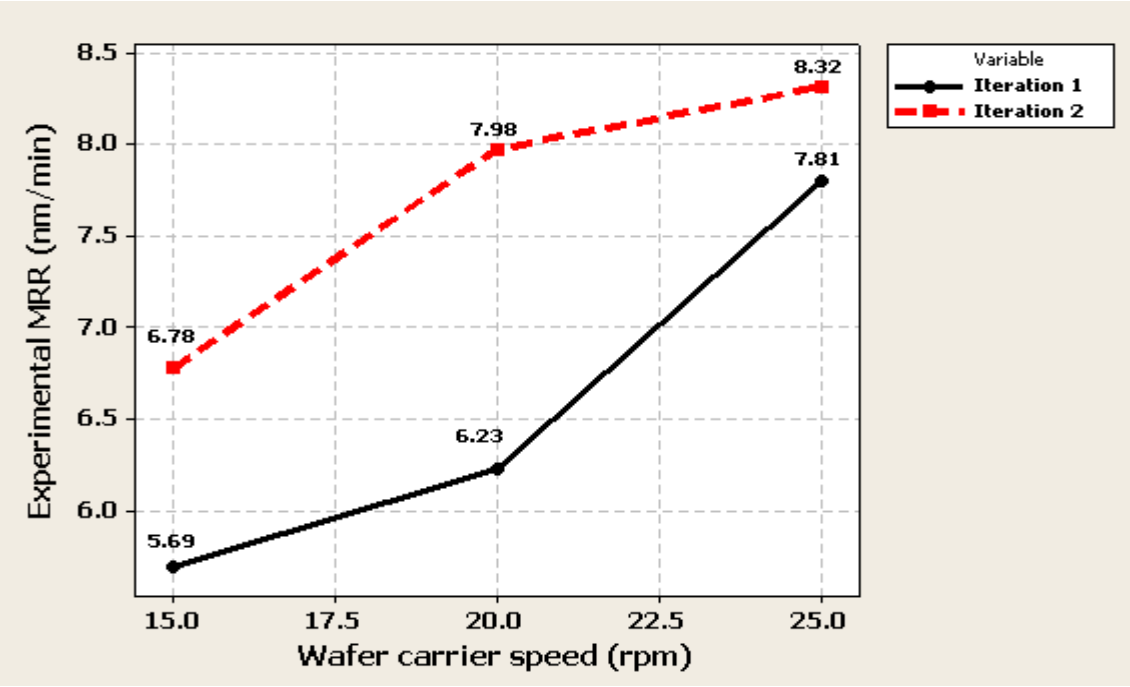

Figure 4-17: Change in Experimental MRR with variation in velocity

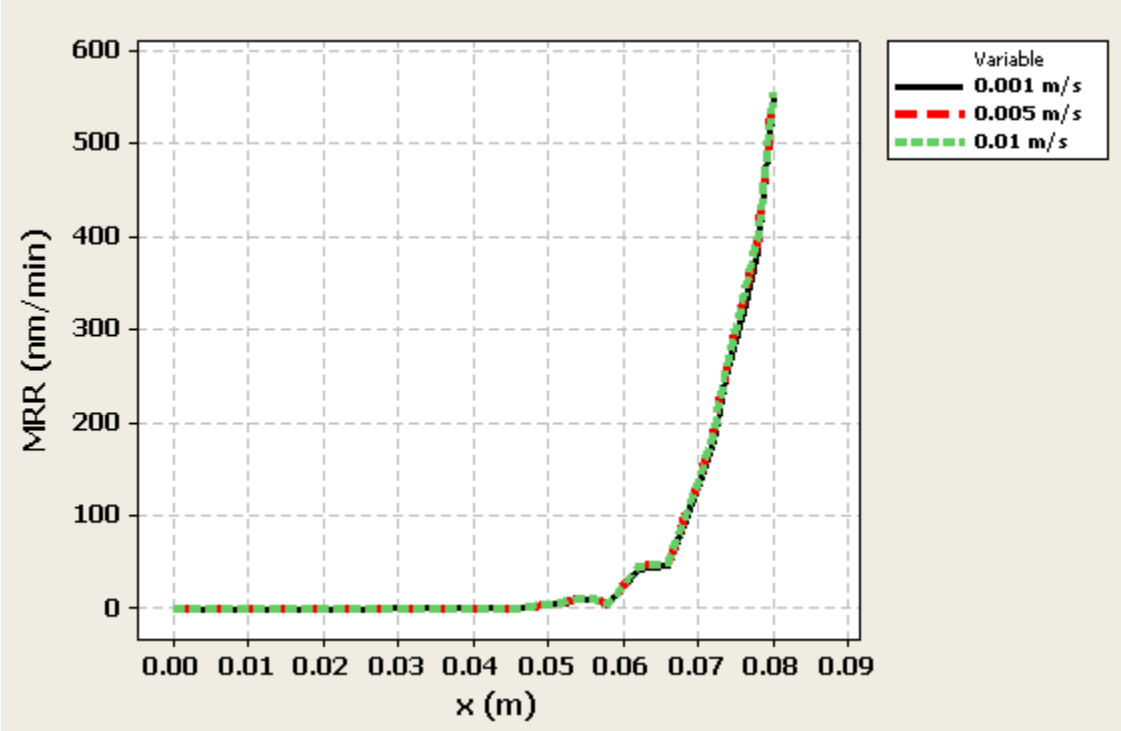

Figure 4-18: Change in MRR with variation in velocity

We can observe from Figure 4-19 that the average MRR increased with the increase in electrolyte flow velocity. The MRR at the anode at a velocity of 0.001 m /s was 3.48% greater than the MRR at 0.01m/s, and the MRR at a velocity of 0.005 m/s was 0.34% greater than the MRR at a velocity of 0.01m/s.

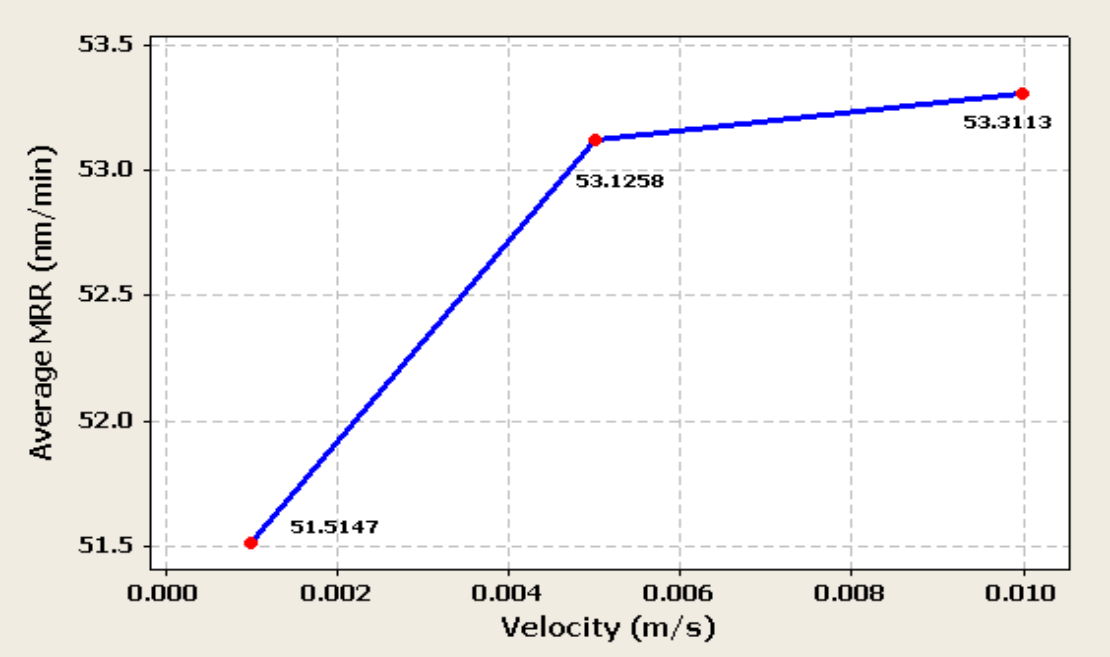

Figure 4-19: Change in average MRR with variation in velocity

The electrolyte potential also increased with the increase in wafer carrier speed, as shown in Figure 4-20. The electrolyte potential difference at various velocities was found to be minimal. It is very clear from Figure 4-20 that the electrolyte potential values at various velocities overlap each other.

We can observe from the Figure 4-21 that the average electrolyte potential increased with increase in velocity. Also, the electrolyte potential at the anode when the velocity is 0.001m/s was 0.054% greater than the electrolyte potential at 0.01 m/s, and the copper complex concentration at a velocity of 0.005 m/s was 0.0053% greater than the electrolyte potential at a velocity of 0.01m/s.

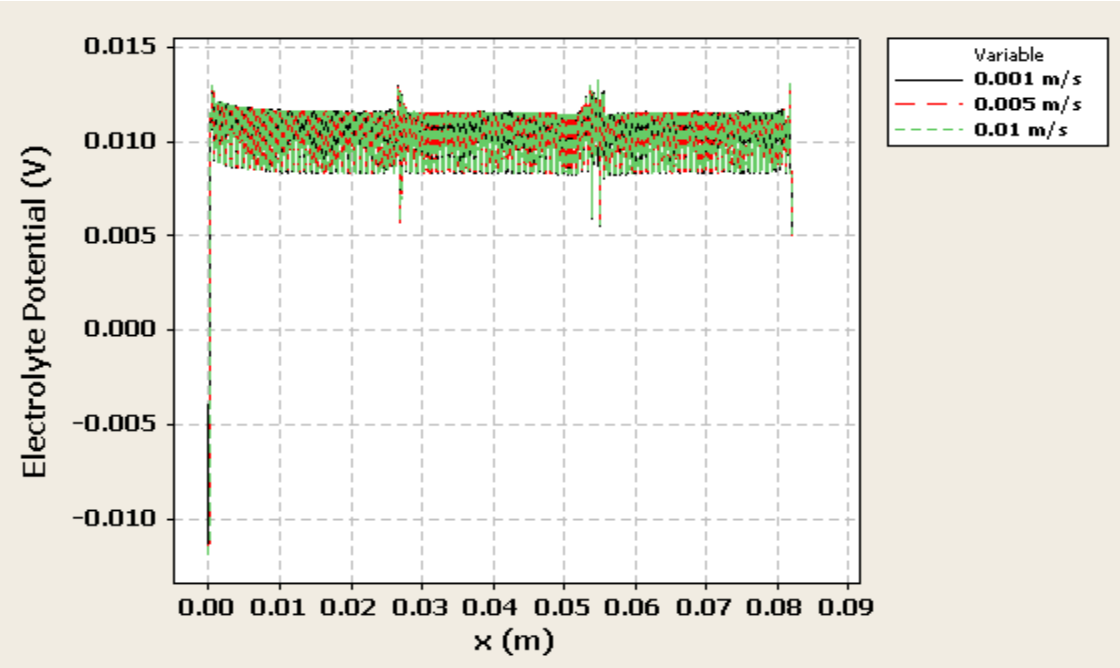

Figure 4-20: Change in electrolyte potential with variation in velocity

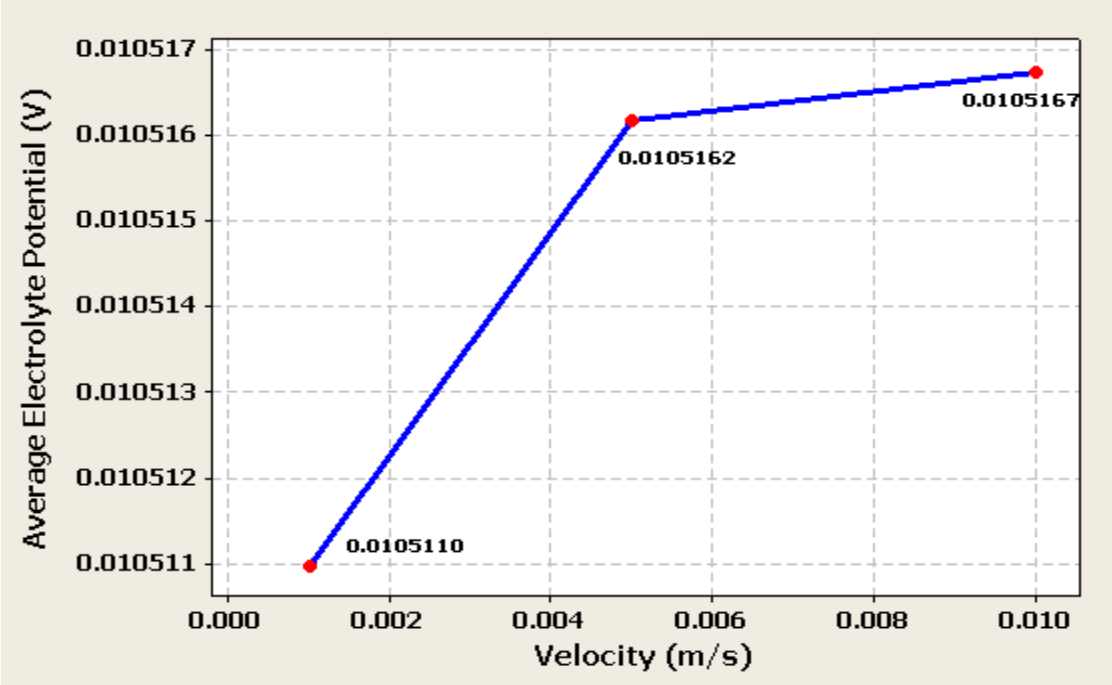

Figure 4-21: Change in average electrolyte potential with variation in velocity

4.3.4 Anode to cathode distance variation study

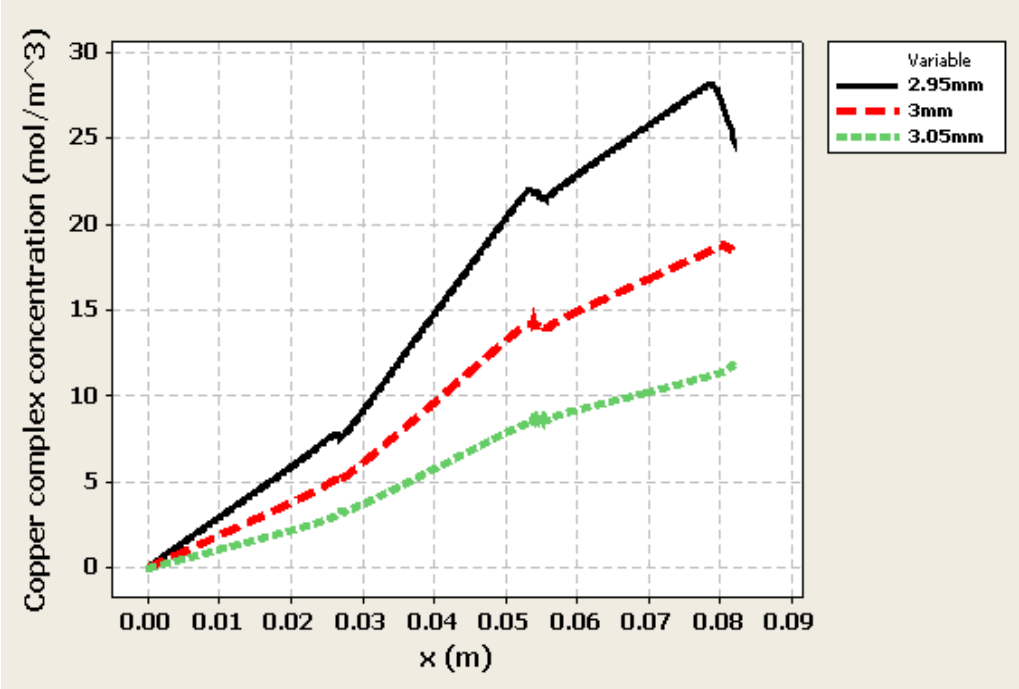

Figure 4-22: Change in concentration with variation in cathode to anode distance

The concentration of copper complex at the anode decreased with the increase in the distance between anode and cathode as shown in Figure 4-22. The concentration of copper complex at the anode decreases with increase in anode to cathode distance as the electric field decreases, due to which the current decreases thereby, decreasing the copper complex concentration.

We see from Figure 4-23 that the average copper complex concentration decreased with the increase in anode to cathode distance. The copper complex concentration when the anode to cathode distance was 3mm was 5.23% greater than the concentration of copper complex when anode to cathode distance was 2.95mm, and the copper complex concentration when the anode to cathode distance was 3.05mm was 15.21% greater than the concentration when the anode to cathode distance was 2.95mm.

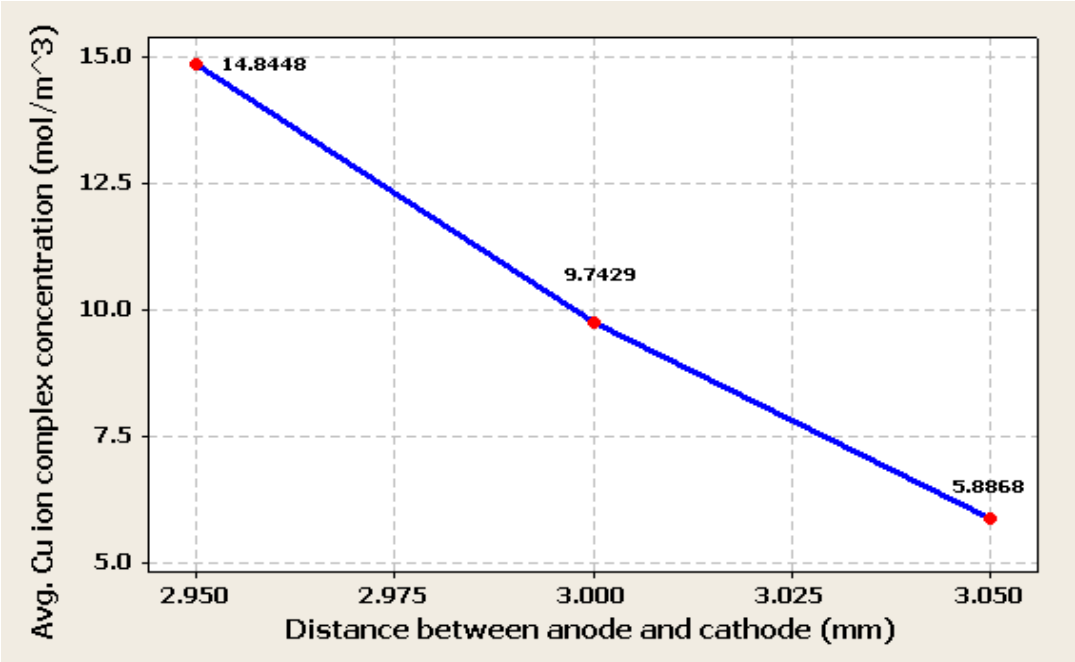

Figure 4-23: Change in average concentration with variation in cathode to anode distance

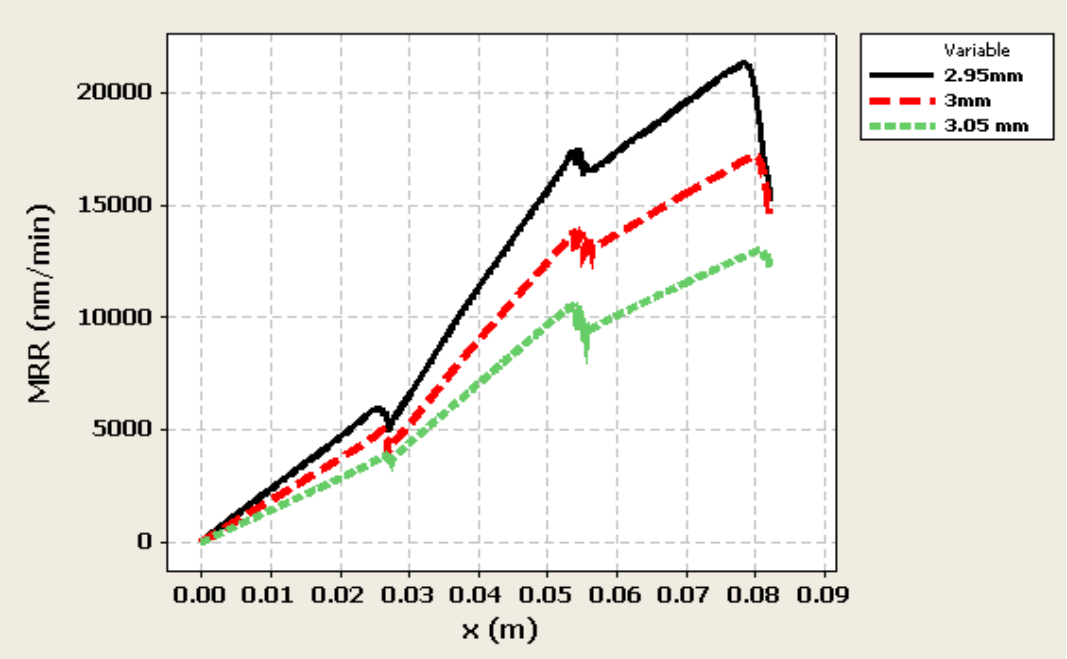

Figure 4-24: Change in MRR with variation in cathode to anode distance

The MRR decreased with the increase in anode to cathode distance, as shown in Figure 4-24.

And the MRR pattern was observed to follow a similar trend for all the cases.

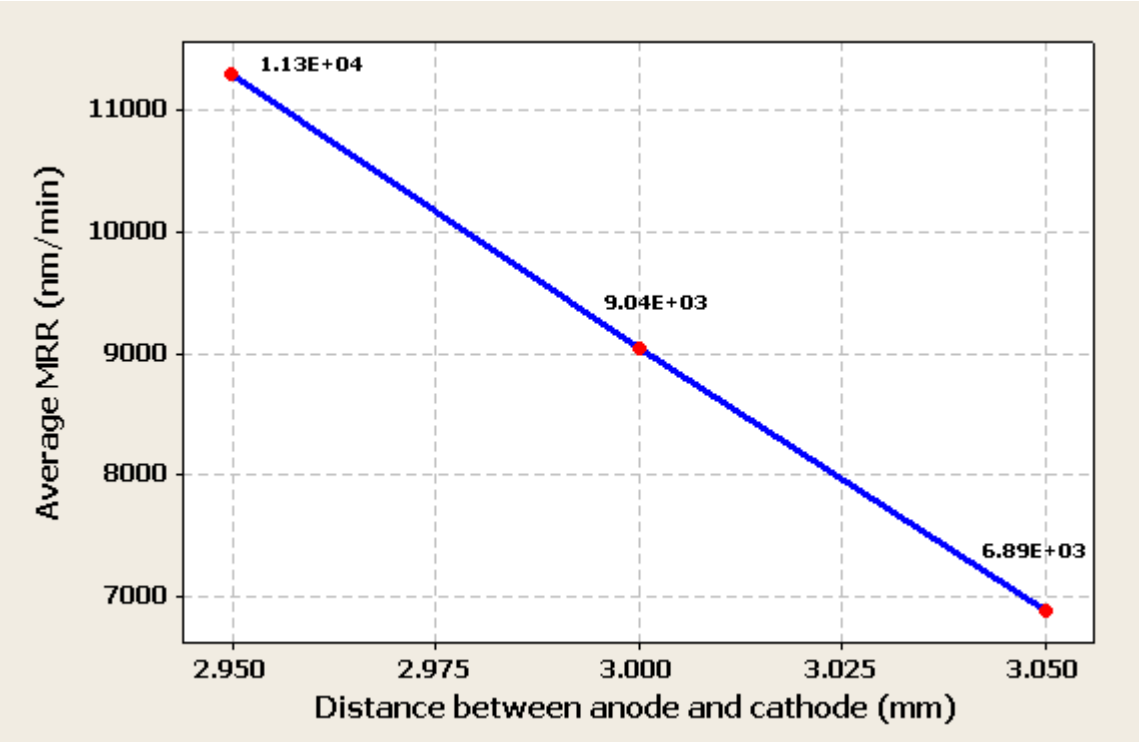

Figure 4-25: Change in average MRR with variation in cathode to anode distance

We can observe from Figure 4-25, that the average copper complex concentration decreased with increase in anode to cathode distance. The total electric field decreases, when the anode to cathode distance is increased, thereby decreasing the current and due to which the MRR also decreases. When the anode to cathode distance was 3mm, the MRR was 2.49% greater than the concentration of copper complex when the anode to cathode distance was 2.95mm, and when the anode to cathode distance was 3.05mm, the MRR was 6.40% greater than when the anode to cathode distance was 2.95mm.

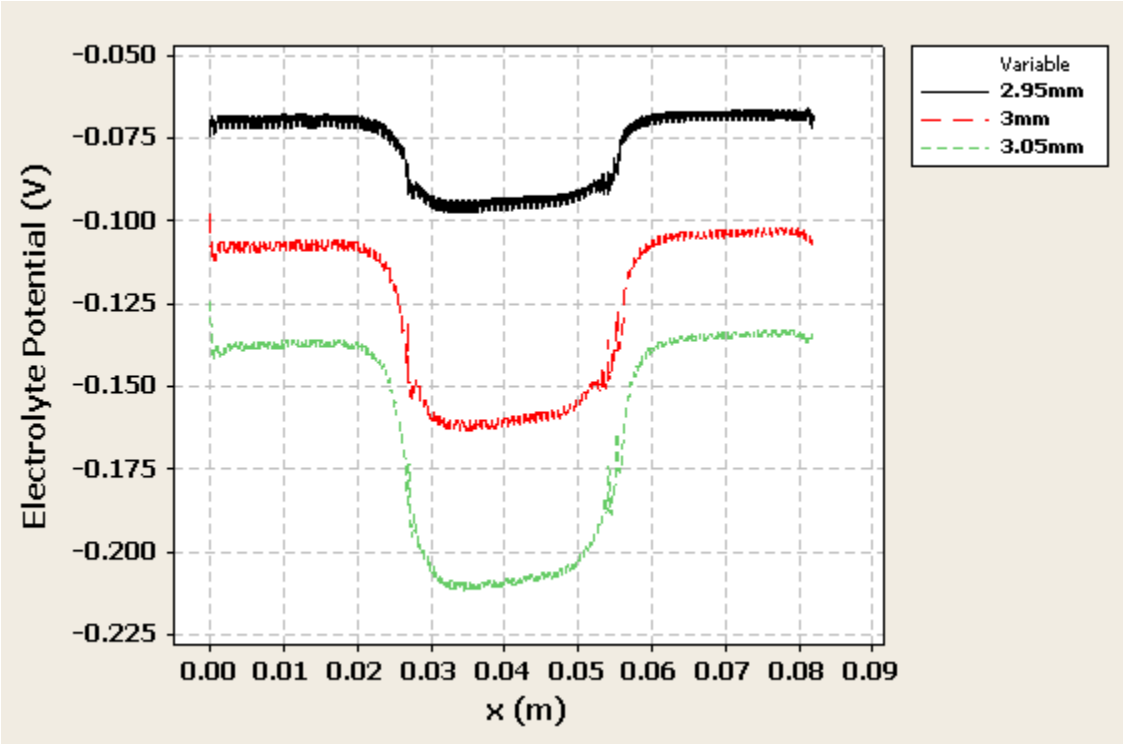

Figure 4-26: Change in electrolyte potential with variation in cathode to anode distance

The electrolyte potential decreased with the increase in anode to cathode distance, as shown in Figure 4-26. We can observe that the difference between the electrolyte potential increases with the increase in anode to cathode distance due to decrease in current caused by the decrease in total electric field. We can observe from Figure 4-27, that the average electrolyte potential decreased with the increase in anode to cathode distance.

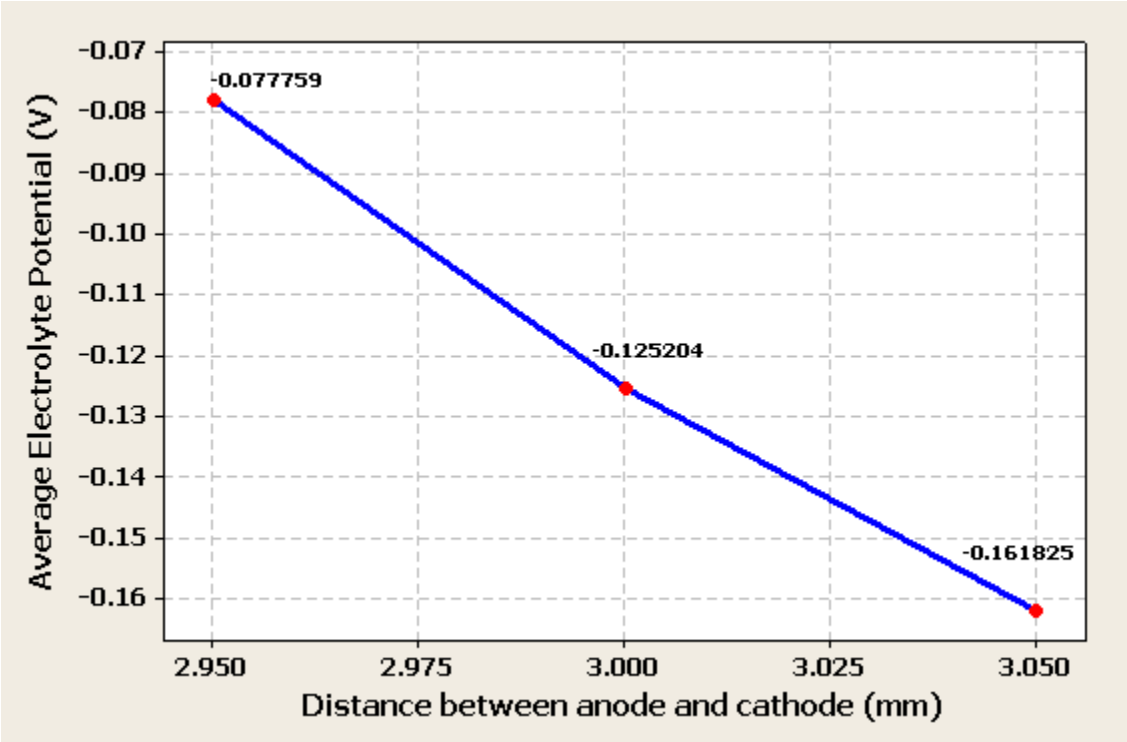

Figure 4-27: Change in average electrolyte potential with variation in cathode to anode distance

CHAPTER V

CONCLUSIONS AND FUTURE WORK

Major parameters affecting the MRR and surface roughness were identified and used to build statistical models. A full factorial design of experiments was conducted to collect data for building the statistical models. Just the process parameters are not sufficient to predict MRR and surface roughness; statistical, time-frequency, and non-linear features of the current must be considered for predicting MRR and surface roughness. The process current signal was used in tracking changes in the Material Removal Rate (MRR) with respect to the applied anodic potential. Various electrochemical phases were mapped by analyzing the current and voltage signal characteristics. The statistical regression models predicting MRR and R_a with statistical, energy, RQA features and signal characteristics gave R^2: 91.8% and 92% respectively.

Low pad pressure angle, 4.5V, and 6.5pH were found to be the optimum conditions for carrying out ECMP of copper wafers. The best regions to work with in Cu ECMP were found to be the transient/trans-passive regions (4–5 V) where the best R_a value and high MRR can be achieved. From the FFT curves of process current we can track the pad speed (frequency peak *0.339Hz* band) and wafer carrier speed (frequency peak *5.449Hz* band*)*, and the amplitude of these peaks can exactly track the variation in the MRR at different anodic voltages.

With further work we can exactly model an equation which can depict the dynamic change in the MRR, which can serve as a very important contribution to the end point detection of the ECMP process. By performing an FFT analysis for 256 peaks above the threshold value, we were able to map out the electrochemical phase transition of the process under different voltage conditions. A mathematical model depicting the ECMP was identified and implemented in COMSOL to study the

change in copper complex concentration, MRR, and electrolyte potential with the variation of applied cathodic voltage, wafer carrier speed and anode to cathode distance. It was observed that the simulated results followed a pattern similar to that of the experimental results.

For future work, concentrations of other components of the slurry can be considered in simulating MRR under different boundary conditions using COMSOL. A force sensor can be used to calculate the exact down pressure and include it as a process parameter in building a statistical model. The features extracted from the signals can be used to detect defects.

REFERENCES

[1] A. Tripathi, I.I. Suni, Y. Li, F. Doniat, and J. McAndrew, “Cu Electrochemical Mechanical Planarization Surface Quality”, *Journal of the Electrochemical Society,* 156 (2009), H555-H60.

[2] M. Mellier, T. Berger, R. Duru, M. Zaleski, M. Luche, M. Rivoire, C. Goldberg, G. Wyborn, K.-L. Chang, and Y. Wang, "Full copper electrochemical mechanical planarization (Ecmp) as a technology enabler for the 45 and 32nm nodes," in *International Interconnect Technology Conference, IEEE 2007*, 2007, pp. 70-72.

[3] N. Kulyk, C.Y. An, J.H. Oh, S.M. Cho, C. Ryu, Y.K. Ko, and C.H. Chung, 'Study on Electrochemical Mechanical Polishing Process of Copper Circuit on Pcb', *Korean Journal of Chemical Engineering,* 27 (2010), 310-14.

[4] Y.J. Oh, G.S. Park, and C.H. Chung, 'Planarization of Copper Layer for Damascene Interconnection by Electrochemical Polishing in Alkali-Based Solution', *Journal of the Electrochemical Society,* 153 (2006), G617-G21.

[5] F.Q. Liu, T. Du, A. Duboust, S. Tsai, and W.Y. Hsu, 'Cu Planarization in Electrochemical Mechanical Planarization', *Journal of the Electrochemical Society,* 153 (2006), C377-C81.

[6] A. Tripathi, C. Burkhard, I.I. Suni, Y. Li, F. Doniat, A. Barajas, and J. McAndrew, 'Electrolyte Composition for Cu Electrochemical Mechanical Planarization', *Journal of the Electrochemical Society,* 155 (2008), H918-H22.

[7] K.G. Shattuck, J.Y. Lin, P. Cojocaru, and A.C. West, 'Characterization of Phosphate Electrolytes for Use in Cu Electrochemical Mechanical Planarization', *Electrochimica Acta,* 53 (2008), 8211-16.

[8] P.K. Rao, 'Statistical Characterization and Sensor Based Modeling and Monitoring of Fine Abrasive, Chemical Mechanical Polishing Process', Oklahoma State University, 2006).

[9] P.B. Zantye, A. Kumar, and AK Sikder, 'Chemical Mechanical Planarization for Microelectronics Applications', *Materials Science and Engineering: R: Reports,* 45 (2004), 89-220

[10] T. Dobrev, DT Pham, and SS Dimov, 'Electro-Chemical Polishing: A Technique for Surface Improvements after Laser Milling', *Manufacturing Engineering center, Cardiff University, Cardiff, CF24 3AA* (2007).

[11] Chen, S.-W., Kung, T.-M., Liu, C.-P., Chang, S.-C., Cheng, Y.-L., and Wang, Y.-L., "Effect of Electric Potential and Mechanical Force on Copper Electro-Chemical Mechanical Planarization," *Japanese Journal of Applied Physics,* 51, 036504, 2012.

[12] F.Q. Liu, S.D. Tsai, Y. Hu, and L.Y. Chen, 'Method and Composition for Fine Copper Slurry for Low Dishing in Ecmp', Google Patents, 2004.

[13] S.J. Han, and Y.J. Seo, 'Voltage-Induced Material Removal Mechanism of Copper for Electrochemical-Mechanical Polishing Applications', *Transactions of Nonferrous Metals Society of China,* 19 (2009), s262-s65.

[14] A.S. Brown, 'Flat, Cheap, and under Control [Electrochemical Mechanical Planarization]', *Spectrum, IEEE,* 42 (2005), 40-45.
[15] Yong-Jin Seo, 'Electrochemical-Mechanical Polishing Application: Monitoring of Electrochemical Copper Removal from Current-Voltage Characteristics in Hno3 Electrolyte', *Microelectron. Eng.,* 88 (2011), 46-52.
[16] Y. Lee S. Lee, and M. Du, 'The Polishing Mechanism of Electrochemical Mechanical Polishing Technology', *Journal of Materials Processing Technology,* 140 (2003), 280-86
[17] J. Bae S. Jeong, H. Lee, H. Lee, Y. Lee, B. Park, H. Kim, S. Kim, and H. Jeong, 'Effect of Mechanical Factor in Uniformity for Electrochemical Mechanical Planarization', *Sensors and Actuators A: Physical,* 163 (2010), 433-39.
[18] S. Jeong, S. Lee, and H. Jeong, 'Effect of Polishing Pad with Holes in Electro-Chemical Mechanical Planarization', *Microelectronic Engineering,* 85 (2008), 2236-42.
[19] S. Kondo, S. Tominaga, A. Namiki, K. Yamada, D. Abe, K. Fukaya, M. Shimada, and N. Kobayashi, 'Novel Electro-Chemical Mechanical Planarization Using Carbon Polishing Pad to Achieve Robust Ultra Low-K/Cu Integration', in *Interconnect Technology Conference, 2005. Proceedings of the IEEE 2005 International*, 2005), pp. 203-05.
[20] Fukuda, Akira, Akira Kodera, Yasushi Toma, Tsukuru Suzuki, Hirokuni Hiyama, Toshiro Doi, Syuhei Kurokawa, and Osamu Ohnishi. "Removal rate simulation of dissolution-type electrochemical mechanical polishing." *Japanese Journal of Applied Physics* 49, no. 7 (2010): 6701.
[21] Chen, Chao Chang A., and Chi Hsiang Hsieh. "Manufacturing Analysis of Hybrid Energy Manufacturing Processes and Application to the Copper Chemical Mechanical Planarization/Polishing Process." *Proc. of*. Vol. 44.
[22] D. Truque, X. Xie, and D. Boning, 'Wafer Level Modeling of Electrochemical-Mechanical Polishing (Ecmp)', in *MRS Proceedings*, Cambridge Univ Press, (2007).
[23] F. Gao, and H. Liang, 'Transformable Oxidation of Tantalum in Electrochemical Mechanical Polishing (Ecmp)', *Journal of Electronic Materials,* 40 (2011), 134-40.
[24] D. COMSOL, 'Experimental Validation of Model of Electro-Chemical-Mechanical Planarization (Ecmp) of Copper'.
[25] S.S. Munnangi, 'Fabrication and Testing of Apparatus for Electrochemical Mechanical Polishing (Ecmp) of Copper for Semiconductor Applications', OKLAHOMA STATE UNIVERSITY, 2012).
[26] http://www.ni.com/digitalio/
[27] Kong Zhenyu, A. Oztekin, O. F. Beyca, U. Phatak, S. Bukkapatnam, and R. Komanduri, 'Process Performance Prediction for Chemical Mechanical Planarization (Cmp) by Integration of Nonlinear Bayesian Analysis and Statistical Modeling', *Semiconductor Manufacturing, IEEE Transactions on,* 23 (2010), 316-27.
[28] P. Choi, D.G. Bessarabov, and R. Datta, 'A Simple Model for Solid Polymer Electrolyte (Spe) Water Electrolysis', *Solid State Ionics,* 175 (2004), 535-39.
[29] JOM Bockris, AKN Reddy, and ME Gamboa-Aldeco, 'Modern Electrochemistry,

2a: Fundamentals of Electrodics', *Modern Electrochemistry, 2A: Fundamentals of Electrodics* (2000).

[30] www.mat.ethz.ch/news_events/archive/materialsday/.../prestat.pdf

[31] Ohri, Amit. Wireless sensor fusion approach for monitoring chemical mechanical planarization (CMP) process. 2010.

[32] Xu, Wenji, et al. "Surface quality prediction and processing parameter determination in electrochemical mechanical polishing of bearing rollers." *The International Journal of Advanced Manufacturing Technology* 63.1-4 (2012): 129-136.

[33] Microelectric Applications of Chemical Mechanical Planarization, Ed. Y. Li,Wiley-Interscience,(2008).

[34] D.Padhi, J.Yahalom, S. Gandikota, and G.Dixit, "Planarization of copper Thin films by Electropolishing in Phsophoric Acid for ULSI Applications,"*J. Electrochem. Soc.,* Vol. 150,No. 1,pp. G10-G14, (2003)

[35] R.Vidal and A.C. West, "Copper Electropolishing in Concentrated Phosphoric Acid, I.Experimental Findings," *J. of Electrochem. Soc.,*Vol. 142, No. 8, pp. 2682-2689, (1995).

[36] R.Vidal and A.C. West, "Copper Electropolishing in Concentrated Phosphoric Acid . II .Experimental Findings," *J. of Electrochem. Soc.,*Vol. 142, No. 8, pp. 2682-2689, (1995).

[37] G. Prentice, *Electrochemical Engineering Principles,* (1991).

[38] J.Newman and K.E. Thomas-Alyea, *Electrochemical Systems,* 3rd ed., (2004).

[39] Goonetilleke, P. C., and D. Roy. "Relative roles of acetic acid, dodecyl sulfate and benzotriazole in chemical mechanical and electrochemical mechanical planarization of copper." *Applied Surface Science* 254.9 (2008): 2696-2707.

[40] Kwon, Tae-Young, In-Kwon Kim, and Jin-Goo Park. "Effects of Additives in KOH Based Electrolytes on Cu ECMP." *MRS Proceedings*. Vol. 991. No. 1. Cambridge University Press, 2007.

[41] Gao, Feng. "Tribo-electrochemical Characterization of Tantalum during Electrochemical-Mechanical Polishing (ECMP)." (2013).

[42] Tiley, J., et al. "Novel automatic electrochemical–mechanical polishing (ECMP) of metals for scanning electron microscopy." *Micron* 41.6 (2010): 615-621.

[43] Ng, Dedy, et al. "Friction and wear-mode comparison in copper electrochemical mechanical polishing." *Journal of The Electrochemical Society* 155.7 (2008): H520-H524.

[44] Johnson, Joy Marie. "Modeling of advanced integrated circuit planarization processes: electrochemical-mechanical planarization (eCMP)", *STI CMP using non-conventional slurries*. Diss. Massachusetts Institute of Technology, 2009.

[45] Suni, Ian Ivar, and Bing Du. "Cu planarization for ULSI processing by electrochemical methods: a review." *Semiconductor Manufacturing, IEEE Transactions on* 18.3 (2005): 341-349.

[46] Lee, Shuo-Jen, Yu-Ming Lee, and Ming-Yu Chung. "Metal removal rate of the electrochemical mechanical polishing technology for stainless steel-the electrochemical characteristics." *Proceedings of the Institution of Mechanical Engineers, Part B: Journal of Engineering Manufacture* 220.4 (2006): 525-530.

[47] Wang, Zhi hong, *et al.* "ECMP polishing sequence to improve planarity and defect performance." U.S. Patent Application 11/849,724.
[48] Duboust, Alain, *et al*. "Planarization of substrates at a high polishing rate using electrochemical mechanical polishing." WIPO Patent No. 2007121177. 26 Oct. 2007.
[49] C. Pettit and D. Roy, "Role of iodate ions in chemical mechanical and electrochemical mechanical planarization of Ta investigated using time-resolved impedance spectroscopy," *Materials Letters,* vol. 59, pp. 3885-3889, 2005.
[50] A. J. a. S. V. Babu, "Effect of pH on chemical-mechanical polishing of Cu and Ta," J. Electrochem. Soc., vol. 151, p. G709, 2004.
[51] Q. S. X.G. An, "Research on the Combined Electro Chemical Mechanical Polishing," Electro Machining, vol. 2, 2002
[52] I. MathWorks, *MATLAB: the language of technical computing. Desktop tools and development environment, version 7* vol. 9: MathWorks, 2005.
[53] C. M. Sulyma and D. Roy, "Voltammetric current oscillations due to general and pitting corrosion of tantalum: Implications for electrochemical–mechanical planarization," *Corrosion Science,* vol. 52, pp. 3086-3098, 2010.
[54] Wang, Zhihong, *et al*. "Process and composition for conductive material removal by electrochemical mechanical polishing." WIPO Patent No. 2006121600. 17 Nov. 2006.
[55] T.-M. Kung, C.-P. Liu, S.-C. Chang, K.-W. Chen, and Y.-L. Wang, "Effect of Cu-Ion concentration in concentrated H3PO4 electrolyte on Cu electrochemical mechanical planarization," *Journal of The Electrochemical Society,* vol. 157, pp. H763-H770, 2010.
[56] M. Zhu and W. G. Catabay, "Electro chemical mechanical polishing method and device for planarizing semiconductor surfaces," ed: Google Patents, 2007.
[57] Y. LI, "METHOD AND APPARATUS FOR ELECTROCHEMICAL MECHANICAL POLISHING NIP SUBSTRATES," ed: WO Patent 2,008,058,200, 2008.
[58] R. A. Mavliev, A. Duboust, and S. D. Tsai, "Methods and apparatus for polishing a substrate," ed: Google Patents, 2004.
[59] J. K. So, "Conductive polishing pad with anode and cathode," ed: Google Patents, 2005.
[60] H.-P. Wang and Q. Liu, "Method and apparatus for detecting micro-scratches in semiconductor wafers during polishing process," ed: Google Patents, 2002.
[61] D. Zeidler, Z. Stavreva, M. Plötner, and K. Drescher, "Characterization of Cu chemical mechanical polishing by electrochemical investigations," *Microelectronic Engineering,* vol. 33, pp. 259-265, 1997.
[62] R. Chang, Y. Cao, and C. J. Spanos, "Modeling the electrical effects of metal dishing due to CMP for on-chip interconnect optimization," *Electron Devices, IEEE Transactions on,* vol. 51, pp. 1577-1583, 2004.
[63] Tominaga, Shigeru, *et al.* "Hybrid electrochemical mechanical planarization process for Cu dual-damascene through-silicon via using noncontact electrode pad." *Japanese Journal of Applied Physics* 49.5 (2010).
[64] Jia, Renhe, et al. "Process for high copper removal rate with good planarization and surface finish." U.S. Patent Application 11/399,560.

[65] R. Bajaj, "Electro-chemical mechanical planarization pad with uniform polish performance," ed: Google Patents, 2010.
[66] B. M. Basol and H. Talieh, "System and method for electrochemical mechanical polishing," ed: Google Patents, 2010
[67] C. E. Uzoh and J. M. E. Harper, "Method of electrochemical mechanical planarization," ed: Google Patents, 1998.
[68] R. A. Mavliev, A. Duboust, and S. D. Tsai, "Methods and apparatus for polishing a substrate," ed: Google Patents, 2004.
[69] R. Chang, Y. Cao, and C. J. Spanos, "Modeling the electrical effects of metal dishing due to CMP for on-chip interconnect optimization," *Electron Devices, IEEE Transactions on,* vol. 51, pp. 1577-1583, 2004.
[70] Y.-L. Chen, S.-M. Zhu, S.-J. Lee, and J. C. Wang, "The technology combined electrochemical mechanical polishing," *Journal of Materials Processing Technology,* vol. 140, pp. 203-205, 2003.
[71] A. Muthukumaran, N. Venkataraman, and S. Raghavan, "Evaluation of sulfonic acid-based solutions for electrochemical mechanical removal of tantalum," *Journal of The Electrochemical Society,* vol. 155, pp. H184-H187, 2008.
[72] F. Doniat, M. L. Fisher, A. D. Zdunek, A. A. Barajas, I. Suni, X. Chu, A. Tripathi, and Y. Li, "ELECTROLYTE FORMULATION FOR ELECTROCHEMICAL MECHANICAL PLANARIZATION," ed: Google Patents, 2007.
[73] L. Economikos, X. Wang, X. Sakamoto, P. Ong, M. Naujok, R. Knarr, L. Chen, Y. Moon, S. Neo, and J. Salfelder, "Integrated electro-chemical mechanical planarization (Ecmp) for future generation device technology," in *Interconnect Technology Conference, 2004. Proceedings of the IEEE 2004 International*, 2004, pp. 233-235.
[74] V. Hardikar, "Methods of multi-step electrochemical mechanical planarization of Cu," ed: Google Patents, 2008.
[75] R. Mavliev, B. A. Swedek, A. N. Wiswesser, and M. Birang, "Endpoint system for electro-chemical mechanical polishing," ed: Google Patents, 2004.
[76] T. S. Kaushal, C. Q. Dam, and Y. Hu, "Chemical mechanical polishing endpoinat detection," ed: Google Patents, 2004.
[77] H. Hocheng, H. Tsai, and M. Tsai, "Effects of kinematic variables on nonuniformity in chemical mechanical planarization," *International Journal of Machine Tools and Manufacture,* vol. 40, pp. 1651-1669, 2000.
[78] S. R. Schmidt and R. G. Launsby, *Understanding industrial designed experiments*: Air Academy Press, 1989.
[79] D. C. Montgomery, *Design and analysis of experiments* vol. 7: Wiley New York, 1984.
[80] A. Antoniou and C. E. Vorlow, "Recurrence quantification analysis of wavelet pre-filtered index returns," *Physica A: Statistical Mechanics and its Applications,* vol. 344, pp. 257-262, 2004.
[81] S. Bukkapatnam, P. Rao, and R. Komanduri, "Experimental dynamics characterization and monitoring of MRR in oxide chemical mechanical planarization (CMP) process," *International Journal of Machine Tools and Manufacture,* vol. 48, pp. 1375-1386, 2008.

[82] U. Phatak, S. Bukkapatnam, Z. Kong, and R. Komanduri, "Sensor-based modeling of slurry chemistry effects on the material removal rate (MRR) in copper-CMP process," *International Journal of Machine Tools and Manufacture,* vol. 49, pp. 171-181, 2009.
[83] . W. Carter and J. P. Chamberlain, "CMP process involving frequency analysis-based monitoring," ed: Google Patents, 2002.
[84] R. H. Carver and M. R. Carver, *Doing data analysis with Minitab 14*: Thomson/Brooks/Cole, 2004.
[85] D. A. Dornfeld and J. Tang, "Semiconductor wafer chemical-mechanical planarization process monitoring and end-point detection method and apparatus," ed: Google Patents, 2006
[86] J.-P. Eckmann, S. O. Kamphorst, and D. Ruelle, "Recurrence plots of dynamical systems," *Europhys. Lett,* vol. 4, pp. 973-977, 1987.
[87] A. Facchini and H. Kantz, "Curved structures in recurrence plots: The role of the sampling time," *Physical Review E,* vol. 75, p. 036215, 2007.
[88] A. Facchini, H. Kantz, and E. Tiezzi, "Recurrence plot analysis of nonstationary data: the understanding of curved patterns," *Physical Review E,* vol. 72, p. 021915, 2005.
[89] A. M. Fraser and H. L. Swinney, "Independent coordinates for strange attractors from mutual information," *Physical review A,* vol. 33, p. 1134, 1986.
[90] R. Ganesan, "Real-time monitoring of complex sensor data using wavelet-based multiresolution analysis," *The International Journal of Advanced Manufacturing Technology,* vol. 39, pp. 543-558, 2008.
[91] R. GANESAN, T. DAS, A. SIKDER, and A. KUMAR, "SYSTEM AND METHOD FOR THE IDENTIFICATION OF CHEMICAL MECHANICAL PLANARIZATION DEFECTS," ed: WO Patent 2,005,100,976, 2005.
[92] J. Gao and H. Cai, "On the structures and quantification of recurrence plots," *Physics Letters A,* vol. 270, pp. 75-87, 2000.
[93] A. Groth, "Visualization of coupling in time series by order recurrence plots," *Physical Review E,* vol. 72, p. 046220, 2005.
[94] R. Hegger, H. Kantz, and T. Schreiber, "Practical implementation of nonlinear time series methods: The TISEAN package," *Chaos: An Interdisciplinary Journal of Nonlinear Science,* vol. 9, pp. 413-435, 1999.
[95] H. Kantz and T. Schreiber, *Nonlinear time series analysis* vol. 7: Cambridge university press, 2004.
[96] C. D. Le, "Eddy current measuring system for monitoring and controlling a CMP process," ed: Google Patents, 2004.
[97] Q. Luo, S. Ramarajan, and S. Babu, "Modification of the Preston equation for the chemical–mechanical polishing of copper," *Thin Solid Films,* vol. 335, pp. 160-167, 1998.
[98] N. Marwan, M. Carmen Romano, M. Thiel, and J. Kurths, "Recurrence plots for the analysis of complex systems," *Physics Reports,* vol. 438, pp. 237-329, 2007.
[99] S. Schinkel, O. Dimigen, and N. Marwan, "Selection of recurrence threshold for signal detection," *The European Physical Journal Special Topics,* vol. 164, pp. 45-53, 2008.

[100] R. H. Myers and C. M. Anderson-Cook, *Response surface methodology: process and product optimization using designed experiments* vol. 705: Wiley. com, 2009.
[101] J. Nichols, S. Trickey, and M. Seaver, "Damage detection using multivariate recurrence quantification analysis," *Mechanical systems and signal processing,* vol. 20, pp. 421-437, 2006.
[102] C. Rhodes and M. Morari, "Determining the model order of nonlinear input/output systems directly from data," in *American Control Conference, 1995. Proceedings of the*, 1995, pp. 2190-2194.
[103] Anant K. Arulmozhi, “Experimental and Molecular Dynamics studies on Copper Electrochemical Mechanical Planarization (Cu ECMP process),” OKLAHOMA STATE UNIVERSITY, 2013.

Appendix 1

Time series and FFT

```
%% Current Directory Information
current_directory = cd;
%% UI for getting the file
[FileName,PathName,FilterIndex] = uigetfile({'*.xls'; '*.xlsx'})
file_directory = strcat(PathName);
%% UI to get file specifics
prompt = {'Enter Worksheet to Pick','Enter Data Units', 'Sensor', 'Saving
Name'};
dlg_title = 'Input for peaks function';
num_lines = 1;
def = {'1','A','Output Current','Output Current'};
answer = inputdlg(prompt,dlg_title,num_lines,def);
options.Resize='on';
options.WindowStyle='normal';
options.Interpreter='tex';
saving_name = strcat(answer{4},'.txt')
%% Convert to real information
xlsheet = strcat('sheet', answer{1});
units = answer{2};
cd(file_directory)
[data,txt,raw]=xlsread(FileName,xlsheet);
cd(current_directory)
save(saving_name, 'data', '-ASCII');
fft_signal(data(:,2),100,answer{3},answer{2},answer{4});

function [ ] = fft_signal(data, sampling_rate,
sensor_string,units,condition);
%FFT on experimental data

%the name of the variable that corresponds to the exptl data
dat_var = data;
Fs = sampling_rate;   %sampling frequency
T = 1/Fs;   %sample time
L = length(dat_var);   %Length of the signal (no. of data points)
t = (0:L-1)*T;  %Time vector

%mean of the amplitudes
dat_varMean = mean(dat_var);

%make the amplitude data mean over zero
y = dat_var - dat_varMean;

plot_title = horzcat(sensor_string, ' ', 'Sensor');
%plot the time series
figure;
plot(t,y, 'linewidth', 1); grid on; axis tight;
title(plot_title, 'fontsize', 16);
```

```
xlabel('Time (seconds)', 'fontsize', 14);
ylabel(units, 'fontsize', 14);
set(gca, 'linewidth', 2.5)
set(gca, 'fontsize', 12);
set(gcf, 'color', [1 1 1]);
file_name = horzcat('Time Series', ' ', condition, ' ',sensor_string);
saveas(gcf, file_name, 'fig');
close gcf


%implement FFT
NFFT = 2^nextpow2(L);  %no. of points for applying FFT
Y = fft(y,NFFT)/L;  %compute FFT for NFFT number of points, normalize by
dividing by L
f = Fs/2 * linspace(0, 1, NFFT/2 + 1);

%plot the FFT
figure;
plot(f,2*abs(Y(1:NFFT/2+1)), 'linewidth', 2.5); grid on; axis tight;
fft_title = horzcat(sensor_string, ' ','Amplitude spectrum');
title(fft_title, 'fontsize', 16);
xlabel('Frequency (Hz)', 'fontsize', 14);
ylabel('|Y(f)|', 'fontsize', 14);
set(gca, 'fontsize', 12);
set(gca, 'linewidth', 2.5)
set(gcf, 'color', [1 1 1]);
file_name = horzcat('FFT', ' ', sensor_string);
saveas(gcf, file_name, 'fig');
close gcf



figure;
plot(f,20*log10(abs(Y(1:NFFT/2+1))), 'linewidth', 2.5); grid on; axis
tight;
fft_title = horzcat(sensor_string, ' ','Amplitude spectrum');
title(fft_title, 'fontsize', 16);
xlabel('Frequency (Hz)', 'fontsize', 14);
ylabel('dB', 'fontsize', 14);
set(gca, 'fontsize', 12);
set(gca, 'linewidth', 2.5)
set(gcf, 'color', [1 1 1]);
file_name = horzcat('PSD', ' ', sensor_string);
saveas(gcf, file_name, 'fig');
close gcf
```

Appendix 2

Spectrogram

```
%% Calculate Spectrogram

F = 1:0.1:Fs/2;
y = y(1:10000);
figure;
spectrogram(y,64,4,F,sampling_rate);
fft_title = horzcat(sensor_string, ' ','Spectrogram, Non-Normalized, 64
Windows');
title(fft_title, 'fontsize', 16);
xlabel('Frequency (Hz)', 'fontsize', 14);
ylabel('Time(Sec)', 'fontsize', 14);
set(gca, 'fontsize', 12);
set(gca, 'linewidth', 2.5)
set(gcf, 'color', [1 1 1]);
 file_name = horzcat('Non-Normalized Spectrogram, 64', ' ',
sensor_string);
 saveas(gcf, file_name, 'fig');
 close gcf


figure;
spectrogram(y,64,4,F);
fft_title = horzcat(sensor_string, ' ','Spectrogram, Normalized, 64
Windows');
title(fft_title, 'fontsize', 16);
xlabel('Frequency (pi*rad/sample)', 'fontsize', 14);
ylabel('Time(Data Points)', 'fontsize', 14);
set(gca, 'fontsize', 12);
set(gca, 'linewidth', 2.5)
set(gcf, 'color', [1 1 1]);
 file_name = horzcat('Normalized Spectrogram, 64', ' ', sensor_string);
saveas(gcf, file_name, 'fig');
 close gcf
```

Appendix 3

Statistical features extraction

```
function [m_arr] = sample(file_name,sheet_name,col_name,length)
   col_name=strcat(col_name,':',col_name);
   sample=xlsread(file_name,sheet_name,col_name);
   ctr=1;
   mean_arr=[];
   var_arr=[];
   std_arr=[];
   skewness_arr=[];
   kurtosis_arr=[];
   max_arr=[];
   mode_arr=[];
   cov_arr=[];
   for i = (1:length:size(sample))
      if i+length > size(sample)
          var_1=size(sample);
      else
          var_1=i+length;
      end
      arr = sample(i:var_1);
      mean_arr(ctr)=mean(arr);
      std_arr(ctr)=std(arr);
      var_arr(ctr)=var(arr);
      skewness_arr(ctr)=skewness(arr);
      kurtosis_arr(ctr)=kurtosis(arr);
      max_arr(ctr)=max(arr);
      mode_arr(ctr)=mode(arr);
      cov_arr(ctr)=cov(arr);
      ctr=ctr+1;
   end
   m_arr=mean_arr;
   m_arr=var_arr;
   m_arr=std_arr;
   m_arr=skewness_arr;
   m_arr=kurtosis_arr;
   m_arr=max_arr;
   m_arr=cov_arr;
```

VITA

SAKTHI JAYA RAHUL RAVICHANDRAN

Candidate for the Degree of

Master of Science

Thesis: STATISTICAL ANALAYSIS AND SENSOR BASED MODELING OF ELECTROCHEMICAL MECHANICAL POLISHING OF Cu BLANKET WAFER FOR SEMICONDUCTOR APPLICATIONS

Major Field: Industrial Engineering and Management

Biographical:

Education:

Completed the requirements for the Master of Science in Industrial Engineering and Management (IEM) at Oklahoma State University, Stillwater, Oklahoma in July 2013.

Completed the requirements for the Bachelor of Engineering in Mechanical Engineering at Velammal Engineering College, Anna University, Chennai, Tamil Nadu/India in May 2010.

Experience:
Graduate Engineer Trainee, Stanadyne Amalgamations Pvt. Ltd, Thiruvallur district near Chennai, Tamilnadu, India (Aug 2010 – July 2011)
Graduate Research Assistant, IEM, OSU, Stillwater (Jan 2012 to July 2013)

Professional Memberships:
Institute of Industrial Engineers
Alpha Pi Mu National Industrial Engineering Honor Society
Society for Engineering & Management Systems
Society of Automotive Engineers